A Novel Method and Error Analysis for Beam Optics Measurements and Corrections at the Large Hadron Collider

Dissertation

zur Erlangung des Doktorgrades
an der Fakultät für Mathematik, Informatik und Naturwissenschaften
Fachbereich Physik
der Universität Hamburg

vorgelegt von
Andy Sven Langner

Hamburg
2016

Gutachter der Dissertation:	Prof. Dr. Eckhard Elsen Prof. Dr. Jörg Rossbach
Mitglieder der Prüfungskommission:	Prof. Dr. Peter Schleper Prof. Dr. Peter Schmelcher Dr. Rogelio Tomás
Tag der Disputation:	03.02.2017
Dekan der MIN-Fakultät:	Prof. Dr. Heinrich Graener
Vorsitzender des Fach-Promotionsausschuss Physik:	Prof. Dr. Wolfgang Hansen

Dieses Dokument wurde mit LaTeX und KOMA-Script erstellt.

Eidesstattliche Versicherung

Hiermit erkläre ich an Eides statt, dass ich die vorliegende Dissertationsschrift selbst verfasst und keine anderen als die angegebenen Quellen und Hilfsmittel benutzt habe.

Genf, den 06.10.2016 Unterschrift:

Liste der aus dieser Dissertation hervorgegangenen Vorveröffentlichungen

Teilergebnisse der vorliegenden Arbeit wurden in folgenden Aufsätzen vorab publiziert. Im Falle von Arbeiten mit Koautoren wurden nur eigene Beiträge übernommen, falls nicht an entsprechender Stelle anders gekennzeichnet.

Fachzeitschriften mit Peer-Review

A. Langner and R. Tomás, "Optics measurement algorithms and error analysis for the proton energy frontier", Phys. Rev. ST Accel. Beams, **18**, 031002, 2015.

A. Langner, et al., "Utilizing the *N* beam position monitor method for turn-by-turn optics measurements", Phys. Rev. Accel. Beams, **19**, 092803, 2016.

Konferenzbeiträge

P. Skowronski, et al., "Limitations on Optics Measurements in the LHC", in Proceedings of IPAC2016, 2016.

A. Valdivieso, et al., "Optics-Measurement-Based BPM Calibration", in Proceedings of IPAC2016, 2016.

J. Coello de Portugal, et al., "Local Optics Corrections in the HL-LHC IR", in Proceedings of IPAC2016, 2016.

A. Langner, et al., "Optics Model", in Proceedings of the 2015 Evian Workshop on LHC Beam Operation, 2015.

A. Langner, et al., "Developments of the Segment-by-Segment Technique for Optics Corrections in the LHC", in Proceedings of IPAC2015, 2015.

A. Langner, et al., "Optics Measurement using the N-BPM Method for the ALBA Synchrotron", in Proceedings of IPAC2015, 2015.

R. Tomás, et al., "Prospects for the LHC optics measurements and corrections at higher energy", in Proceedings of IPAC2014, 2014.

A. Langner, et al., "OMC Improvements and Prospects for 2015", in Proceedings of the 2014 Evian Workshop on LHC Beam Operation, 2014.

A. Langner and R. Tomás, "Improvements in the Optics Measurement Resolution for the LHC", in Proceedings of IPAC2014, 2014.

N. Aquilina, et al., “LHC magnets towards 7 TeV operation”, in Proceedings of IPAC2014, 2014.

R. Tomás, et al., “Optics and Non-Linear Beam Dynamics at 4 and 6.5 TeV”, in Proceedings of the 2012 Evian Workshop on LHC Beam Operation, 2012.

Berichte

A. Valdivieso, et al., “LHC injection optics measurements at commissioning (2015)”, CERN-ATS-Note-2016-0033, 2016.

A. Langner, et al., “First beam test of a combined ramp and squeeze at LHC”, CERN-ACC-NOTE-2015-0023, 2015.

A. Langner, et al., “LHC Optics Commissioning at $\beta^* = 40$ cm and 60 cm”, CERN-ACC-NOTE-2015-0035, 2015.

T. Bach, et al., “1 % Calibration Errors in MQY Magnets”, CERN-ATS-Note-2013-029 MD (LHC), 2013.

Kurzbeschreibung

Der Large Hadron Collider (LHC) ist aktuell der weltgrößte Teilchenbeschleuniger mit der höchsten Schwerpunktsenergie bei Teilchenkollisionsexperimenten. Für die maximal erreichbare Leistungsfähigkeit eines solchen Beschleunigers ist die Kontrolle über die Teilchenstrahlfokussierung unabdingbar. Zur Charakterisierung der Fokussiereigenschaften wird am LHC die Position des zum Schwingen angeregten Strahls für jeden Umlauf an zahlreichen Messinstrumenten (BPMs) entlang des Beschleunigers aufgezeichnet. In der vorliegenden Arbeit wird ein neues Analyseverfahren für diese Messungen (N-BPM Methode) basierend auf einer detaillierten Untersuchung von systematischen und statistischen Fehlerquellen und ihren Korrelationen gezeigt. Während der Inbetriebsetzung des LHC bei einer bisher unerreichten Energie von 6.5 TeV wurde dieses Analyseverfahren angewandt. Die dabei erreichte Fokussierung ist stärker als im LHC Design vorgesehen. Dies führt zu kleineren transversalen Strahlgrößen an den Kollisionspunkten und ermöglicht so eine höhere Rate von Teilchenkollisionen.
An vielen Synchrotron-Lichtquellen werden zur Bestimmung der Fokussierparameter die Abweichungen der periodischen Teilchenbahn beobachtet, die durch absichtliche Veränderungen der Magnetfelder induziert werden (Orbit Antwortmatrix). Im Gegensatz dazu liefert für viele dieser Maschinen aufgrund der Abstände zwischen den BPMs die Analyse der gemessenen Strahlpositionsdaten pro Umlauf weniger genaue Ergebnisse. Die begrenzte Messgenauigkeit wird durch die N-BPM Methode überwunden, indem es die Analyse der Messdaten von mehreren BPMs ermöglicht. Sie wurde an der ALBA Synchrotron-Lichtquelle angewandt und mit der Orbit Antwortmatrix Methode verglichen. Die deutlich schnellere Messung mit der N-BPM Methode stellt hierbei einen entscheidenden Vorteil dar.
Abschließend wird ein Ausblick auf kommende Herausforderungen in der Kontrolle der Strahlfokussierung am HL-LHC, einer zukünftigen Erweiterung des LHC, gegeben.

Abstract

The Large Hadron Collider (LHC) is currently the world's largest particle accelerator with the highest center of mass energy in particle collision experiments. The control of the particle beam focusing is essential for the performance reach of such an accelerator. For the characterization of the focusing properties at the LHC, turn-by-turn beam position data is simultaneously recorded at numerous measurement devices (BPMs) along the accelerator, while an oscillation is excited on the beam. A novel analysis method for these measurements (N-BPM method) is developed here, which is based on a detailed analysis of systematic and statistical error sources and their correlations. It has been applied during the commissioning of the LHC for operation at an unprecedented energy of 6.5 TeV. In this process a stronger focusing than its design specifications has been achieved. This results in smaller transverse beam sizes at the collision points and allows for a higher rate of particle collisions.

For the derivation of the focusing parameters at many synchrotron light sources, the change of the beam orbit is observed, which is induced by deliberate changes of magnetic fields (orbit response matrix). In contrast, the analysis of turn-by-turn beam position measurements is for many of these machines less precise due to the distance between two BPMs. The N-BPM method overcomes this limitation by allowing to include the measurement data from more BPMs in the analysis. It has been applied at the ALBA synchrotron light source and compared to the orbit response method. The significantly faster measurement with the N-BPM method is a considerable advantage in this case.

Finally, an outlook is given to the challenges which lie ahead for the control of the beam focusing at the HL-LHC, which is a future major upgrade of the LHC.

Contents

1. Introduction

Accelerator physics is a relatively young branch in the physics domain. It describes the machines that are used for accelerating, storing and transporting elementary charged particles by means of electromagnetic fields, which are in the following referred to as particle accelerators, or simply accelerators. It furthermore describes the dynamics of these particles in an accelerator.

The history of particle accelerators dates back to the 1920s, where R. Widerøe successfully accelerated ions up to an energy of 50 keV [1], based on a linear accelerator concept of G. Ising [2]. Subsequently, accelerators were advanced, reaching higher beam energies and intensities, while repeatedly new technical concepts were developed. For a detailed report on the history of particle accelerators, the reader is referred to [3–5].

Since then, accelerators have become an important technology with applications in various different fields, e.g. fundamental and applied research, medical therapy, industry and defense [6–9].

In the following sections, the Large Hadron Collider (LHC) is introduced, which is a hadron accelerator, designed to operate at an unprecedented beam energy of 7 TeV and used for fundamental particle physics research.

The performance characteristics of such an accelerator are introduced, as well as the nomenclature which is used to describe the beam dynamics. Furthermore, techniques to measure and correct certain aspects of the beam motion are explained, which are crucial for the operation of this machine. In Chapter 2 a new method, named N-BPM method, is developed for the measurement of the focusing properties of the accelerator. This new method represents a significant improvement in the precision and accuracy compared to previous methods.

It is benchmarked in simulations and in comparison with other measurement techniques. Moreover its successful application at the ALBA accelerator is presented. In Chapter 3 the N-BPM method is shown in practice during the commissioning of the LHC at an energy of 6.5 TeV. An outlook is given in Chapter 4 to the challenges that lie ahead for the High Luminosity Large Hadron Collider (HL-LHC), which is a major upgrade of the LHC.

1.1. The Large Hadron Collider

The LHC is a circular accelerator located at the European Organization for Nuclear Research (CERN) in Switzerland. The purpose of this machine is to study rare high energy physics events by colliding two proton beams at dedicated interaction points (IPs), which are surrounded by detectors for the collision products [10]. The most prominent achievement was the discovery of the Higgs boson[1]. A part of the LHC operation time is dedicated to the collision of lead ions. These heavy ion collisions allow to study matter interaction in extreme conditions of high temperature and high particle densities [11].
The particles for the LHC are accelerated in steps, using several smaller accelerators, c.f. Fig. 1.1. This is not only an efficient approach, as in this case the smaller accelerators already existed, but also inevitable, as e.g. the required precision of the magnetic fields in a circular accelerator are technologically difficult to achieve for an acceleration from rest. Furthermore, the beam charge distribution limits the maximum beam intensity for a given injection energy of a circular accelerator [12], which sets bounds to the ratio of injection energy to maximum energy.
The first acceleration of protons up to energies of 50 MeV takes place in the linear accelerator LINAC2. Afterwards the particles are transferred consecutively to the Proton Synchrotron (PS), Proton Synchrotron Booster (PSB) and Super Proton Synchrotron (SPS), where they reach at the end an energy of 450 GeV before they are injected into the LHC. A complete fill of the LHC includes according to design parameters, up to 2808 bunches of 1.15×10^{11} particles each[2]. This corresponds to an energy of 362 MJ which is stored in each beam after acceleration to 7 TeV [14].
Special care needs to be taken to protect the machine elements from its beams. For example, collimators are used to ensure that the beam size stays within limits [15]. The beam loss detection and beam dump system are responsible for a safe and fast extraction of the beams in case of problems [16]. Most of the LHC magnets are superconducting (sc), due to the required high magnetic fields. The process, when an sc magnet exceeds the critical temperature and becomes normal conducting, is referred to as quenching. Another crucial safety system is the quench protection system (QPS) [17]. It monitors the resistance of the sc magnets and mitigates the effects of a quench. An incident in 2008 showed the severe damage that may result due to a quench, when a fault in the electrical connection from a dipole to a quadrupole occurred, which delayed the LHC start by several months [18].

[1] The discovery of the Higgs boson has been announced in July 2012 at CERN. In 2013 the Nobel Prize in Physics has been awarded to Francois Englert and Peter Higgs for the theoretical derivation of the Higgs mechanism.

[2] An acceleration which uses radio frequency (rf) fields allows only for a beam which consists of bunches of particles with a specific length and distance between two bunches, depending on the rf frequency.

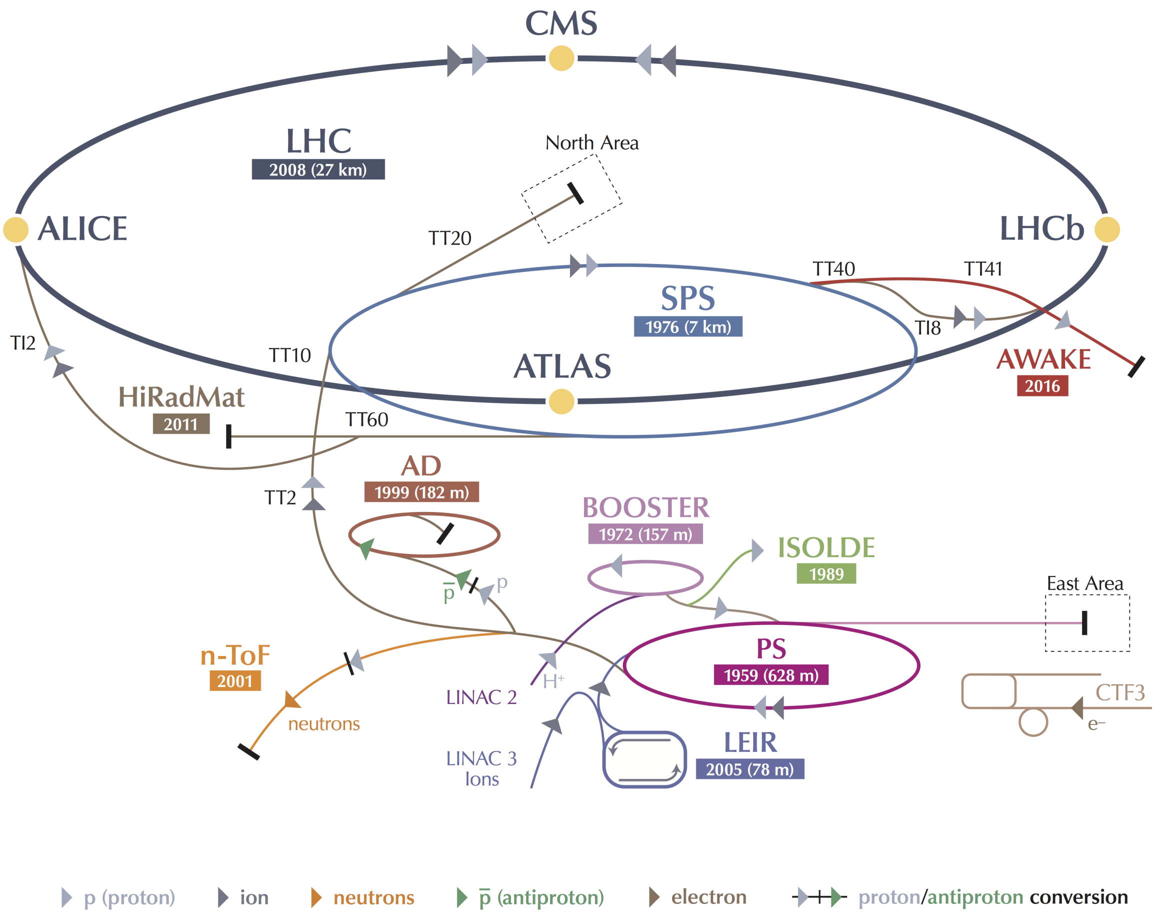

Figure 1.1.: Illustration of the CERN accelerator complex. Colored arrowheads indicate the possible paths of different particles. © CERN [13].

1.1.1. Performance characteristics

The purpose of a high energy particle collider is to induce particle interactions (events), which are suitable for analysis by the experimental detectors. Its performance is therefore characterized by the amount of events that are produced.

Center of mass energy

The energy in the center of mass frame defines the possible particle interaction processes, as e.g. for the production of a particle at least its mass at rest is required. For ultra-relativistic particles, head-on collisions of two particle beams are preferred compared to a fixed target collision, cf. Fig. 1.2, as the later becomes less efficient. For example, in case of the LHC which is designed to operate at a beam energy of

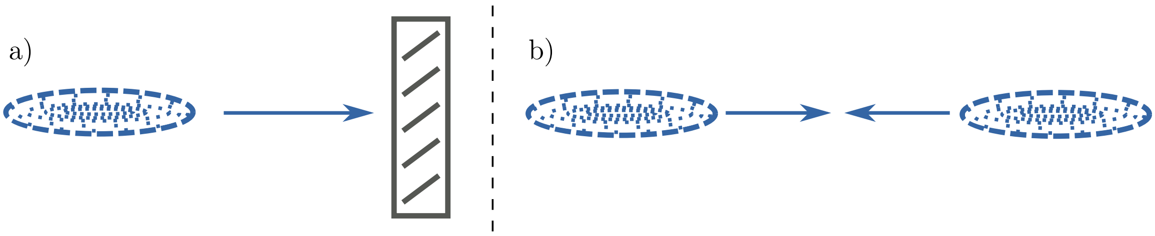

Figure 1.2.: Illustration of a collision experiment where particles either collide a) with other particles which are in rest (fixed target), or b) head on with particles of same momentum.

$E_1 = 7\,\mathrm{TeV}$, the energy available for particle production in head-on collisions would be $E = 2E_1 = 14\,\mathrm{TeV}$. A fixed target experiment with the same beam energy would only result in a center of mass energy of $E = \sqrt{2E_1mc^2} = 115\,\mathrm{GeV}$, cf. [5]. Hence, colliding beams are used for high energy particle physics experiments.
Furthermore, the cross section, i.e. the likelihood of a certain event, depends on the energy. For example, the cross section for a Higgs boson production in a proton-proton (pp) collider, for center of mass energies from 14 TeV to 100 TeV, is increasing with energy [19]. This means that a pp collider which is operated at larger energies, will produce more of these particles.

Luminosity

A second measure for the performance of a collider is the rate of particle collisions. The higher this rate is, the faster a rare event may be detected with statistical significance. The rate for a certain event is described as $\mathcal{L}\sigma$, where σ is the cross section of this event, and $\mathcal{L}$ the luminosity. The luminosity describes the probability of particle encounters in the colliding beams. While the cross section is determined by the beam energy, the luminosity depends on further parameters of the accelerator. For two Gaussian beams colliding head-on it is defined as

$$\mathcal{L} = \frac{1}{4\pi}\frac{N_1N_2fN_b}{\sigma_x\sigma_y}, \tag{1.1}$$

where $N_{1,2}$ are the number of particles per bunch for the two beams, and $\sigma_{x,y}$ are the horizontal and vertical size of the beam [20]. $\mathcal{L}$ depends furthermore on the rate of crossings which is described by the revolution frequency f and the number of bunches N_b in the accelerator. Since the parameters in Eq. (1.1) change with time, as e.g. the amount of particles decreases or the beam sizes change, it is important to assess the integrated luminosity

$$\mathcal{L}_{\mathrm{int}} = \int \mathcal{L}\,\mathrm{d}t. \tag{1.2}$$

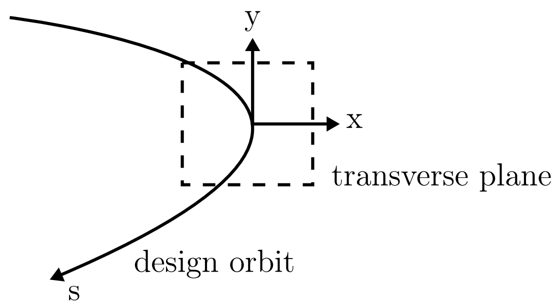

Figure 1.3.: Schematic of the Frenet-Serret coordinate system, which is used to describe the particle motion in an accelerator in the vicinity of a design orbit.

1.1.2. Linear beam dynamics

In this section the basic principles and the nomenclature which is used to describe the beam motion in an accelerator is introduced. The focus is on the transverse beam dynamics and on circular accelerators. For a more general explanation and especially for longitudinal and acceleration related effects, the reader is referred to [4, 5, 21].
The motion of charged particles can be controlled using electric and magnetic fields as described by the Lorentz force

$$\vec{F}_L = q(\vec{E} + \vec{v} \times \vec{B}). \tag{1.3}$$

For the deflection of charged particles, magnetic fields become more efficient for larger velocities of the particles. Magnetic fields are therefore preferred for steering of the beam. For example, a velocity of 14 % of the speed of light is for protons[1] already achieved in LINAC2, which is the first linear accelerator of the LHC proton acceleration chain, cf. Fig. 1.1.
In the following equations, a coordinate system which moves along the design orbit as described in Fig. 1.3 will be used.
In a continuous dipole field in the vertical direction, $|\vec{B}| = B_y$, a charged particle will be moving along a circle. The radius r is determined by setting the Lorentz force equal to the centripetal force, which gives

$$\frac{1}{r} = \frac{q}{p} B_y, \tag{1.4}$$

for a particle with charge q and momentum p. The size of an accelerator and the maximum magnetic field determine the maximum achievable particle momentum. For example for the LHC with a circumference of 27 km and a kinetic energy of 7 TeV

[1] at 0.14 c the relativistic and non-relativistic momentum of a proton deviate by 1 %

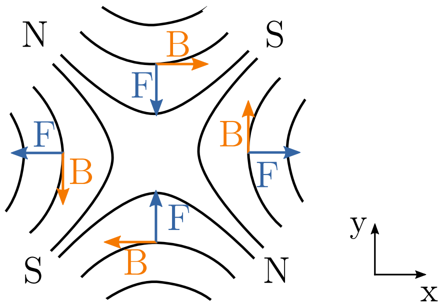

Figure 1.4.: Magnetic field lines of a quadrupole magnet. The resulting force is indicated for a positively charged particle moving perpendicular into the drawing plane. Particles with a transverse offset from the quadrupole center will be focused in the vertical plane and defocused in the horizontal plane.

of the protons, a magnetic field of $B = 5.4\,\mathrm{T}$ would be needed. Since the magnetic field for bending is not continuous, but interrupted to place other elements in the accelerator, in practice a magnetic field of more than $8\,\mathrm{T}$ is used.

For an ideal vertical magnetic dipole field with $B_x = B_z = 0$ and $B_y = B_0$, any perturbation which causes a particle to move in the vertical direction, will not receive a restoring force. With each turn the particle will deviate further from the design orbit, until it gets lost due to an interaction with the beam pipe. In the horizontal plane there is a natural focusing, as a particle which deviates from the design orbit will move on a displaced circle of same size. Hence, it will for small deviations periodically return and cross the design orbit. A focusing in both planes can for example be achieved with curved dipole fields, as described in [22]. However, this method which is also called weak focusing, is unfeasible for higher energies, as the maximum particle displacements from the design orbit become too large [21]. Another method to focus particles is to use quadrupole magnets which are illustrated in Fig. 1.4.

Though a quadrupole is focusing only in one plane and defocusing in the other plane, it has been demonstrated in [23, 24], that a sequence of alternating quadrupoles can have an net focusing effect in both planes. The magnetic quadrupole field is of the form

$$\vec{B} = B_1 \begin{pmatrix} y \\ x \end{pmatrix}. \tag{1.5}$$

In analogy to the dipole strength $1/r$ in Eq. (1.4), the quadrupole strength is defined as

$$k = \frac{q}{p} B_1 = \frac{q}{p} \left. \frac{\partial B_y}{\partial x} \right|_{x=y=0}. \tag{1.6}$$

Equations of motion

Linear beam dynamics is restricted to drift spaces without magnetic fields and to dipolar and quadrupolar magnetic fields, which are either constant or depend linearly on the transverse coordinates. In linear approximation the equations of motion can be written in this case as

$$x''(s) + \left(\frac{1}{r(s)^2} - k(s)\right) x(s) = 0, \tag{1.7}$$

$$y''(s) + k(s)y(s) = 0, \tag{1.8}$$

with the derivatives after the longitudinal coordinate s, i.e. $x''(s) \equiv \mathrm{d}^2x/\mathrm{d}s^2$. $r(s)$ and $k(s)$ define the dipole and quadrupole fields along s. It is furthermore assumed that $B_z = 0$ and that all particles have the same momentum. The equation of motion for the vertical plane are equivalent to the horizontal plane in the absence of dipole fields. Hence, without omitting generality, the following derivations will be restricted to the horizontal plane. For the case of constant $r(s)$ and $k(s)$ a solution of the equations of motions can be written as [24]

$$x(s) = C(s)x_0 + S(s)x_0', \tag{1.9}$$

$$x'(s) = C'(s)x_0 + S'(s)x_0'. \tag{1.10}$$

$C(s), S(s)$ and their derivatives with respect to s, $C'(s)$ and $S'(s)$, whose form is shown later, describe the transfer of a particle with coordinates (x_0, x_0') at position s_0 to the position s with the new coordinates (x, x'). This expression is often written in matrix form as

$$\begin{pmatrix} x \\ x' \end{pmatrix} = \boldsymbol{M} \cdot \begin{pmatrix} x_0 \\ x_0' \end{pmatrix}, \tag{1.11}$$

where $\boldsymbol{M}$ is the transfer matrix, which describes the change of particle coordinates between two locations. This method can be extended from constant to step-wise constant functions $r(s)$ and $k(s)$, by multiplying the resulting transfer matrices for the constant ranges. The transfer matrix for a segment as in Fig. 1.5 can be written as

$$\boldsymbol{M}_{\text{segment}} = \boldsymbol{M}_5 \cdot \boldsymbol{M}_4 \cdot \boldsymbol{M}_3 \cdot \boldsymbol{M}_2 \cdot \boldsymbol{M}_1. \tag{1.12}$$

This is a good approach for accelerators, assuming that each magnet has a longitudinally constant magnetic field.

Courant-Snyder parameters

For solving the equation of motion (1.7) in circular accelerators, one can assume periodicity, i.e. $k(s) = k(s+L)$ and $r(s) = r(s+L)$. A solution of this so called Hill's

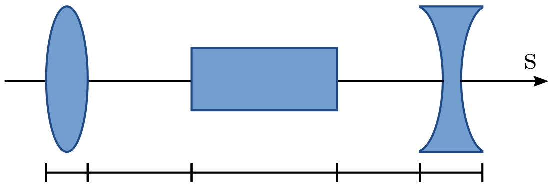

	$\boldsymbol{M}_1$	$\boldsymbol{M}_2$	$\boldsymbol{M}_3$	$\boldsymbol{M}_4$	$\boldsymbol{M}_5$
$k(s)$	k_1	0	0	0	$-k_1$
$r(s)$	∞	∞	r	∞	∞

Figure 1.5.: Illustration of a typical segment in an accelerator of a focusing quadrupole followed by a dipole and a defocusing quadrupole. The transfer matrices $\boldsymbol{M}_1$ to $\boldsymbol{M}_5$ denote the regions where constant magnetic fields along the longitudinal axis are assumed.

differential equation, can be written in the form of a harmonic oscillator with varying amplitude and phase

$$x(s) = A(s)\cos(\phi(s) + \phi_0). \tag{1.13}$$

In [24] the Courant-Snyder parameterization was introduced with

$$\beta(s) = \frac{A(s)^2}{\epsilon}, \tag{1.14}$$

$$\alpha(s) = -\frac{1}{2}\frac{\mathrm{d}\beta(s)}{\mathrm{d}s}, \tag{1.15}$$

$$\gamma(s) = \frac{1+\alpha(s)^2}{\beta(s)}. \tag{1.16}$$

The amplitude $A(s)$ of the particle oscillation around the design orbit is described by a constant part ϵ, which is called the emittance, and the β-function $\beta(s)$, which varies along the accelerator. This oscillation is referred to as the betatron oscillation and is illustrated in Fig. 1.6. Using the Courant-Snyder parameters the transfer matrix $\boldsymbol{M}$ from Eq. (1.11) can be written as

$$\boldsymbol{M}(s_0, s) = \begin{pmatrix} \sqrt{\frac{\beta(s)}{\beta(s_0)}}(\cos\Delta\phi + \alpha(s_0)\sin\Delta\phi) & \sqrt{\beta(s)\beta(s_0)}\sin\Delta\phi \\ \sqrt{\frac{1}{\beta(s)\beta(s_0)}}\left[(\alpha(s_0)-\alpha(s))\cos\Delta\phi - (1+\alpha(s)\alpha(s_0))\sin\Delta\phi\right] & \sqrt{\frac{\beta(s_0)}{\beta(s)}}(\cos\Delta\phi - \alpha(s)\sin\Delta\phi) \end{pmatrix}, \tag{1.17}$$

where $\Delta\phi = \phi(s) - \phi(s_0)$ is the phase advance of the betatron oscillation from s_0 to s. The phase at position s is defined defined as

$$\phi(s_i) = \int_0^{s_i} \frac{1}{\beta(s)}\mathrm{d}s. \tag{1.18}$$

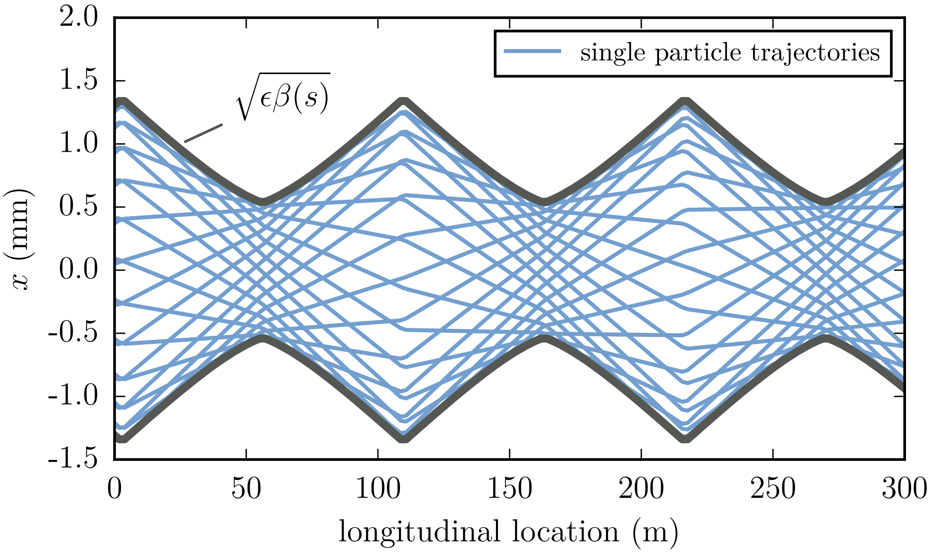

Figure 1.6.: Particle trajectories computed from Eq. (1.13). The maximum amplitude $\sqrt{\epsilon\beta(s)}$ defines an envelope for all particles with emittance ϵ.

The Courant-Snyder parameters can be propagated using a transfer matrix as well, whose elements are a combination of the transfer matrix elements from Eq. (1.11)

$$\begin{pmatrix}\beta\\ \alpha\\ \gamma\end{pmatrix} = \begin{pmatrix} C^2 & -2CS & S^2\\ -CC' & CS'+SC' & -SS'\\ C'^2 & -2C'S' & S'^2\end{pmatrix} \cdot \begin{pmatrix}\beta_0\\ \alpha_0\\ \gamma_0\end{pmatrix}. \tag{1.19}$$

Phase space

The solution of the Hill differential equation Eq. (1.13) and its derivative can be rewritten by removing the phase $\phi(s)$ to

$$\gamma(s)x(s)^2 + 2\alpha(s)x(s)x'(s) + \beta(s)x(s)'^2 = \epsilon, \tag{1.20}$$

which is defining an ellipse in the phase space for a particle with emittance ϵ. While the shape of this ellipse is changing along the accelerator depending on the optical functions β, α and γ, the area of this ellipse $A = \pi\epsilon$ is invariant. From one turn to another the particle position on the ellipse will change, depending on the phase advance for one revolution in the accelerator, cf. Fig. 1.7. This phase advance, normalized to 2π, is referred to as the tune Q.

$$Q_{x,y} = \frac{1}{2\pi}\oint \frac{1}{\beta_{x,y}(s)}\mathrm{d}s. \tag{1.21}$$

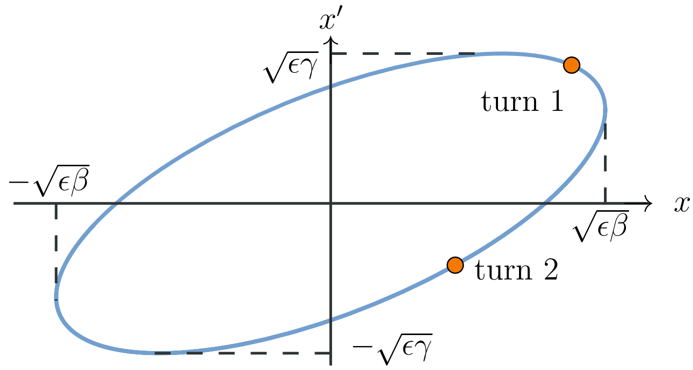

Figure 1.7.: The phase space ellipse defines the possible configurations of transverse position and angle for a particle with emittance ϵ. It is specified at a certain location in the accelerator by the local optical functions.

The beam emittance for an ensemble of particles with different single particle emittances is usually defined as the value for which the corresponding phase space ellipse contains a certain fraction of the particles. For a beam whose transverse particle density is described by a Gaussian distribution

$$\rho(x,y) = \frac{1}{2\pi\sigma_x\sigma_y}\exp\left(-\frac{x^2}{2\sigma_x^2} - \frac{y^2}{2\sigma_y^2}\right), \tag{1.22}$$

with the horizontal and vertical one standard deviation beam size $\sigma_{x,y}$, the beam emittance can be defined as

$$\epsilon_{x,y} = \frac{\sigma_{x,y}(s)^2}{\beta_{x,y}(s)}. \tag{1.23}$$

1.1.3. Perturbations and instabilities

In the previous section the linear beam dynamics were discussed under ideal conditions of the magnetic fields. In the following, the effect of deviations from design parameters is described.

Magnetic field imperfections

Higher order magnetic fields, where the field strength depends non-linearly on the transverse position of the particle, are referred to as non-linear magnetic multipoles. Purely transverse magnetic fields can be described with the following multipole expansion [25]

$$B_y + \mathrm{i}B_x = B_0 \sum_{n=1}^{\infty} (b_n + \mathrm{i}a_n)(x + \mathrm{i}y)^{n-1}, \tag{1.24}$$

with

$$b_n = \frac{1}{B_0(n-1)!} \frac{\partial^{n-1} B_y}{\partial x^{n-1}}\bigg|_{x=y=0} \quad \text{and} \quad a_n = \frac{1}{B_0(n-1)!} \frac{\partial^{n-1} B_x}{\partial x^{n-1}}\bigg|_{x=y=0}.$$

The order of the magnetic field is described by n, where $n = 1$ corresponds to a dipole, $n = 2$ to a quadrupole, $n = 3$ to a sextupole and so forth. If Eq. (1.24) is evaluated using Eq. (1.5) for a quadrupole field, the only non-zero component is b_2. If the quadrupole is rotated, a_2 would become non-zero as well, as in this case the horizontal field depends additionally on the horizontal particle position. Therefore, b_n are referred to as the normal multipole components and a_n the skew multipole components.
Due to imperfections of real magnets, higher order multipoles occur in every accelerator and perturb the beam dynamics.

The limitation for the particle oscillations due to the geometry of the beam pipe is referred to as the mechanical aperture. Certain oscillation amplitudes would cause a particle to interact with the material of the beam pipe and result in a loss of this particle from the beam.
Likewise, non-linear magnetic fields cause certain oscillation amplitudes to be unstable with the consequence of particle losses. Similar to the mechanical aperture, a dynamic aperture (DA) can be defined to describe the maximum oscillation amplitude for which a particle oscillation is stable in the presence of non-linear magnetic fields. Its value can be estimated with tracking simulations of particles through the accelerator for many turns[1]. The study and correction for these non-linear effects is of great interest for complex machines like the LHC.

$\boldsymbol{\beta}$-beating

Deviations from the design β-function occur due to focusing errors. The perturbed transfer matrix $\boldsymbol{M}_p$ due to a quadrupole error Δk at position s_0 can be derived by multiplying the unperturbed transfer matrix $\boldsymbol{M}$, cf. Eq. (1.11), with a matrix that describes the quadrupole gradient error

$$\boldsymbol{M}_p(s, s_0) = \begin{pmatrix} C_p & S_p \\ C'_p & S'_p \end{pmatrix} = \begin{pmatrix} C & S \\ C' & S' \end{pmatrix} \cdot \begin{pmatrix} 1 & 0 \\ -\Delta k & 1 \end{pmatrix} = \begin{pmatrix} C - \Delta k S & S \\ C' - \Delta k S' & S' \end{pmatrix}. \tag{1.25}$$

The perturbed β-function can be derived from Eq. (1.19) as

$$\beta_p(s) = \beta(s_0) C_p^2 - \alpha(s_0) 2 S_p C_p + \gamma(s_0) S_p^2. \tag{1.26}$$

[1]Computationally extensive tracking studies for 10^5 to 10^6 turns still only correspond to a few seconds to a few minutes of the operation time of the LHC.

Using Eqs. (1.17),(1.25) and (1.26) the perturbed β-function can be written as

$$
\begin{aligned}
\beta_p(s) =& \beta(s_0)\left\{\sqrt{\frac{\beta(s)}{\beta(s_0)}}\left[\cos\phi+\alpha(s_0)\sin\phi\right]-\Delta k\sqrt{\beta(s)\beta(s_0)}\sin\phi\right\}^2 \\
& -\alpha(s_0)2\sqrt{\beta(s)\beta(s_0)}\sin\phi \\
& \cdot\left\{\sqrt{\frac{\beta(s)}{\beta(s_0)}}\left[\cos\phi+\alpha(s_0)\sin\phi\right]-\Delta k\sqrt{\beta(s)\beta(s_0)}\sin\phi\right\} \\
& +\gamma(s_0)\left[\sqrt{\beta(s)\beta(s_0)}\sin\phi\right]^2 \qquad (1.27)\\
=& \beta(s)\left[\cos\phi^2+\cancel{2\alpha(s_0)\cos\phi\sin\phi}+\cancel{\alpha(s_0)^2\sin\phi^2}\right] \\
& -2\Delta k\beta(s)\beta(s_0)\cos\phi\sin\phi-\cancel{2\Delta k\beta(s)\beta(s_0)\alpha(s_0)\sin\phi^2} \\
& +\Delta k^2\beta(s)\beta(s_0)^2\sin\phi^2-\cancel{2\alpha(s_0)\beta(s)\sin\phi\cos\phi} \\
& -\cancel{2\alpha(s_0)^2\beta(s)\sin\phi^2}+\cancel{2\Delta k\beta(s)\beta(s_0)\alpha(s_0)\sin\phi^2} \\
& +\beta(s)\sin\phi^2+\cancel{\alpha(s_0)^2\beta(s)\sin\phi^2} \qquad (1.28)\\
=& \beta(s)\underbrace{\left[\cos\phi^2+\sin\phi^2\right]}_{=1}-\beta(s)\beta(s_0)\Delta k\sin(2\phi) \\
& +\Delta k^2\beta(s)\beta(s_0)^2\sin\phi^2. \qquad (1.29)
\end{aligned}
$$

With $\Delta\beta(s) = \beta_p(s) - \beta(s)$ follows

$$
\frac{\Delta\beta(s)}{\beta(s)} = -\beta(s_0)\Delta k\sin(2\phi)+\beta(s_0)^2\Delta k^2(\sin\phi)^2. \qquad (1.30)
$$

In linear order in Δk and in the general case of more than one error source, the resulting deviation of the β-function will be a superposition of Eq. (1.30) with different amplitudes and initial phases for each error source, the β-beating. According to [26] this oscillation will still propagate with the same phase advance, but with an in general unknown initial phase and amplitude. The β-beating propagation in regions with negligible focusing errors can be described by an oscillation with constant amplitude A, which propagates with twice the betatron oscillation phase advance

$$
\frac{\Delta\beta(s)}{\beta(s)} = A\cdot\sin(2\cdot\phi(s)+\phi_0). \qquad (1.31)
$$

A sudden change of the β-beating amplitude is an indicator for a strong focusing error at that location. This can be seen very clearly in measurements before optics corrections, for example in Fig. 3.21, where the β-beating amplitude changes significantly in IR1 and IR5.

Feed down

Magnetic multipole fields of higher order than quadrupoles can perturb the optics due to feed down effects. For a sextupole magnet with $b_3 \neq 0$, Eq. (1.24) gives

$$B_y = B_0 b_3 (x^2 + y^2), \tag{1.32}$$

with

$$b_2 = \frac{1}{B_0} \frac{\partial B_y}{\partial x}\bigg|_{x=y=0} = 2x b_3|_{x=y=0} = 0. \tag{1.33}$$

If this magnet is horizontally displaced by Δx, the field becomes

$$B_y = B_0 b_3 ((x + \Delta x)^2 + y^2). \tag{1.34}$$

This gives a non zero quadrupole component

$$b_2 = \frac{1}{B_0} \frac{\partial B_y}{\partial x}\bigg|_{x=y=0} = 2(x + \Delta x) b_3|_{x=y=0} = 2\Delta x b_3. \tag{1.35}$$

This effect is called feed down, which makes it necessary to consider misalignments of higher order magnetic fields for linear optics perturbations.

Dispersion

For the equations of motion Eqs. (1.7) and (1.8) it was assumed that all particles have the reference momentum p_0 as defined by the dipole field in Eq. (1.4). For small momentum deviations $\Delta p = p - p_0$ the equation of motion becomes

$$x''(s) + \left(\frac{1}{r(s)^2} - k(s) \right) x(s) = \frac{1}{R} \frac{\Delta p}{p_0}. \tag{1.36}$$

The solution of the homogeneous part $x_H(s)$ of this differential equation has been shown in the previous section, yielding Eq. (1.9). The periodic solution for the inhomogeneous differential equation can be written as

$$x(s) = x_H(s) + D(s) \frac{\Delta p}{p}, \tag{1.37}$$

with the dispersion function $D(s)$. It describes the additional transverse offset of a particle due to its momentum deviation. Often, the normalized dispersion is used, which is defined as

$$\eta(s_0) = \frac{1}{\sqrt{\beta(s_0)}} D(s_0) = \frac{1}{2\sin(\pi Q)} \int_{s_0}^{s_o+L} \frac{\sqrt{\beta(s)}}{\rho(s)} \cos(\phi(s) - \phi(s_0) - \pi Q) \mathrm{d}s, \tag{1.38}$$

as it is nearly constant for FODO cell latices [5].

Coupling

So far it was assumed that the horizontal and vertical plane can be treated independently. Equation (1.24) shows, that even a small rotational misalignment for a quadrupole introduces coupled motion in both planes. In this case the transfer matrix needs to be extended to

$$\begin{pmatrix} x \\ x' \\ y \\ y' \end{pmatrix} = \begin{pmatrix} \boldsymbol{M_x} & \boldsymbol{C_1} \\ \boldsymbol{C_2} & \boldsymbol{M_y} \end{pmatrix} \cdot \begin{pmatrix} x_0 \\ x_0' \\ y_0 \\ y_0' \end{pmatrix}, \tag{1.39}$$

where $\boldsymbol{M_{x,y}}$ are the 2×2 transfer matrices for each plane in the uncoupled case, and $\boldsymbol{C_{1,2}}$ the 2×2 matrices which describe the coupling effect. Coupling is the origin of further tune resonances, as described in the following paragraph, and reduces the DA [27]. Another effect of coupling prevents the fractional part of the two tunes to approach each other up to equality, i.e. there will be a minimum distance ΔQ_{min} [28]. This observable can be used to minimize the coupling effects by the use of skew quadrupoles [29].

Tune resonance

Equation (1.38) for the normalized dispersion already indicates that certain tune values need to be avoided. For integer tune values, i.e. $Q = n$, with $n \in \mathbb{N}$, $\eta(s)$ would become infinitely large, due to $\sin(\pi Q)$ in the denominator. As it describes the transverse particle offset, no stable motion would exist even for the smallest momentum deviations.

The same can be shown for the case of magnetic field errors instead of momentum deviations [4]. Higher order field errors additionally excite tune resonances described by $mQ = n$, with $(m, n) \in \mathbb{N}^2$, for a resonance of m^{th} order. As a result of coupling of the horizontal and vertical plane further resonances can be excited if $m_1 Q_x + m_2 Q_y = n$ is fulfilled with $(m_1, m_2, n) \in \mathbb{N}^3$.

Due to the shared vacuum pipe for both beams around the IPs, bunch encounters in the vicinity of the IP and especially the head-on collisions lead to a defocusing of the particles in a bunch, which effectively causes tune shifts, also referred to as beam-beam tune shifts [30, 31]. The tune working point of an accelerator needs to be chosen such that the relevant resonance lines are not crossed by the resulting spread of possible tunes inside a bunch. For the LHC resonances up to the 12^{th} order have been considered. An intriguing method to describe the resonance lines uses Farey sequences [32], which have been used to draw the tune diagrams in Fig. 1.8.

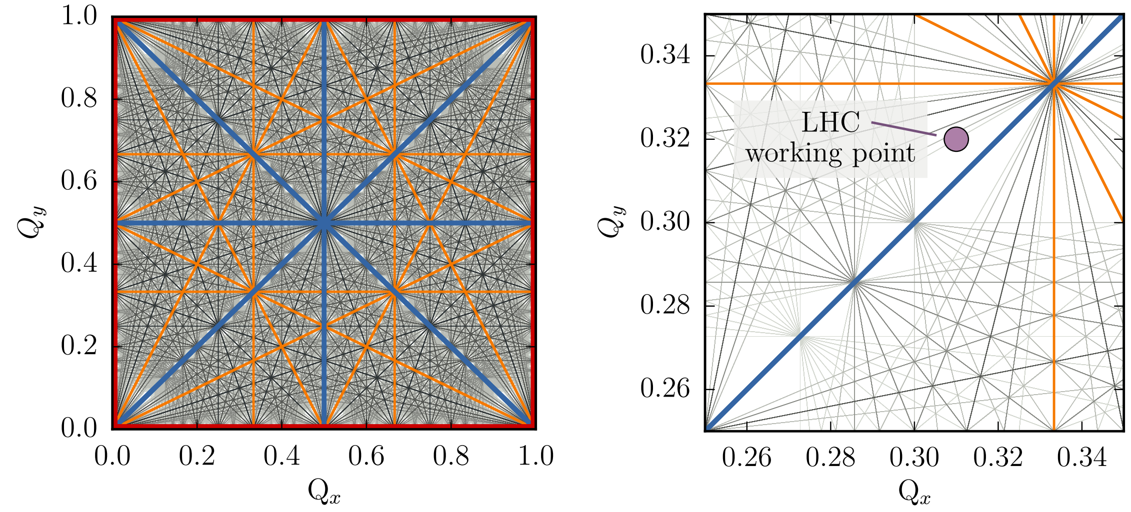

Figure 1.8.: Full tune diagram (left) and a zoom around the LHC working point (right) for resonances up to the 12$^{\text{th}}$ order. The first order (red), second order (blue) and third order (orange) resonances are highlighted with colors. Higher order resonances are drawn with decreasing line widths and brighter gray tones.

Chromaticity

Equation (1.6) shows that the focusing strength of a quadrupole depends on the particle momentum. Hence, a particle with a momentum deviation will experience a different focusing strength, which will result in a change of the tune for this particle. Chromaticity describes the overall tune change for the whole accelerator and is defined as

$$\xi = \frac{\Delta Q}{\Delta p/p} = \frac{1}{4\pi} \oint k(s)\beta(s)\mathrm{d}s. \tag{1.40}$$

The biggest contribution comes from magnets with large quadrupole strength $k(s)$ at locations where the β-function is large as well. The absolute value of the chromaticity is desired to be small, as it is the scaling factor to relate a momentum spread to a tune spread. A large tune spread potentially crosses resonance lines in the tune diagram, and could therefore cause unwanted beam losses.

The chromaticity can be controlled with sextupole magnets [33], and for the LHC a small positive value is chosen, as this avoids the head-tail instability [34].

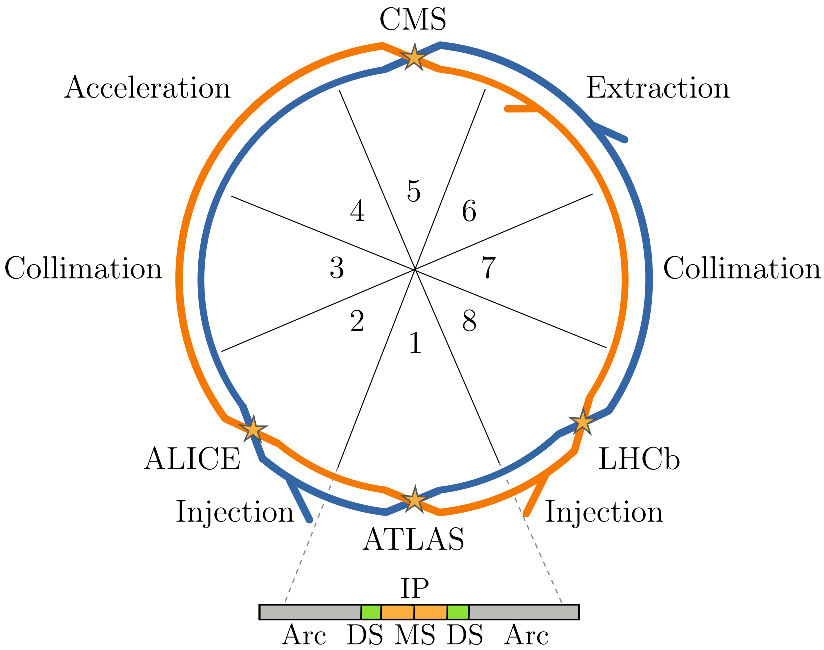

Figure 1.9.: Layout of the LHC illustrating the eight octants. In each octant the purpose of its IR is shown. The crossing of beam 1 (blue) and beam 2 (orange) is indicated in the four experimental insertions. For octant 1 the sequence of arcs, dispersion suppression (DS) and matching section (MS) with the interaction point (IP) in the center, is shown.

1.1.4. Magnet lattice design

The LHC has been placed in a tunnel which was used before for the Large Electron-Positron Collider (LEP). Its circumference of 27 km was defined by this constraint. The LHC can be divided into eight octants, and consists of eight bending sections, the arcs, which are separated by eight straight sections. The straight sections, also referred to as insertion regions (IRs), serve a specific purpose such as housing an experimental detector, beam acceleration, beam collimation and beam extraction, cf. Fig. 1.9. Each of the IRs has different requirements for the beam optics which will be described in the following paragraphs.

Arcs

The main purpose of the arcs is to bend the beam around the circular design orbit. The optics design in the arcs needs to weigh up between achieving a high integrated dipole field, while keeping a small beam size to reduce the aperture requirements in the dipole magnets [14]. For round beams, i.e. $\epsilon_x \approx \epsilon_y$, the optimal phase advance per

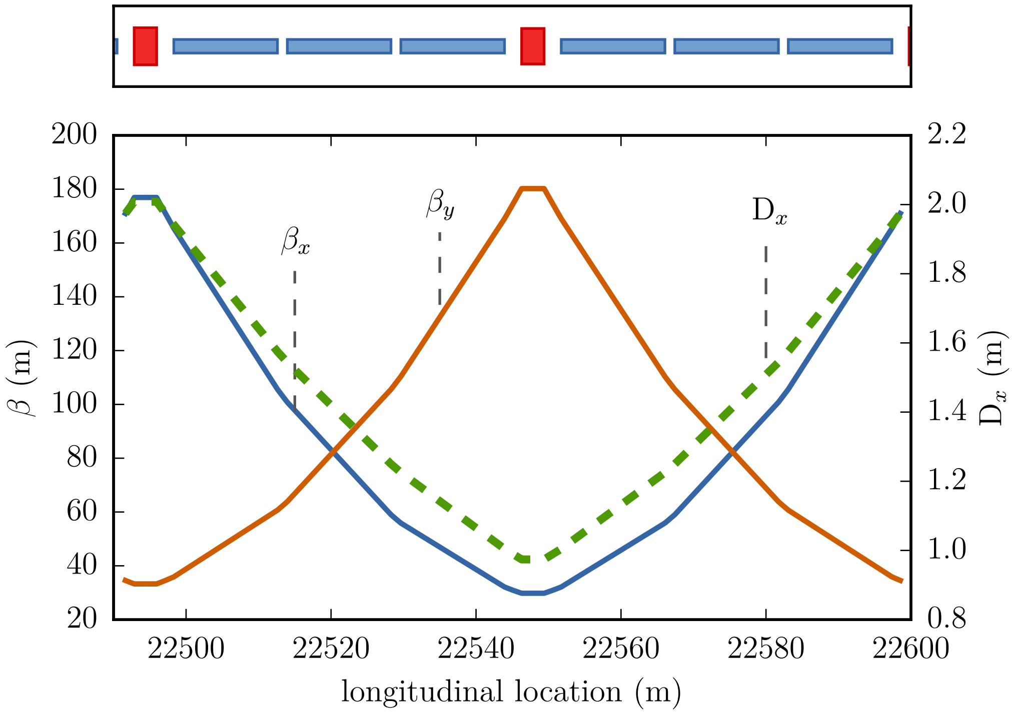

Figure 1.10.: β-function and horizontal dispersion in an LHC arc FODO cell. The top graph indicates the position of dipole (blue) and quadrupole (red) magnets.

FODO cell for minimizing the beam size in both planes is 90° [35]. This defines the product $k \cdot \Delta s$ of the quadrupole strength k and distance Δs between two quadrupoles. A larger FODO cell is preferred to increase the integrated dipole field in the arc, however the maximum length is limited by the optics stability in the presence of field errors [36]. For the LHC a FODO cell length of 107 m has been chosen, and each arc consists of 23 of these cells. The dispersion which is created in the arcs due to the dipole fields needs to be reduced, as it is unwanted in the insertion regions. A dispersion suppressor section is connecting each arc with the IRs, which uses the missing dipole scheme together with individually powered quadrupole magnets to correct the dispersion [35].

Experimental IRs

Four IRs in the LHC are housing experiments. The two high-luminosity experiments are the ATLAS detector in IR1 and the Compact Muon Solenoid (CMS) in IR5. Two medium-luminosity experiments, A Large Ion Collider Experiment (ALICE) and

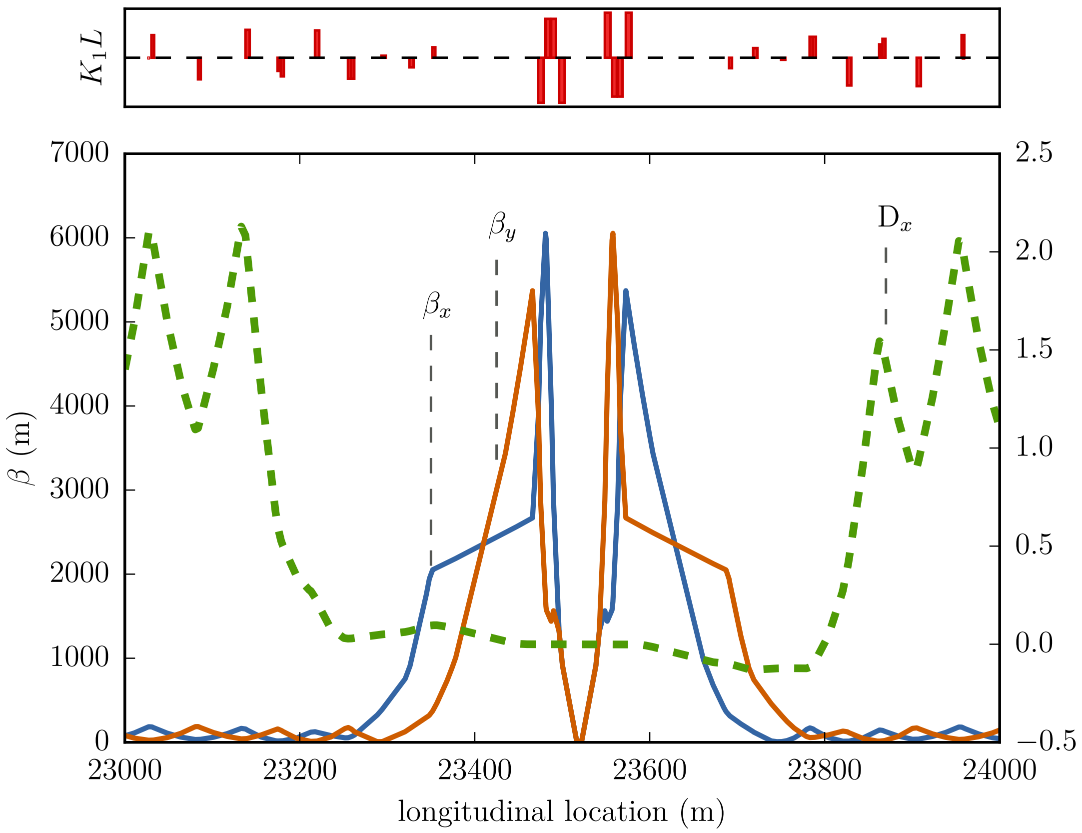

Figure 1.11.: β-function and horizontal dispersion in IR1 for a β^* of 40 cm. The top graph indicates the position of quadrupole magnets and their integrated field gradient (K_1L). The IP is surrounded by the final focusing triplet magnets.

Large Hadron Collider beauty (LHCb), are located in IR2 and IR8. The luminosity for each experiment depends according to Eq. (1.1) on the transverse beam size at the IP, which is related to the β-function at this point (β^*), cf. Eq. (1.23). All experimental IRs share the requirement on the optics of allowing for different β^* without changing the overall phase advance for the IR. Characteristic for the optics with low β-functions at the IPs are the large β-functions at the three final focusing quadrupole magnets (triplet), cf. Fig. 1.11. Close to the IP no beam focusing can be performed as this space is occupied by the detector. From Eq. (1.19) one can derive the evolution of the β-function around the IP, where $k(s) = 0$, $r(s) = \infty$ and $\alpha \equiv 0$, as it is the location of the minimum β-function

$$\beta(s) = \beta^* + \frac{s^2}{\beta^*}. \tag{1.41}$$

For a distance from the IP to the first quadrupole (L^*) of 23 m, as in the LHC, and $\beta^* = 0.4\,\mathrm{m}$ the approximated β-function at the beginning of the quadrupole becomes $\beta(L^*) = 1322\,\mathrm{m}$. Since the first quadrupole focuses only in one plane and defocuses in the other one, even larger β-functions occur in the following quadrupole of the triplet. These magnets are therefore prone for introducing a large β-beating. Furthermore, the minimum β^* is limited by the more rapidly increasing β-functions and thereby larger transverse beam sizes in the triplet magnets.

Non-experimental IRs

IR3 and **IR7** comprise the collimation system for beam cleaning. The collimation system uses a two-step approach. In IR3 the momentum cleaning takes place, ensuring that a certain momentum deviation is not exceeded by the beam particles. Therefore, it is desired to have a large normalized dispersion $\eta_x = D_x/\sqrt{\beta_x}$, so that the transverse offset of the particles is dominated by their momentum deviation [37]. Particles exceeding a certain transverse offset are then intercepted by the collimators [37]. In IR7 the betatron collimation is done, where particles with too large betatron oscillation amplitudes are intercepted. Due to similar consideration, in this case a very low normalized dispersion is needed at the collimator positions. Furthermore, specific phase advances between two collimators are crucial for the efficiency of this system [38, 39].

IR4 includes the rf cavities for beam acceleration. Inside the cavities a small dispersion is desired.

In **IR6** the extraction of the beam at the end of a physics fill, or due to unexpected problems or instabilities is performed. It includes a larger drift space between the extraction kicker and septum magnet, in order to reduce the required strengths of these magnets. This results in larger β-functions and constrains the aperture of the system elements [40].

1.1.5. Operational cycle

In this section the operational cycle of the LHC is described with a focus on the different optics that are used in each stage. A typical cycle is illustrated in Fig. 1.12. Particles are injected into the LHC at an energy of $\mathrm{E_{inj}} = 450\,\mathrm{GeV}$. The optics during injection have a β^* in the experimental IRs of (10–11) m. Furthermore, the tune working point is different from the one described in Fig. 1.8, with the fractional tunes $Q_x = 0.28$ and $Q_y = 0.31$. Tracking studies have shown that these tunes improve the DA at injection [41]. Moreover, it reduces the effect of coupling errors [42].

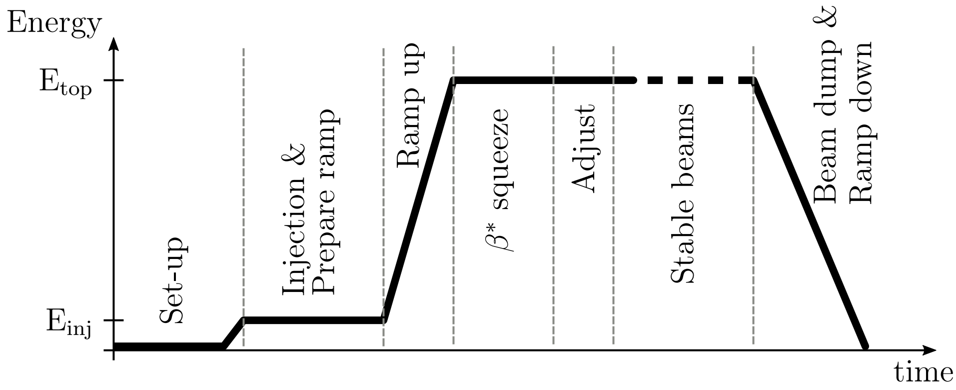

Figure 1.12.: Illustration of the LHC operational cycle.

Table 1.1.: Top energy over time for the LHC.

Year	$\mathbf{E_{top}}$ **(TeV)**
up to 2011	3.5
2012	4.0
from 2015	6.5

During the energy ramp particles will be accelerated, while the gradients of the magnets are increased, which ensures the same beam orbit and focusing. The maximum particle energy, also referred to as top energy, has increased over the years, as shown in Table 1.1.

After the energy ramp, the optics are the same as at injection. This state is often referred to as flattop.

In a next step the β-functions at the experimental IPs are reduced, which is called the β^* squeeze. This is necessary to increase the luminosity for collisions, cf. Eq. (1.1). After a change to the fractional tunes for collision of $Q_x = 0.31$ and $Q_y = 0.32$, and after final adjustments, stable beams will be declared.

At the end of a physics fill, the beam will be extracted, and the magnets will be ramped down to prepare for the next cycle.

1.2. Optics measurement techniques

Deviations from the model lattice, which arise from imperfection of magnetic fields and misalignment of the elements, have potentially negative effects for the accelerator performance. Equation (1.30) shows how a quadrupole field error results in an oscillating deviation of the β-function, a β-beating wave. Accelerators with strong focusing magnets, as for example particle colliders which need to achieve small beam sizes in the interaction points, cf. Fig. 1.11, will experience larger deviations of the β-function, due to the large β-functions at the focusing quadrupoles. The maximum tolerable β-beating for the LHC due to machine imperfections is shown in Table 1.2. Measurements of the LHC optics before corrections show β-beating values of up to

Table 1.2.: Maximum tolerable β-beating due to machine imperfections as specified in [43].

Optics	**Peak $\Delta\beta/\beta$ (%)**	
	horizontal	**vertical**
Injection	14	16
Collision	15	19

100 %, cf. Appendix B.2. The lower the β^* is, which is one way to increase the luminosity, cf. Eq. (1.1), the larger the β-beating due to machine imperfections becomes. It is therefore crucial for the operation of the LHC, to measure and correct the optics. In the following chapters, three optics measurement techniques, which are relevant for the context of this thesis, will be introduced. A more detailed review of the different optics measurement methods is given in [44].

1.2.1. Turn-by-turn orbit

Turn-by-turn (TbT) optics measurements are based on probing the betatron oscillation with the measurement of the transverse beam center position for many consecutive turns. The betatron oscillation for single particles, described by Eq. (1.13), is difficult to measure, as it is superposed by the oscillation of other particles in the beam with different initial phases. Therefore, the whole beam needs to be displaced in the phase space, so that the beam center is performing betatron oscillations. The oscillations are excited either by a single turn dipole field from a kicker magnet, or a continuous excitation using an alternating current (ac) dipole [45]. The latter has the advantage of adiabatically increasing and decreasing the excitation amplitude, which prevents to increase the beam emittance [46]. The TbT data are recorded using beam position monitors (BPMs) [47], of which the LHC is equipped with more than 500 per plane and per beam [48]. TbT measurements are very fast, as the beam excitation and data recording takes only a few seconds, and is done in parallel for all BPMs.
The large amount of BPMs allows furthermore for an efficient noise reduction of the TbT data, using a singular value decomposition (SVD) technique for filtering uncorrelated signals [49].

β-function from phase

The method to derive β-functions from the phase advance of the betatron oscillation has been developed at LEP [50, 51]. According to Eqs. (1.13) and (1.21), the TbT data which is recorded at a specific location by a BPM is of the form

$$x_i = A\cos(2\pi Q i + \phi_0) + x_{\mathrm{CO}}, \tag{1.42}$$

where i is the turn number and x_{CO} the closed orbit offset at this position. The two sums

$$C = \sum_{i=0}^{N-1} x_i \cos(2\pi Q i) \quad \text{and} \quad S = \sum_{i=0}^{N-1} x_i \sin(2\pi Q i), \tag{1.43}$$

can be approximated for large number of turns to

$$C = \frac{AN}{2}\cos(\phi_0) \quad \text{and} \quad S = -\frac{AN}{2}\sin(\phi_0). \tag{1.44}$$

This allows to derive the phase of the betatron oscillation at the BPM position

$$\phi_0 = -\arctan\left(\frac{S}{C}\right). \tag{1.45}$$

Hence, the measurement of the phase is not influenced by an offset of the beam or a wrong excitation amplitude due to BPM calibration errors. The phase of the betatron oscillation can be derived by this harmonic analysis at every BPM position. With the phase advances and the model transfer matrix in between three BPMs, the β-function can be calculated at the position of the three BPMs [50, 51]. The Courant Snyder parameters β_i and α_i at the positions s_i are obtained with

$$\beta_i = \frac{\epsilon_{ijk}\cot(\phi_{i,j}) + \epsilon_{ikj}\cot(\phi_{i,k})}{\epsilon_{ijk}\frac{M_{11(i,j)}}{M_{12(i,j)}} + \epsilon_{ikj}\frac{M_{11(i,k)}}{M_{12(i,k)}}} \tag{1.46}$$

and

$$\alpha_i = \frac{\epsilon_{ijk}\frac{M_{11(i,k)}}{M_{12(i,k)}}\cot(\phi_{i,j}) + \epsilon_{ikj}\frac{M_{11(i,j)}}{M_{12(i,j)}}\cot(\phi_{i,k})}{\epsilon_{ijk}\frac{M_{11(i,j)}}{M_{12(i,j)}} + \epsilon_{ikj}\frac{M_{11(i,k)}}{M_{12(i,k)}}}, \tag{1.47}$$

where $\phi_{i,j} = \phi_j - \phi_i$ is the phase advance and $M_{mn(i,j)}$ are the model transfer matrix elements from s_i to s_j, cf. Fig. 1.13. ϵ_{ijk} is the Levi-Civita symbol which allows for a compact notation of the three cases of deriving the Courant Snyder parameters at the different BPMs. No summation over equal indices is implied. In case of using an ac dipole for the beam excitation, the forced oscillation will differ from the free oscillation [52, 53]. The effect on the analysis of the β-function can be corrected by introducing a quadrupole error in the optics model at the ac dipole position [54].

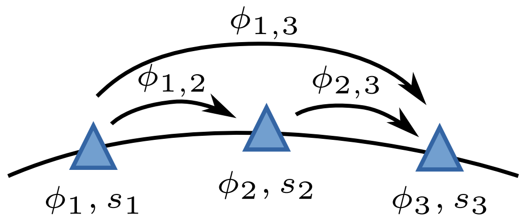

Figure 1.13.: Illustration of the β-function measurement from phase. The phase advances $\phi_{i,j}$ in between three positions s_i are needed to derive the β-functions at those positions.

$\boldsymbol{\beta}$-function from amplitude

The β-function can furthermore be derived from the amplitude of the excited betatron oscillation. The amplitude from Eq. (1.13) can be written as

$$A(s) = \sqrt{2J\beta(s)}, \tag{1.48}$$

with the action J, which depends on the strength of the beam excitation. The equation is similar to Eq. (1.14) for the single particle emittance. The action, which is an invariant, can be computed by evaluating the following average around the ring

$$2J = \left\langle \frac{A(s)^2}{\beta_m(s)} \right\rangle, \tag{1.49}$$

using the model β-functions $\beta_m(s)$. This introduces a systematic error as the real average β-function might deviate from the model. For the LHC at injection optics this effect is below 0.5 % for an rms β-beating up to 12 % [55]. For collision optics with a β^* of 40 cm however this effect introduces a systematic error of 4 % for the same rms β-beating, cf. Fig. 1.14.
Additionally this method relies on an accurate calibration of the BPMs. According to Eq. (1.48), the uncertainty of the derived β-function would be twice as large as a linear scaling uncertainty at the BPM, i.e. a 1 % uncertainty in the BPM calibration would result in a 2 % uncertainty of the β-function.

Further derivable quantities

TbT measurements are very versatile, as they allow to derive many more quantities. This includes e.g. coupling [56–58] or the tune change for larger oscillation amplitudes (detuning with amplitude) [59, 60]. By performing the measurements for different rf settings of the accelerating cavities, off momentum effects can be probed. Dispersion can be computed by observing the orbit change due to the induced momentum change according to Eq. (1.37). Furthermore, chromaticity, chromatic coupling [61, 62] and chromatic β-functions [63, 64] can be derived.

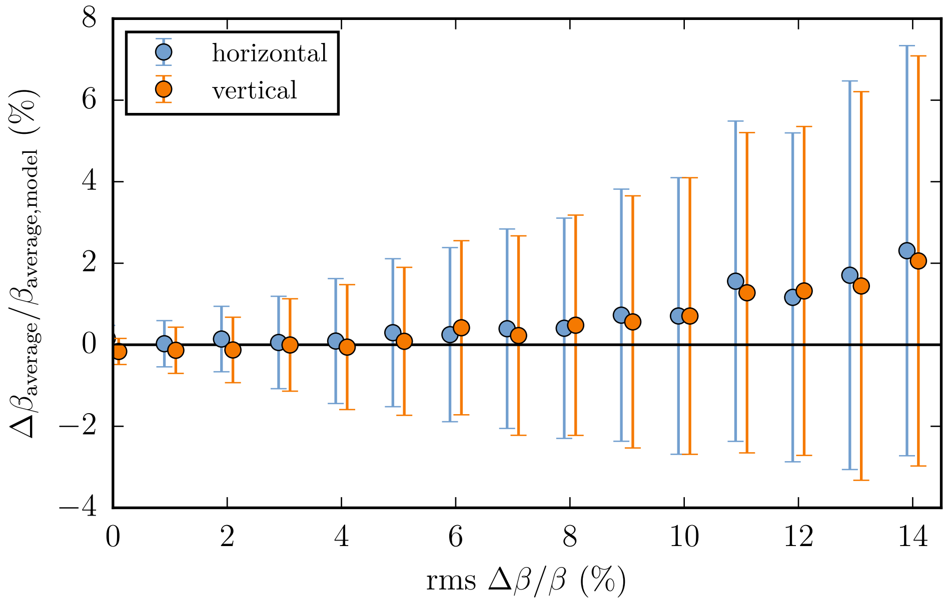

Figure 1.14.: The relative deviation of the average β-function from the model value is shown for different lattices where quadrupole errors were introduced for the LHC optics with $\beta^* = 40\,\text{cm}$. The data has been binned in steps of 1 % according to the rms β-beating.

1.2.2. K-modulation

A method to derive the β-function at the position of quadrupole magnets varies their integrated field, while observing the resulting tune change. It is called k-modulation as the quadrupole strength k from Eq. (1.6) is varied.
The expected tune change can be computed by multiplying the transfer matrix for a complete revolution in the accelerator with a transfer matrix which describes the perturbation of the quadrupole field changes, cf. [29]. Solving this equation for the β-function yields

$$\beta_{x,y} = \pm\frac{2}{\Delta k}\left[\cot(2\pi Q_{x,y})\left\{1-\cos(2\pi\Delta Q_{x,y})\right\}+\sin(2\pi\Delta Q_{x,y})\right], \tag{1.50}$$

with the tune change $\Delta Q_{x,y}$ for a quadrupole strength change Δk. The $\pm$ sign differentiates the solution for the horizontal and vertical plane. For small $\Delta Q_{x,y}$ and for an unperturbed tune $Q_{x,y}$ which is far from an integer or half integer value the equation can be approximated to

$$\beta_{x,y} \approx \pm 4\pi\frac{\Delta Q}{\Delta k}. \tag{1.51}$$

K-modulation measurements can only be performed at individually powered quadrupole magnets. In the LHC, these measurements are performed for example at the final focusing triplet for the computation of the β^* [65, 66].

1.2.3. LOCO

Small dipole corrector magnets can be used to introduce deflection angles Θ_i at the position s_i, which results in a deviation of the closed orbit [24]

$$\Delta x(s) = \frac{\sqrt{\beta(s)}}{2\sin(\pi Q)}\Theta_i\sqrt{\beta(s_i)}\cos(\phi(s) - \phi(s_i) - \pi Q). \tag{1.52}$$

An orbit response matrix can be constructed for every available corrector dipole, with the measured closed orbit deviation at every BPM position. Linear optics from closed orbit (LOCO) allows to fit for example quadrupole gradient changes in an accelerator model by minimizing the deviations of the measured and the model orbit response matrices [67]. LOCO is the standard method for optics measurements at many storage rings [68–73]. LOCO is used at the LHC as well, especially for transfer lines and injection tests [74]. For an optics fit of the whole machine however this method becomes very time-consuming due to the large size of the LHC [75].

1.3. Optics correction methods

Optics corrections for the LHC are performed in two steps. First, strong local error sources in the IRs are corrected, which come mainly from the final focusing triplet magnets. In a second iteration global corrections are computed using a response matrix approach. These methods are described in the following chapters.

1.3.1. Correction of strong local error sources

The segment-by-segment (SbS) technique was developed at the LHC for the computation of optics corrections for local, strong error sources [76]. The concept is to model the optics in a part of the accelerator in between two BPM locations, and is usually done for the different IRs. The optical functions which were derived from measured TbT data at the BPMs are the start parameters. The propagation inside the segment is done by using the optics modeling tool MAD-X [77]. For optics corrections the simulated phase advances between BPMs are compared to the measured ones, as they are more directly observable than e.g. the β-function. Possible correction settings aim at eliminating the deviations in the phase advance, which is illustrated in Fig. 1.15. This method has been very successful at finding local optics corrections

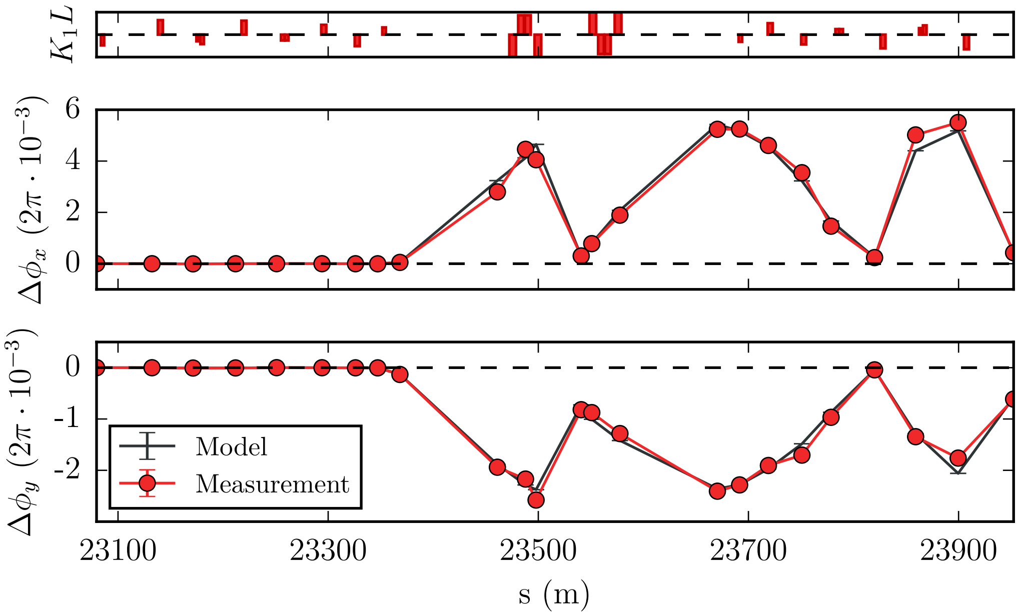

Figure 1.15.: The simulated measurement of the phase advance deviation between consecutive BPMs is shown for one IR. On the top of the plot the position of quadrupole magnets is illustrated with the two triplets around the center where the IP is. An artificial error in a magnet results in a periodic deviation of the phase advances starting at that magnet position (red line). The gradients in the lattice model in MAD-X are adjusted to reproduce the observed deviations (black line). Applying these gradients with negative sign will correct these deviations.

for the LHC, where it was once even able to identify a cable swap between the two beam apertures in a quadrupole which caused an unexpectedly large β-beating [64, 78]. SbS was also successfully tested at the Relativistic Heavy Ion Collider (RHIC) and is fully implemented there [79].

To facilitate finding optics correction, an automatic routine has been developed to fit the measured and simulated phase advances [80, 81].

Another purpose of SbS is the propagation of optical functions from the BPM positions to other lattice elements. This allows for example to derive the β^*. It has also been used to propagate the optical functions to beam wire scanners for an emittance study [82] and to collimators for a comparison to beam sizes as they are measured in beam-based collimator alignment [83]. These studies require very precisely measured β-functions and improvements to SbS were required to comply with these demands.

Previously, the uncertainties in SbS were only roughly estimated by running two

MAD-X simulations where the start parameters were changed once by adding their uncertainty and once by subtracting it. This is also more time consuming than the evaluation of analytic equations, since more MAD-X runs are necessary. For a tool which is used online during optics measurements, time efficiency is very important to ensure an efficient use of the beam time. An improved error propagation for the phase advance, the β- and the α-function and for coupling was implemented as shown in [84].

1.3.2. Effective global corrections

Global corrections are computed using a response matrix method. Based on an ideal model, the response matrix $\boldsymbol{R}$ which relates the change of quadrupole gradients to a deviation of the optics is constructed using MAD-X simulations [85]

$$\boldsymbol{R}\Delta\vec{k} = (\Delta\vec{\phi}, \Delta\vec{\eta}, \Delta Q_x, \Delta Q_y). \tag{1.53}$$

Again, instead of the β-function, the phase advances are used, as they are a more direct observable. Based on the measured optics parameters, the quadrupole strengths of the correction $\vec{k}_{\text{corr}}$ can be computed as

$$\Delta\vec{k}_{\text{corr}} = -\boldsymbol{R}^{-1}(\omega_\phi \Delta\vec{\phi}_{\text{meas}}, \omega_D \Delta\vec{\eta}_{\text{meas}}, \omega_Q \Delta Q_{x,\text{meas}}, \omega_Q \Delta Q_{y,\text{meas}}), \tag{1.54}$$

where $\boldsymbol{R}^{-1}$ is the generalized inverse of the response matrix and ω_i weights which can be assigned to the different parameters.

2. *N*-BPM method

The N-BPM method is based on the calculation of β-functions from the phase information of TbT orbit measurements, recorded at BPMs, which was introduced in Section 1.2.1. The accuracy of this method depends on the knowledge of the optics model, the precision of the measured phase, and also on the value of the phase advances between the BPMs. From Eq. (1.46) it can be seen that, for example, a phase advance between two BPMs should not be close to a multiple of π, as the cotangent becomes infinite at those points. Figure 2.1 shows the propagated error of the β-function for a specific location in the LHC, depending on the phase advances between the three BPMs.

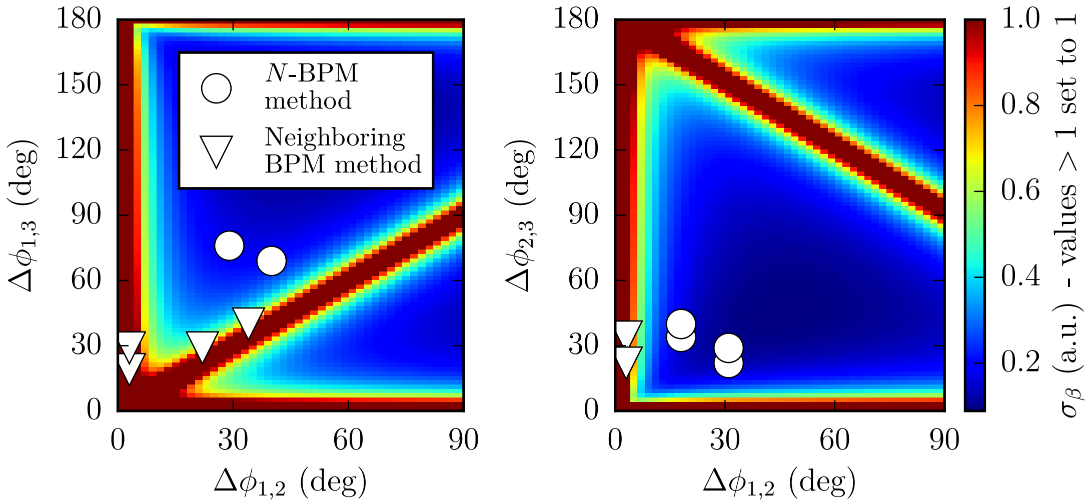

Figure 2.1.: Expected error of a measured β-function at position s_1, depending on the phase advances to the other two BPMs. The six used phase advances (three BPM combinations each, for the horizontal and vertical plane) for a BPM position in IR4 from the neighboring BPM method are indicated by triangles. When an increased range of 7 BPM is used (N-BPM method), 15 different combinations of phase advances are possible per plane, including the ones that are indicated by triangles. Six better suited combinations from the range of 7-BPMs are indicated by circles.

From Eq. (1.46) one can derive two conditions for the optimal phase advances. The phase advance from the probed BPM (i) to the other two (j,k) should be

$$\begin{aligned} \phi_{i,j} &= \frac{\pi}{4} + n_1 \frac{\pi}{2}, \\ \phi_{i,k} &= \frac{\pi}{4} + (2n_2 + 1 - n_1)\frac{\pi}{2}, \end{aligned} \qquad (n_1, n_2) \in \mathbb{Z}^2. \tag{2.1}$$

The method that has been used so far uses three neighboring BPMs for the calculation of the β-functions at these three BPM positions. In the LHC arcs, cf. Section 1.1.4, where in general the phase advance between consecutive BPMs is about $\pi/4$, this method is already close to the optimum configuration, when probing the middle BPM. However, in the case that the probed BPM is not in the middle of the other two BPMs, the optimum would be to skip the farther BPM and use instead the next following BPM, as shown in Fig. 2.2.

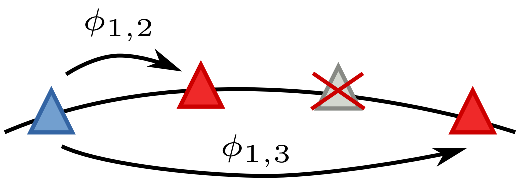

Figure 2.2.: In the arcs the phase advance between two consecutive BPMs is about $\pi/4$. If the blue BPM is probed, it is better to skip the grey BPM and use the two red BPMs. The resulting phase advances are approximately $\phi_{1,2} = \pi/4$ and $\phi_{1,3} = 3\pi/4$, which is the optimum according to Eq. (2.1).

In the IRs, the phase advances between BPMs can be very different, as the optics do not follow the regular FODO structure of the arcs in order to fulfill other constraints, cf. Section 1.1.4. For example in the ATLAS and CMS IRs, where the β-function reaches very high values, the phase advances between consecutive BPMs close to the IPs may only be a few degrees. If in this case only neighboring BPMs are used, this results in large uncertainties, which prevented β^* measurements at the IPs in 2012 [64].

An improved algorithm is developed here, which allows to use more BPM combinations from a larger range of BPMs. This makes it possible to include BPM combinations with better phase advances and also increases the amount of information that is used in the measurement of the β-function. A range of N BPMs is chosen, as illustrated in Fig. 2.3. The amount m of possible combinations of three BPMs, out of N BPMs with one fixed BPM, is

$$m = \frac{(N-1)(N-2)}{2}. \tag{2.2}$$

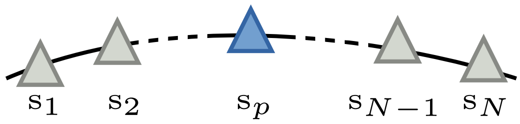

Figure 2.3.: In the N-BPM method, N BPMs at position s_1 to s_N are used to derive the β-function at a probed BPM at position s_p. The probed BPM is usually set at the center of the N BPMs, as optics errors decrease the gain of using further BPMs in both directions.

To find the best estimate of the real β-function out of the β-functions β_i, which are inferred from the m combinations of three BPMs, a least squares minimization is performed. It considers the residuals $\beta_i - \hat{\beta}$, where $\hat{\beta}$ is the estimate of the real β-function. The least square method minimizes the squared residuals, which can be weighted if the individual uncertainties σ_i of the β_i are known

$$S(\hat{\beta}) = \frac{(\beta_i - \hat{\beta})^2}{\sigma_i^2} \tag{2.3}$$

The more general case which includes correlations between the different β_i is described in [86], and the function to minimize can be written as

$$S(\hat{\beta}) = \sum_{i=1}^{m} \sum_{j=1}^{m} (\beta_i - \hat{\beta}) \boldsymbol{V}_{ij}^{-1} (\beta_j - \hat{\beta}), \tag{2.4}$$

where $\boldsymbol{V}_{ij}$ are the elements of the covariance matrix for the different β_i.
Therefore, the minimization of $S(\hat{\beta})$ is considering the individual uncertainties and correlations of the β_i from the m different BPM combinations, which allows for a better estimate of the β-function. The measured β-function at the probed BPM position is a weighted average of the m β-functions

$$\beta = \sum_{i=1}^{m} w_i \beta_i. \tag{2.5}$$

From the minimization of Eq. (2.4) one can derive the weights

$$w_i = \frac{\sum_{k=1}^{m} \boldsymbol{V}_{ik}^{-1}}{\sum_{k=1}^{m} \sum_{j=1}^{m} \boldsymbol{V}_{jk}^{-1}}. \tag{2.6}$$

This equation replaces the simple average introduced in [76]. The uncertainty for this measurement is

$$\sigma_\beta^2 = \sum_{k=1}^{m} \sum_{j=1}^{m} w_j w_k \boldsymbol{V}_{jk}. \tag{2.7}$$

The covariance matrix $\boldsymbol{V}$ is an element-wise sum of the covariance matrices for the systematic and statistical errors [87]

$$\boldsymbol{V}_{ij} = \boldsymbol{V}_{ij,stat} + \boldsymbol{V}_{ij,syst}. \tag{2.8}$$

For this method it is fundamental to have a precise knowledge of these covariance matrices, which will be derived in the following sections.

2.1. Statistical uncertainties

If Eq. (1.46) is used to derive the β-function, two phase advances between BPMs are used ($\phi_{i,j}$, $\phi_{i,k}$) in which the BPM (i) appears twice. This introduces a correlation which must be regarded in the error propagation, since the same phase measurement at BPM (i) was used in the calculation of both phase advances. More correlations will occur when the BPM combinations to calculate the different β_i in Eq. (1.14) have common BPMs, which all contribute to the covariance matrix $\boldsymbol{V}_{stat}$.
The error of the measured phase advance can be derived from the standard deviation of n measurements

$$\sigma_{\phi_{i,j}} = t(n)\sqrt{\frac{1}{n-1}\sum_{k=1}^{n}\left(\overline{\phi_{i,j}} - \phi_{i,j,(k)}\right)^2}, \tag{2.9}$$

where $\overline{\phi_{i,j}}$ is the average phase advance from BPM (i) to (j) and $t(n)$ is the t value correction from the Student's t distribution, which compensates the underestimation of the uncertainty for a small sample size. During the LHC Run I the error was calculated from a normal standard deviation without the t value correction and by dividing the sum by n instead of (n-1). This has been changed, since the mean value of the phase advance is also obtained from the measurements, and there are only (n-1) degrees of freedom left for the calculation of the standard deviation. Table 2.1 shows $t(n)$ for different amount of measurements, which shows that this correction is needed, since due to constraints on the available beam time, the amount of measurements is always limited.
The correlation between two phase advances which have one BPM in common, $\phi_{i,j}$ and $\phi_{i,k}$, depends on the uncertainty of the single phase ϕ_i at the common BPM. The error of the single phase ϕ_i is not known, because it cannot be compared among the measurement results, since its value is arbitrary and may vary. One can use the ansatz $\sigma_\phi \sim \beta^{-\frac{1}{2}}$ as shown in [50] to derive the single phase uncertainties ϕ_i from the uncertainty of the phase advance $\phi_{i,j}$, based on the β-functions at the two locations s_i and s_j

$$\sigma^2_{\phi_i} = \sigma^2_{\phi_{i,j}}\left(1 + \frac{\beta_i}{\beta_j}\right)^{-1}. \tag{2.10}$$

Table 2.1.: t value correction for a confidence interval of 68.3 %.

Number of measurements	$\boldsymbol{t(n)}$
2	1.84
3	1.32
4	1.20
5	1.15
10	1.06

The correlation coefficient between two phase advances $\phi_{i,j}$ and $\phi_{i,k}$, with $j \neq k$, can be derived by transforming the covariance matrix of the single phase uncertainties

$$\boldsymbol{U} = \begin{pmatrix} \sigma^2_{\phi_i} & 0 & 0 \\ 0 & \sigma^2_{\phi_j} & 0 \\ 0 & 0 & \sigma^2_{\phi_k} \end{pmatrix}, \tag{2.11}$$

to a covariance matrix of the phase advances by using the transformation matrix

$$\boldsymbol{T}_1 = \begin{pmatrix} \frac{\partial \phi_{i,j}}{\partial \phi_i} & \frac{\partial \phi_{i,k}}{\partial \phi_i} \\ \frac{\partial \phi_{i,j}}{\partial \phi_j} & \frac{\partial \phi_{i,k}}{\partial \phi_j} \\ \frac{\partial \phi_{i,j}}{\partial \phi_k} & \frac{\partial \phi_{i,k}}{\partial \phi_k} \end{pmatrix}. \tag{2.12}$$

With the transformation $\boldsymbol{T}_1^T \boldsymbol{U} \boldsymbol{T}_1$ one gets the covariance matrix for the two phase advances $\phi_{i,j}$ and $\phi_{i,k}$ in the standard form

$$\boldsymbol{T}_1^T \boldsymbol{U} \boldsymbol{T}_1 = \begin{pmatrix} \sigma^2_{\phi_{i,j}} & \rho(\phi_{i,j}, \phi_{i,k}) \sigma_{\phi_{i,j}} \sigma_{\phi_{i,k}} \\ \rho(\phi_{i,j}, \phi_{i,k}) \sigma_{\phi_{i,j}} \sigma_{\phi_{i,k}} & \sigma^2_{\phi_{i,k}} \end{pmatrix}, \tag{2.13}$$

from which the correlation coefficient can be extracted as

$$\rho(\phi_{i,j}, \phi_{i,k}) = \frac{\partial \phi_{i,j}}{\partial \phi_i} \frac{\partial \phi_{i,k}}{\partial \phi_i} \frac{\sigma^2_{\phi_i}}{\sigma_{\phi_{i,j}} \sigma_{\phi_{i,k}}}. \tag{2.14}$$

Let the phase at the probed BPM be ϕ_1, all other phase advances can be calculated with respect to this BPM. The elements of the covariance matrix for the different phase advances $\phi_{1,2}$ to $\phi_{1,n}$ are defined by

$$\begin{aligned} \boldsymbol{C}_{i-1,j-1} = \rho(\phi_{1,i}, \phi_{1,j}) \sigma_{\phi_{1,i}} \sigma_{\phi_{1,j}}, \\ i \geq 2, j \geq 2, \end{aligned} \tag{2.15}$$

which is $\sigma^2_{\phi_{1,i}}$ when $i = j$ and $\pm\sigma^2_{\phi_1}$ elsewhere. Using the transformation matrix

$$\boldsymbol{T}_2 = \begin{pmatrix} \frac{\partial\beta_1}{\partial\phi_{1,2}} & \cdots & \frac{\partial\beta_m}{\partial\phi_{1,2}} \\ \vdots & \ddots & \vdots \\ \frac{\partial\beta_1}{\partial\phi_{1,n}} & \cdots & \frac{\partial\beta_m}{\partial\phi_{1,n}} \end{pmatrix}, \tag{2.16}$$

the covariance matrix for the phases can be transformed to a covariance matrix for the m β-functions ($\boldsymbol{V}_{stat}$) which are calculated from using different BPM combinations,

$$\boldsymbol{V}_{stat} = \boldsymbol{T}_2^T \boldsymbol{C} \boldsymbol{T}_2. \tag{2.17}$$

This covariance matrix is to be used in Eq. (2.8).
As a test of the correct implementation of the equations for the statistical errors in the optics analysis code, simulations of the optics measurement have been performed. TbT measurements were simulated for every BPM positions with enhanced noise and without SVD cleaning. This has been done to create 500 sets of BPM TbT data, which corresponds to 500 measurements.
Since in contrast to a real measurement, in this simulation the phase at each BPM is known in absolute values, it is possible to derive the uncertainty of the phase for each BPM position from its variation. As the uncertainties of the single phases and also of the phase advances are known, they were used directly in Eq. (2.14) to create the covariance matrix. The afore described error propagation was applied and the β-function derived according to Eq. (1.14), with its uncertainty according to Eq. (2.7). Systematic errors are neglected here, as they are not depending on the amount of measurements.
The distribution of the β-function in these 500 data sets has been fitted to a Gaussian distribution for each BPM. The value of the σ from the fit was then compared to calculated uncertainties of the β-function using Eq. (2.7), cf. Fig. 2.4. The calculated values of the uncertainty agree well to the expected value from the variations of the β-function, which is not the case for the old equations for the error calculation, where the error bars were too pessimistic. In this plot one can furthermore see, that most of the points are located at two levels. This is due to the fact, that the BPMs in the arcs, where most BPMs are, alternate between a β-function of 30 m and 170 m, and the phase can be measured with a higher relative precision at a BPM with a larger β-function, due to the larger oscillation amplitude.

2.1.1. Uncertainty of the calculated error bars

The study of the uncertainty of the error bar gives an important insight in the accuracy of the measurement method. Simulated TbT data with the same noise level

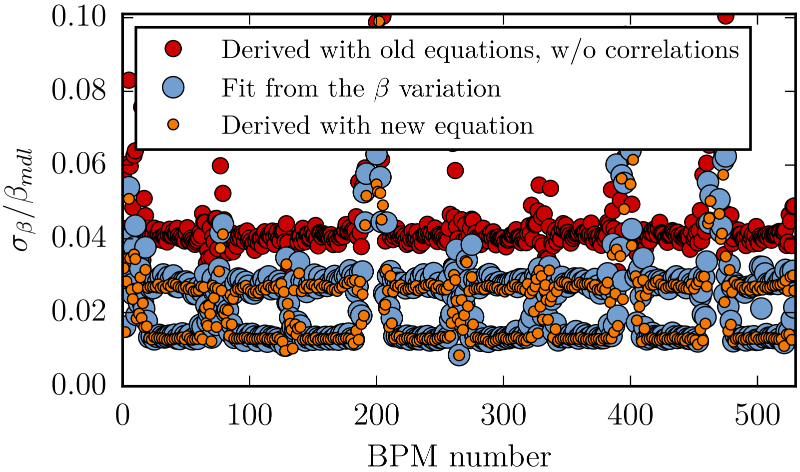

Figure 2.4.: Relative uncertainty of the β-function derived in the error propagation compared to a fit of the variation of calculated β-functions.

as in Section 2.1 were used for this analysis. Several measurement files are now used together for one analysis, which implies that the error of the phase advance is now to be calculated from Eq. (2.9), by using the standard deviation of the phase advances from the different measurements. This was done for the cases of using two to ten measurement files together, and repeated for the 500 measurement files. The deviations of the calculated error bar of the β-function to the uncertainty, which is calculated from the known phase uncertainty, is fitted with a Gaussian distribution. The σ of this fit is shown in Fig. 2.5 as a distribution for all BPMs. This plot shows that the uncertainty of the error bar reaches up to 60 %, if only three measurements are used. Significantly more precise is the error bar when five measurements are used, where its uncertainty varies from (20–35) %. This number further decreases when more measurements are used. For ten measurements the uncertainty is only at (10–22) %. The mean value of fitting the deviation of the error bar to the real uncertainty with a Gaussian distribution shows, if either the error bar is biased towards smaller or larger values, which is shown in Fig. 2.6. One can see in this plot, that for three measurements the distribution is not centered around zero, but at a positive value, which means that there is tendency to overestimate the error bar. Additionally, the width of the distribution is rather large when using less than five measurements. This also shows that the t value correction is useful, as without it the error bars would be biased to underestimate the real error.

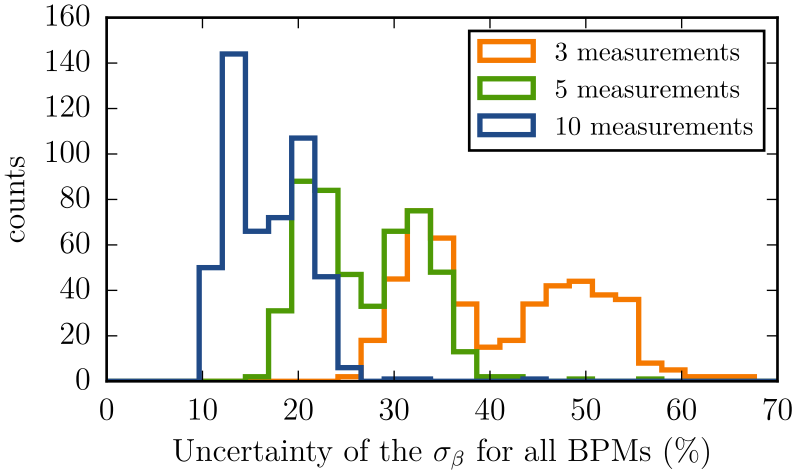

Figure 2.5.: The distribution shows for all BPMs the width of the deviation of the derived uncertainty of the β-function compared to the calculated error bar from the known phase uncertainty.

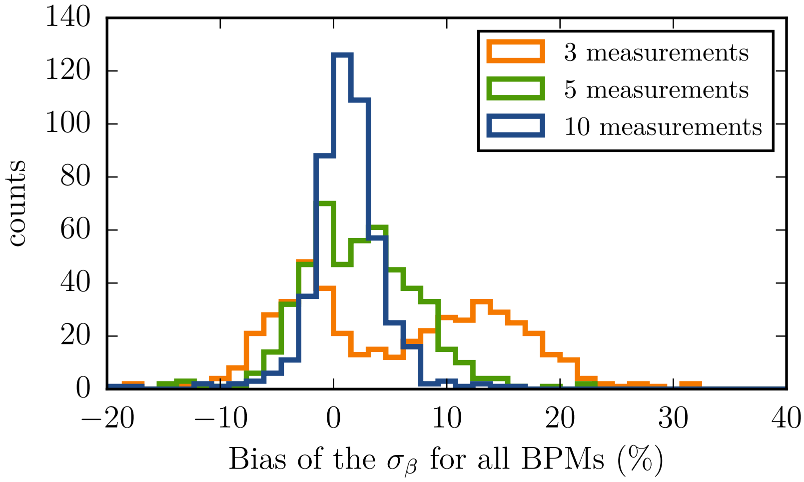

Figure 2.6.: The distribution shows for all BPMs the mean of the deviation of the derived uncertainty of the β-function compared to the calculated error bar from the known phase uncertainty.

2.2. Accuracy of the transfer matrix model

A precise knowledge of the model transfer matrix is essential for the computation of the β-function in Eq. (1.46). In this section improvements to the nominal optics model are studied, based on known systematic errors.

Dipole b_2 errors

Due to imperfections, every dipole magnet has a non-zero quadrupole field component (b_2), cf. Eq. (1.24). The 1232 main dipoles of the LHC have additionally a geometric b_2 component, due to the design with two apertures for the two beams (twin aperture), which is of opposite sign in both apertures and changes with the main field strength. The distribution of the measured b_2 component is shown in Fig. 2.7. The following

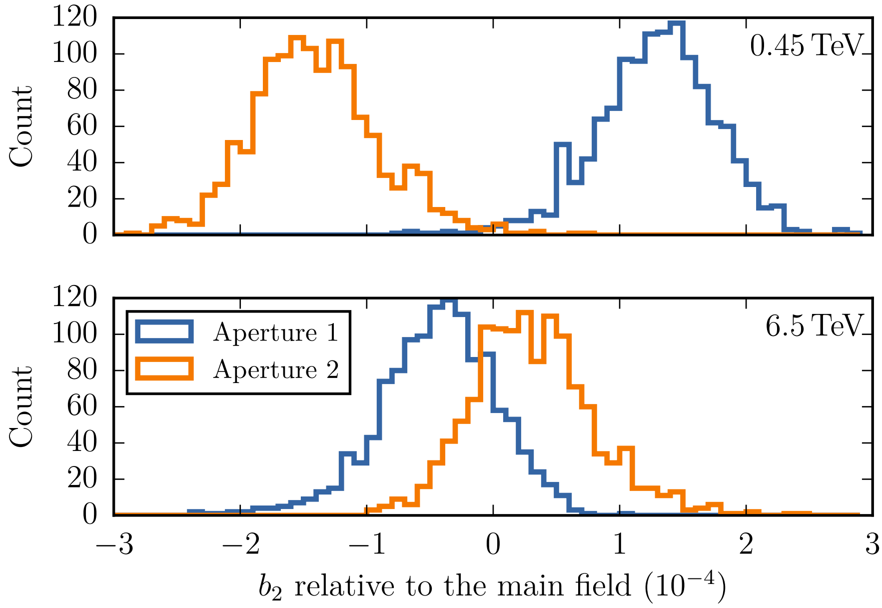

Figure 2.7.: Distribution of the b_2 component for the LHC main dipole magnets, separately for both apertures, at 450 GeV and 6.5 TeV.

equation allows to analytically estimate the deviation of the measured β-function up to the first order of quadrupole field errors Δk, and has been derived in [88].

$$\frac{\Delta\beta}{\beta} = \frac{h_{13} - h_{12}}{\cot\Delta\phi_{12} - \cot\Delta\phi_{13}}, \tag{2.18}$$

with

$$h_{ij} = \mp\frac{\sum_{i<w<j}\beta_w\Delta k_w \sin^2\Delta\phi_{wj}}{\sin^2\Delta\phi_{ij}}, \tag{2.19}$$

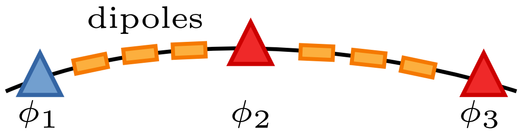

Figure 2.8.: The β-function is derived at the BPM with phase ϕ_1. The phase advances to two other BPMs are used, with $\phi_{12} = \phi_2 - \phi_1$ and $\phi_{13} = \phi_3 - \phi_1$.

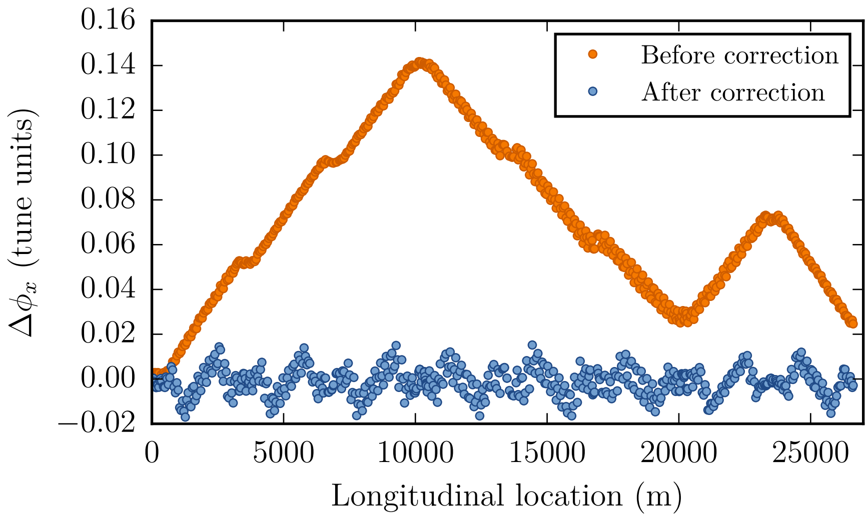

Figure 2.9.: Illustration of the betatron phase deviation due to the dipole b_2 components and after an arc-by-arc correction with MQT magnets. The slope of the phase deviation changes when the beam changes from the inner to the outer aperture after an interaction point.

gives the relative deviation of the measured β-function due to quadrupole field errors Δk_w, which are in between three BPMs with the phase advances ϕ_{12} and ϕ_{13}, as shown in Fig. 2.8. For an LHC arc cell, cf. Fig. 1.10, the phase advance between consecutive BPMs is $\pi/4$, i.e. $\phi_{12} = \pi/4$ and $\phi_{13} = \pi/2$. The first main dipole (MB) magnet in this cell has a horizontal β-function of 133 m in its center, and a phase advance of 0.023π from the first BPM. In this case Eq. (2.18) gives a relative error of the measured β-function of $5 \cdot 10^{-5}$, which by its own is negligible. However, in between two BPMs there are three MBs magnets, and this number increases if larger amounts of BPMs are used, e.g. for a range of eleven BPMs, 30 MB magnets are involved. The effect of the b_2 component will add up as the b_2 component for one aperture systematically perturb the optics in the same direction.

Moreover, the b_2 component of MB magnets cause a phase shift, which is corrected arc-by-arc using tune trim quadrupole (MQT) magnets, as shown in Fig. 2.9. A typical

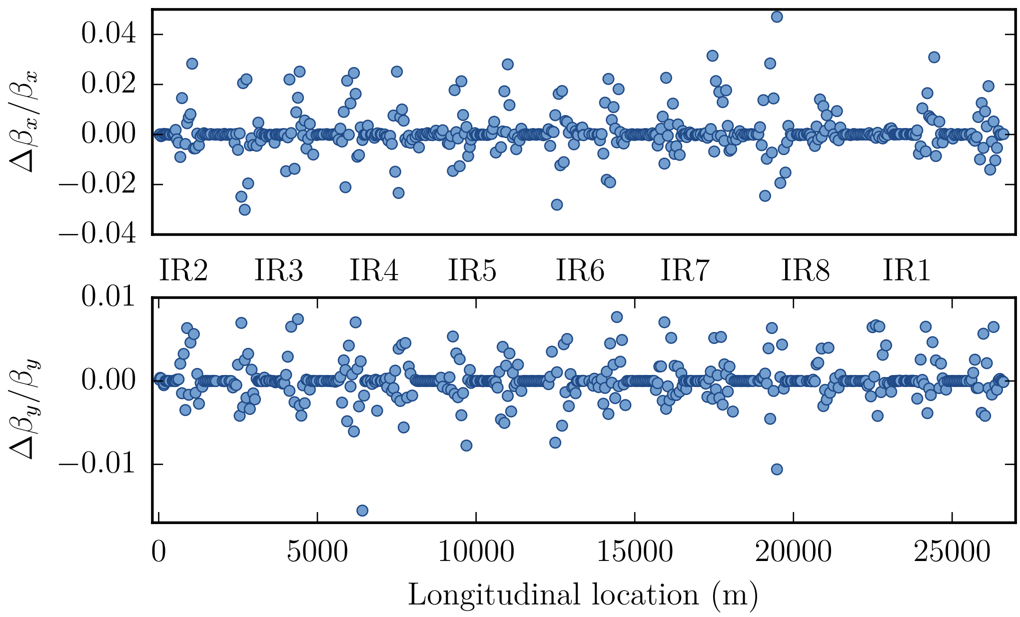

Figure 2.10.: Relative deviation of the computed β-function for a measurement of beam 1 at a β^* of 80 cm, between using either a model with the nominal setting of MQT magnets, or the real setting of the magnets during the measurement.

correction strength of an MQT magnet at 450 GeV, will cause a relative deviation of the measured β-function of 1.5 % according to Eq. (2.18). These error sources deteriorate the measurement of the β-function in a non-negligible way. Therefore, the measured values for the dipole b_2 component and the correction with MQT magnets are included in the optics model, which is used to derive the β-function.

MQT magnet settings

MQT magnets are not only used for the correction of the dipole b_2 errors as shown the previous paragraph, but also to set a specific tune value of the machine. For a specific measurement, the deviations of the measured β-functions between using the nominal setting of the MQT magnets or the real setting during that measurement are shown in Fig. 2.10. Deviations are only visible around the positions of MQT magnets, and the absolute values are below 3 % in the horizontal and 1 % in the vertical plane, with the exceptions of one 4.5 % deviation in the horizontal and one −1.5 % deviation in the vertical plane. It is therefore necessary to consider the real settings of these magnets as well. The optics analysis code has been improved to allow for an extraction of the MQT magnet setting for a specific time, so that these can be included in the optics model for deriving the β-functions.

2.3. Assessment of significant systematic errors

In this section, significant systematic errors which deteriorate the measurement of the β-function are evaluated and a covariance matrix for the systematic errors $\boldsymbol{V}_{syst}$ is derived, which is to be used in Eq. 2.8. The following uncertainties are considered in the estimate of the systematic error: (i) the uncertainty of the b_2 component of the dipole magnets, (ii) an individual uncertainty of the gradient for each quadrupole magnet family, (iii) a Gaussian distributed misalignment uncertainty of 1 mm along the longitudinal axis for quadrupole magnets and (iv) a Gaussian distributed misalignment uncertainty of 1 mm in the transverse plane for sextupole magnets.
Sextupole magnets perturb the linear optics if they are transversely displaced, as in this case they would have a non-zero b_2 component, cf. Eq. (1.24). The gradient uncertainties for the different quadrupole families have been derived from magnetic measurements [89, 90] and are shown in Table 2.2. The influence of deviations in the

Table 2.2.: Gradient errors of different quadrupole magnet families for the systematic error calculation.

Quadrupole family	**Error relative to the main field (10^{-4})**	
	450 GeV	**6.5 TeV**
MQ	14	18
MQM	13	12
MQY	11	8
MQX	3	4
MQW	33	15
MQT	72	75

optics model to the measurement of the β-function can be determined by introducing errors in the optics model following a Monte-Carlo approach. The β-function is then calculated using the phase advances from the perturbed model and the transfer matrix elements from the ideal model. The variation of the β-functions corresponds to the error for every given set of BPM combinations. This has been done for 10^3 cases where the errors have been varied following Gaussian distributions, truncated at three standard deviations. From this Monte-Carlo simulation one can derive the covariance matrix of the systematic errors $\boldsymbol{V}_{syst}$. In Table 2.3 the average systematic error at arc BPMs is shown for different BPM combinations. In this table several combinations of three BPMs have been omitted, since they show the same results due to the symmetry and regular distribution of BPMs in the arcs. The minimum systematic error is around 0.4 % when neighboring BPMs are used. It increases to

(0.9–15.0) % if one allows to skip one BPM, i.e. for a range of 7 BPM. A range of 9 BPMs is omitted in this table, as the systematic error would be very large, since the phase advance to the fourth BPM left or right of the probed BPM is around π. Although the systematic errors increase for larger ranges of BPMs, for a range of 11 BPMs some combinations of three BPMs can be found with uncertainties below 2 %.

Table 2.3.: Average systematic error of the measured horizontal (H) and vertical (V) β-function at arc BPMs for using different BPM combinations. The phase advance between consecutive BPMs is approximately $\pi/4$.

BPM combination	**Systematic error (%)**	
$\color{blue}\blacktriangle$: probed, $\color{red}\blacktriangle$: used, $\color{gray}\blacktriangle$: unused	**H**	**V**
$\color{red}\blacktriangle\color{blue}\blacktriangle\color{red}\blacktriangle$	0.5	0.4
$\color{red}\blacktriangle\color{red}\blacktriangle\color{blue}\blacktriangle\color{gray}\blacktriangle\color{gray}\blacktriangle$	0.5	0.4
$\color{red}\blacktriangle\color{gray}\blacktriangle\color{blue}\blacktriangle\color{red}\blacktriangle\color{gray}\blacktriangle$	1.2	0.9
$\color{red}\blacktriangle\color{gray}\blacktriangle\color{blue}\blacktriangle\color{gray}\blacktriangle\color{red}\blacktriangle$	7.5	15.4
$\color{red}\blacktriangle\color{red}\blacktriangle\color{gray}\blacktriangle\color{blue}\blacktriangle\color{gray}\blacktriangle\color{gray}\blacktriangle\color{gray}\blacktriangle$	1.9	1.3
$\color{red}\blacktriangle\color{gray}\blacktriangle\color{red}\blacktriangle\color{blue}\blacktriangle\color{gray}\blacktriangle\color{gray}\blacktriangle\color{gray}\blacktriangle$	1.2	0.9
$\color{red}\blacktriangle\color{gray}\blacktriangle\color{gray}\blacktriangle\color{blue}\blacktriangle\color{red}\blacktriangle\color{gray}\blacktriangle\color{gray}\blacktriangle$	8.3	15.0
$\color{red}\blacktriangle\color{gray}\blacktriangle\color{gray}\blacktriangle\color{blue}\blacktriangle\color{gray}\blacktriangle\color{red}\blacktriangle\color{gray}\blacktriangle$	2.2	2.1
$\color{red}\blacktriangle\color{gray}\blacktriangle\color{gray}\blacktriangle\color{blue}\blacktriangle\color{gray}\blacktriangle\color{gray}\blacktriangle\color{red}\blacktriangle$	1.7	1.4
$\color{red}\blacktriangle\color{red}\blacktriangle\color{gray}\blacktriangle\color{gray}\blacktriangle\color{gray}\blacktriangle\color{blue}\blacktriangle\color{gray}\blacktriangle\color{gray}\blacktriangle\color{gray}\blacktriangle\color{gray}\blacktriangle\color{gray}\blacktriangle$	77.3	286.4
$\color{red}\blacktriangle\color{gray}\blacktriangle\color{red}\blacktriangle\color{gray}\blacktriangle\color{gray}\blacktriangle\color{blue}\blacktriangle\color{gray}\blacktriangle\color{gray}\blacktriangle\color{gray}\blacktriangle\color{gray}\blacktriangle\color{gray}\blacktriangle$	1.4	1.3
$\color{red}\blacktriangle\color{gray}\blacktriangle\color{gray}\blacktriangle\color{red}\blacktriangle\color{gray}\blacktriangle\color{blue}\blacktriangle\color{gray}\blacktriangle\color{gray}\blacktriangle\color{gray}\blacktriangle\color{gray}\blacktriangle\color{gray}\blacktriangle$	2.1	2.1
$\color{red}\blacktriangle\color{gray}\blacktriangle\color{gray}\blacktriangle\color{gray}\blacktriangle\color{red}\blacktriangle\color{blue}\blacktriangle\color{gray}\blacktriangle\color{gray}\blacktriangle\color{gray}\blacktriangle\color{gray}\blacktriangle\color{gray}\blacktriangle$	6.3	16.5
$\color{red}\blacktriangle\color{gray}\blacktriangle\color{gray}\blacktriangle\color{gray}\blacktriangle\color{gray}\blacktriangle\color{blue}\blacktriangle\color{red}\blacktriangle\color{gray}\blacktriangle\color{gray}\blacktriangle\color{gray}\blacktriangle\color{gray}\blacktriangle$	1.1	1.1
$\color{red}\blacktriangle\color{gray}\blacktriangle\color{gray}\blacktriangle\color{gray}\blacktriangle\color{gray}\blacktriangle\color{blue}\blacktriangle\color{gray}\blacktriangle\color{red}\blacktriangle\color{gray}\blacktriangle\color{gray}\blacktriangle\color{gray}\blacktriangle$	3.2	2.0
$\color{red}\blacktriangle\color{gray}\blacktriangle\color{gray}\blacktriangle\color{gray}\blacktriangle\color{gray}\blacktriangle\color{blue}\blacktriangle\color{gray}\blacktriangle\color{gray}\blacktriangle\color{red}\blacktriangle\color{gray}\blacktriangle\color{gray}\blacktriangle$	5.1	10.8
$\color{red}\blacktriangle\color{gray}\blacktriangle\color{gray}\blacktriangle\color{gray}\blacktriangle\color{gray}\blacktriangle\color{blue}\blacktriangle\color{gray}\blacktriangle\color{gray}\blacktriangle\color{gray}\blacktriangle\color{red}\blacktriangle\color{gray}\blacktriangle$	7.9	295.5
$\color{red}\blacktriangle\color{gray}\blacktriangle\color{gray}\blacktriangle\color{gray}\blacktriangle\color{gray}\blacktriangle\color{blue}\blacktriangle\color{gray}\blacktriangle\color{gray}\blacktriangle\color{gray}\blacktriangle\color{gray}\blacktriangle\color{red}\blacktriangle$	1.9	1.5

2.4. Evaluation of the measurement precision and accuracy

The N-BPM method allows in general to use the measured TbT data of all available BPM. However, the farther away two BPMs are, the larger become systematic uncertainties of the transfer matrix elements, and the improvement of the measurement uncertainty will therefore become smaller. Furthermore, the computation of the covariance matrix is more time consuming for larger ranges of BPMs. The gain in precision and accuracy was studied with simulations for a range of up to 13 BPMs. Furthermore, instead of using all m BPM combinations, cf. Eq. (2.2), the simulations were done separately for different amount j of BPM combinations, with $0 < j \leq m$. The BPM combinations were sorted according to the expected error for the β-function based on their model phase advances. The BPM combinations which are used for the computation of the β-function are drawn from this sorted list starting with the combinations with the best phase advances.
Another simulation was performed with a sample size of 10^3, where random model uncertainties were applied according to the previous section, as well as a Gaussian noise of 200 µm to the BPM data for an oscillation amplitude of 1 mm in the arcs. From the fit of a Gaussian distribution to the variation of the derived β-functions at each BPM one can derive the following two parameters, which describe the uncertainty of the measurement. The mean value of the distribution of the β-functions is the accuracy, as it shows a bias towards larger or smaller results. The width of the distribution is the precision, which describes how large the spread is of the results, cf. Fig. 2.11. The average accuracy for all BPMs is always below 0.3 % which shows that the bias towards a wrong result is very low, cf. Fig 2.12. The improvement for the average precision is shown in Fig. 2.13. The gain in precision is very little when increasing the BPM range from 11 to 13. The amount of BPM combinations increase the precision noticeably up to using six BPMs and seem to saturate after that. For

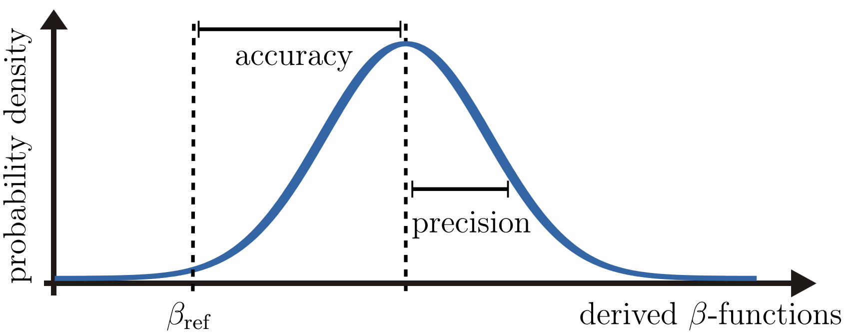

Figure 2.11.: Illustration of the precision and accuracy.

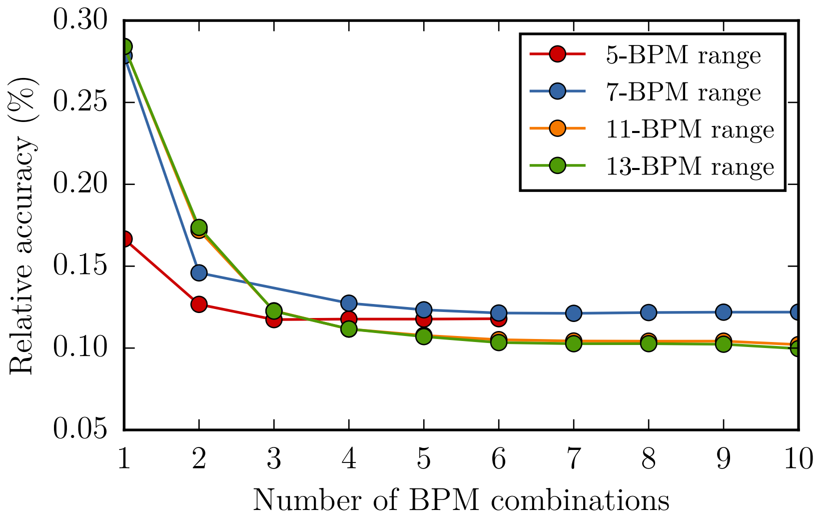

Figure 2.12.: Accuracy of the derived β-functions from simulations for different ranges of BPMs and different amount of BPM combinations. The oscillation amplitude was 1 mm in the arcs and a Gaussian noise of 200 µm was applied.

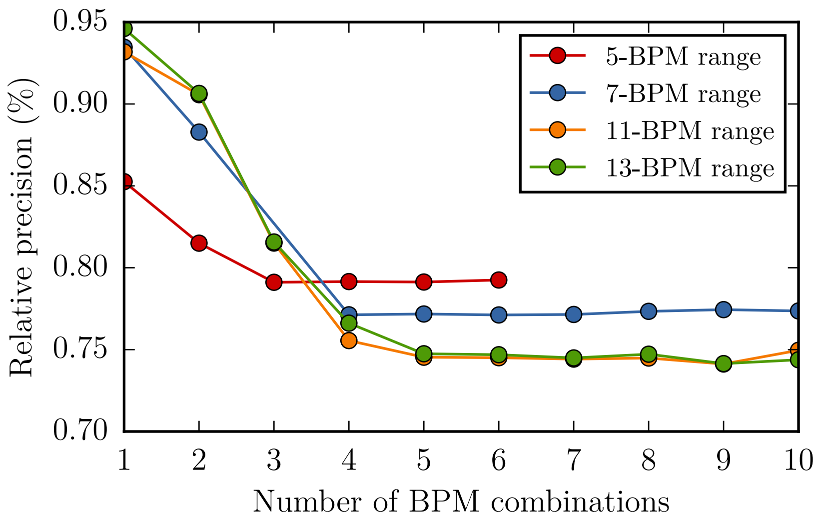

Figure 2.13.: Precision of the derived β-functions from simulations for different ranges of BPMs and different amount of BPM combinations. The oscillation amplitude was 1 mm in the arcs and a Gaussian noise of 200 µm was applied.

calculations at the LHC in the following, a range of 11 BPMs will be used, which is a good compromise between computational time efficiency and precision.

2.5. Verification with other optics measurement techniques

At the LHC, optics measurements can be performed with k-modulation, cf. Section 1.2.2, for individually powered quadrupoles. This is usually done for the triplet magnet to derive the β^*, and in IR4 where beam diagnostics elements are located. A comparison to TbT measurements is presented for measurements which have been taken in 2015.
Furthermore, a collaboration allowed to perform TbT optics measurements at the ALBA[1] accelerator. ALBA is a 3$^{\text{rd}}$ generation synchrotron light source with an operation energy of 3 GeV, which is operated as a user facility since 2012 [91, 92]. This allows to test the N-BPM method at a different machine and to compare the results with LOCO, cf. Section 1.2.3, which is the standard method for optics measurements and corrections at ALBA [69].

2.5.1. K-modulation

Several k-modulation measurements were performed during the LHC commissioning in 2015 [93], which allow for a comparison to TbT measurements. The details of the measurements which are compared here are shown in Table 2.4. For injection optics at 450 GeV, TbT measurements were also performed at the beginning of the commissioning at 10$^{\text{th}}$ April 2016, however these measurements suffered from issues with the BPMs, cf. Section 3.2.1, and a comparison to k-modulation measurements showed a significant discrepancy for two out of 24 data points [94]. A comparison of the results from both measurement methods is shown in Figs. 2.14 and 2.15 for twelve magnets in IR4. Figure 2.16 shows the results for IP1 for a β^* of 20 m at 6.5 TeV, for which k-modulation data only exist for beam 1. In the comparison of the β-function at a magnet, the results from TbT measurement needed to be propagated from BPM

Table 2.4.: K-modulation and TbT measurement details.

Measurement date		**Location**	**Energy**
k-modulation	**TbT**		
5$^{\text{th}}$ May 2016	28$^{\text{th}}$ August 2016	IR4	450 GeV
27$^{\text{th}}$ April 2016	9$^{\text{th}}$ May 2016	IP1	6.5 TeV

[1]from spanish alba, ‘sunrise’

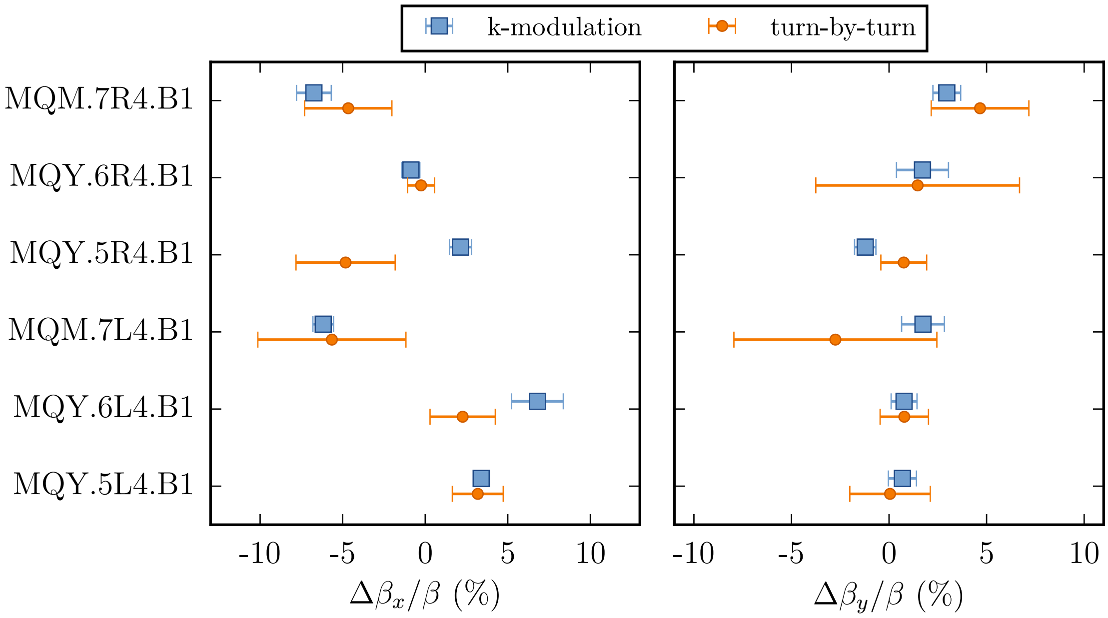

Figure 2.14.: Comparison of the measured β-functions using k-modulation and turn-by-turn measurements for magnets in IR4 for beam 1 at 450 GeV.

positions to the magnet, while k-modulation measurements directly give the average β-function at the magnet. This increases the uncertainty of TbT measurements if the propagation includes quadrupole magnets for which a gradient uncertainty is assumed.

To assess the agreement of both methods the χ^2 value can be computed as explained in Appendix A.1. For the hypothesis H_0, that both measurements agree, the χ^2 can be computed for the deviation of both measurements

$$y_i = \beta_{i,\mathrm{k-mod}} - \beta_{i,\mathrm{TbT}}, \tag{2.20}$$

with the uncertainty

$$\sigma_i = \sqrt{\sigma^2_{i,\mathrm{k-mod}} + \sigma^2_{i,\mathrm{TbT}}}. \tag{2.21}$$

The correlation term is omitted in the error propagation as both measurement methods are independent. The expected value, given H_0, is $y_{t,i} = 0$. Computing

$$\chi^2/\nu = \frac{1}{n}\sum_{i=1}^{n} \frac{\left(\beta_{i,\mathrm{k-mod}} - \beta_{i,\mathrm{TbT}}\right)^2}{\sigma^2_{i,\mathrm{k-mod}} + \sigma^2_{i,\mathrm{TbT}}}, \tag{2.22}$$

for the measurements at IR4 gives $\chi^2/\nu = 1.13$. The probability, given H_0, to get this χ^2 value or a larger one is $P(\chi^2, \nu) = 30\,\%$. The observed results are therefore very likely if both measurements agree.

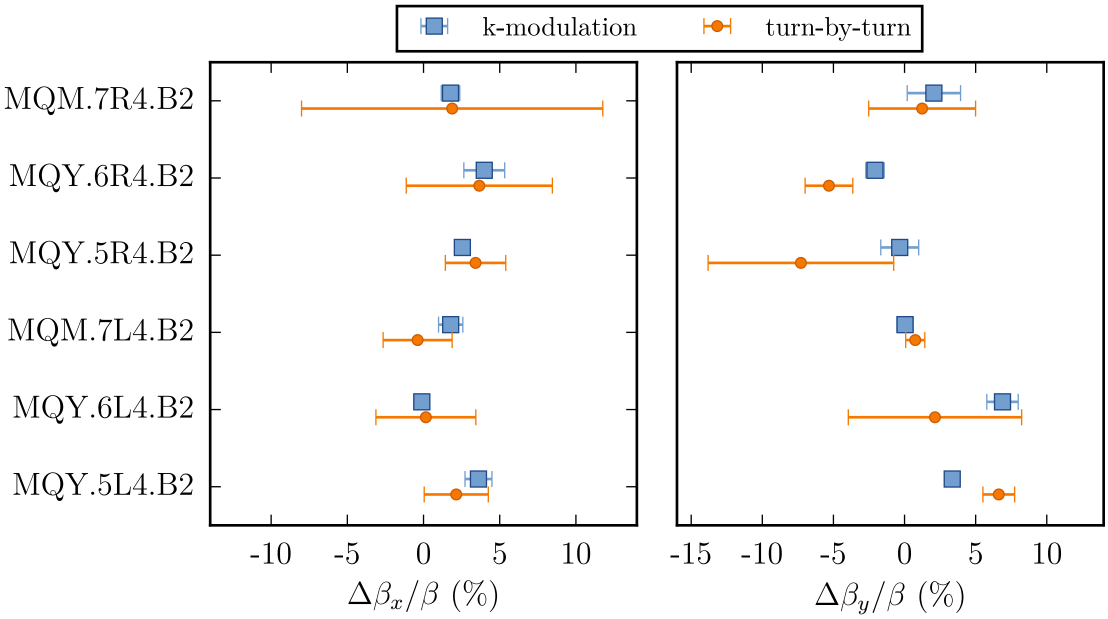

Figure 2.15.: Comparison of the measured β-functions using k-modulation and turn-by-turn measurements for magnets in IR4 for beam 2 at 450 GeV.

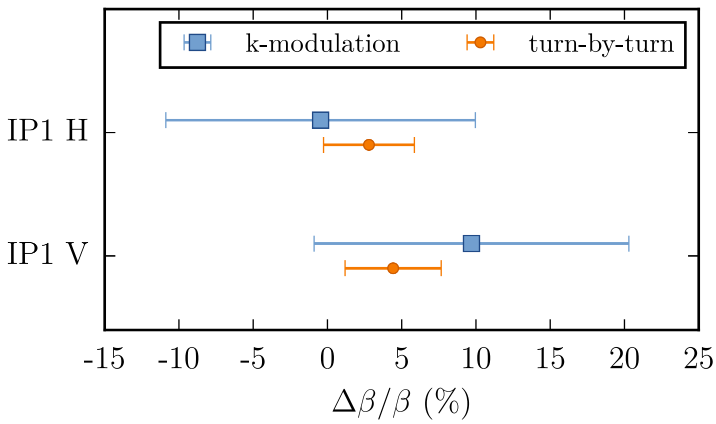

Figure 2.16.: Comparison of the measured β-functions using k-modulation and turn-by-turn measurements in IP1 for beam 1 at 6.5 TeV.

The same conclusion can be made for the measurement in IP1, where all data points agree within their error bars. In this case the uncertainty of the k-modulation measurement is larger due to a larger noise in the tune signal [95].

2.5.2. Optics measurements at the ALBA light source

TbT measurements can provide faster optics measurements than LOCO and are of great interest also for other light sources [70, 72, 96, 97]. Recently, efforts have been put in developing optics measurements based on BPM TbT data at ALBA. However, first measurement attempts of the β-function using the phase information of TbT data were futile. The precision was notably worse compared to the β-functions that were inferred from the amplitude information which showed a discrepancy of (4–10) % to LOCO measurements [98]. Improvements of the BPM electronics, their timing setup and synchronization were a prerequisite for an advancement in the calculation of the β-function from the TbT amplitude information [73]. Also at SOLEIL[1] significant discrepancies were observed when comparing the β-beating from TbT measurements to LOCO and an optics correction study at SLS[2] found an inferior performance of turn-by-turn measurements compared to LOCO. Studies in ESRF[3] [58, 88] show that the model which arises from a fit to the phase advances from TbT data is comparable to their standard orbit response matrix (ORM) based model. The phase advances of consecutive BPMs are shown in Fig. 2.17 for the nominal ALBA lattice. Especially in the vertical plane, there are many consecutive BPMs with a small phase advance, and considering BPM combinations within a larger range of BPMs, as it is the case in the N-BPM method, would allow for better phase advances for the measurement.

In the following sections, systematic and random errors are evaluated, which is a prerequisite for using the N-BPM method. An estimate of the precision and accuracy of the measured β-functions is given based on tracking simulations. The precision of the LOCO method at ALBA has been studied in simulations and is expected to be 0.89 % in the horizontal and 1.06 % in the vertical plane [99].

Systematic errors of the *N*-BPM method

For the N-BPM method it is crucial to consider the effect of model uncertainties and their correlations for the β-function measurement, in order to derive the covariance matrix for the systematic errors V_{syst}, which is used in Eq. (2.6) to derive the weights

[1] SOLEIL is a 2.75 GeV electron synchrotron, located near Paris, France

[2] Swiss Light Source (SLS) is a 2.4 GeV electron synchrotron at the Paul Scherrer Institute (PSI) in Villigen, Switzerland

[3] European Synchrotron Radiation Facility (ESRF) is a 6 GeV electron synchrotron in Grenoble, France

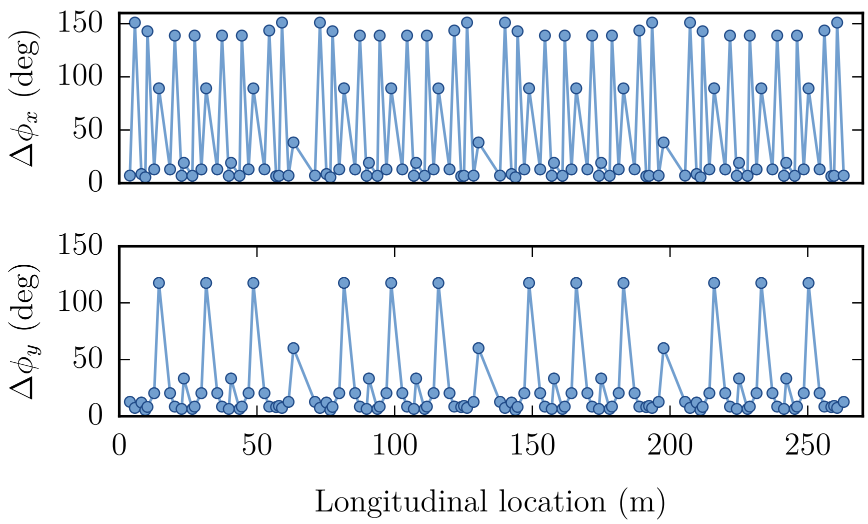

Figure 2.17.: Phase advances of consecutive BPMs in the nominal model. Many phase advances close to 0° impair the calculation of β-functions when using only neighboring BPMs.

for the computation of the β-function. The calculation of systematic errors is based on the uncertainties of magnetic measurements and alignment uncertainties, which can be found in Table 2.5. The Monte-Carlo simulation was performed for 10^3 iterations and the error sources were varied randomly following a Gaussian distribution. One can perform the Monte-Carlo simulations additionally separately for each contribution, to study how much each error source is contributing to the total systematic error, cf. Fig 2.18. The dominant contribution comes from quadrupolar gradient errors and transverse misalignment of sextupole magnets. In contrast to the vertical plane, in the horizontal plane the dipole b_2 errors have a negligible effect. This is because β_y is much larger at the dipole magnets than β_x.
The systematic errors can furthermore be assessed separately for different BPM combinations. In Table 2.6 the average systematic error of the measured β-function is shown for different BPM combinations. The lowest error is in both planes achieved for neighboring BPMs, if the BPM in the middle is probed. For other BPM combinations the systematic errors are increasing more quickly in the horizontal than in the vertical plane.

Precision and accuracy of the *N*-BPM method

The uncertainty of the β-function measurement depends additionally on the statistical error of the phase measurement, which is expressed by the covariance matrix V_{stat}.

Table 2.5.: Uncertainties which are considered in the computation of systematic errors. Quadrupolar errors are specified relative to their main field (quadrupoles), respectively relative to their quadrupole component (dipoles).

Quadrupolar errors	**Uncertainty**
Dipole b_2 component	0.1 %
Quadrupole gradient	0.1 %
Misalignments	**Uncertainty**
Quadrupole, longitudinal	300 µm
BPM, longitudinal	300 µm
Sextupole, transverse	150 µm

A simulation of the TbT measurement was done to assess the overall uncertainty of the N-BPM method. 500 lattices were created by randomly adding errors to the nominal model according to Table 2.5. For each lattice, 5 measurements of BPM TbT data with 10^3 turns each were simulated. In simulations, the noise which is applied to the TbT data, e.g. a Gaussian noise, would be cleaned too efficiently with the SVD technique which is used for noise cleaning in real measurements [49, 100]. Instead of applying an empirical noise value to the data, the BPM noise and the beam excitation amplitude were adjusted to reproduce the standard deviation of the measured phase advance, as it is observed in a typical measurement. For the measurements which are analyzed here, the average uncertainty of the measured phase advances in units of 2π are $8.2 \cdot 10^{-3}$ for the horizontal and $7.8 \cdot 10^{-3}$ for the vertical plane. To achieve similar uncertainties in the simulation, a Gaussian noise of 14 µm / 13 µm (horizontal / vertical) was applied to the TbT data, while the beam excitation amplitude was set to 1 mm (peak to peak) at a β-function of 12 m. No additional cleaning with SVD was performed. This ensures that the calculation of the β-function in the simulation is using phase advances with similar random errors as they are in measurements. It should be noted that the real TbT data may likely have larger noise before cleaning than the (13–14) µm, which were used to reproduce the observed phase uncertainty after cleaning using SVD.

The β-functions were derived using the N-BPM method for different ranges of BPM. Furthermore, instead of using all possible m combinations of three BPM, cf. Eq. (2.2), j combinations were used with $0 < j \leq m$. For each BPM, the deviation of the measured β-function to the β-function of the perturbed lattice was fitted with a Gaussian distribution. The mean value of this distribution is the accuracy of the measurement, as it indicates a bias towards larger or smaller values. The width of the distribution is

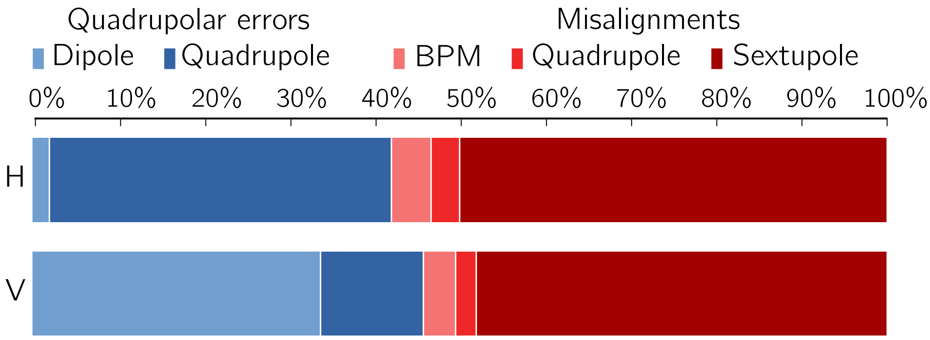

Figure 2.18.: Contribution of the uncertainties from Table 2.5 to the total variance of the derived β-function. The average value over all BPMs is shown for the case of probing the middle BPM of neighboring BPMs, as it is the combination which has the smallest systematic error. The top bar is for the horizontal plane (H) and the bottom one for the vertical plane (V). Quadrupolar errors are shown in blue and misalignment uncertainties in red.

Table 2.6.: Systematic error of the measured β-function for using different BPM combinations. The five best combinations are shown for each plane.

BPM combination ◮: probed, ▲: used, △: unused	**Average systematic error (%)**
horizontal plane	
△ △ ▲ ◮ ▲ △ △	0.18
△ ▲ ▲ ◮ △ △ △	0.24
▲ ▲ △ ◮ △ △ △	0.77
△ ▲ △ ◮ ▲ △ △	0.87
▲ △ ▲ ◮ △ △ △	0.88
vertical plane	
△ △ ▲ ◮ ▲ △ △	0.12
△ ▲ ▲ ◮ △ △ △	0.18
△ ▲ △ ◮ ▲ △ △	0.22
▲ △ ▲ ◮ △ △ △	0.26
▲ △ △ ◮ ▲ △ △	0.42

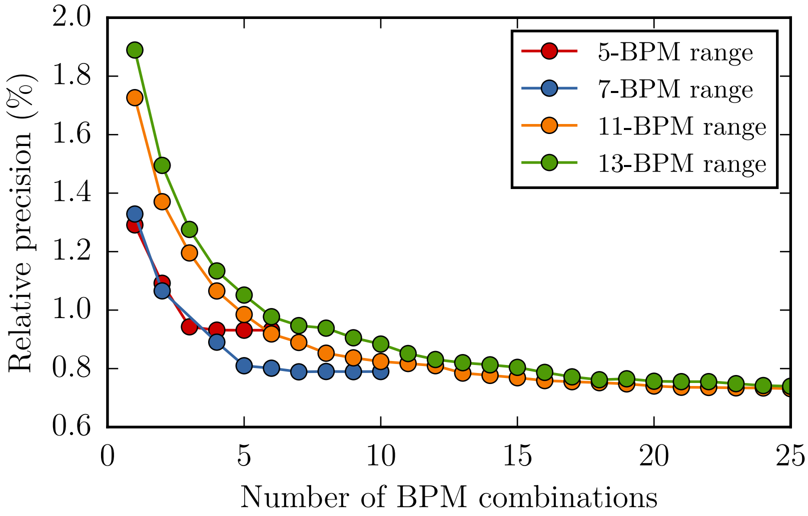

Figure 2.19.: Precision of the derived horizontal β-functions from simulations for different ranges of BPMs and different amount of BPM combinations.

the precision and describes how much the measurement spreads. Figures 2.19 and 2.20 show exemplary for the horizontal plane the evolution of the average precision and accuracy for all BPM for different ranges of BPM (N) and different number of BPM combinations (j) that were analyzed together. One can see how a larger number of BPM combinations will increase the precision and accuracy of the measurement until they saturate, as the information from further BPM combinations is negligible. The different BPM ranges start at a different value for the precision and accuracy, as the order of the BPM is not the same in every case. However, if enough BPM are used, a larger range of BPM will result in a better precision and accuracy as more information is used to derive the β-functions. Table 2.7 shows the precision and accuracy that can be achieved for using different BPM ranges. The precision of the vertical β-function saturates already for a 7-BPM range, whereas in the horizontal plane benefits are still visible up to a range of 13 BPMs.

Measurements

The ALBA synchrotron is equipped with 120 BPMs and TbT data was acquired using the moving average filter acquisition mode (MAF) [73]. The value of the β-function at the BPM positions vary approximately between 4 m and 13 m. For the excitation of the betatron oscillation, a pinger magnet was used. The peak-to-peak value of the amplitude for the betatron oscillation was 1 mm in the horizontal plane and 1.4 mm in the vertical plane, for BPMs with a β-function of 12.7 m (both planes).

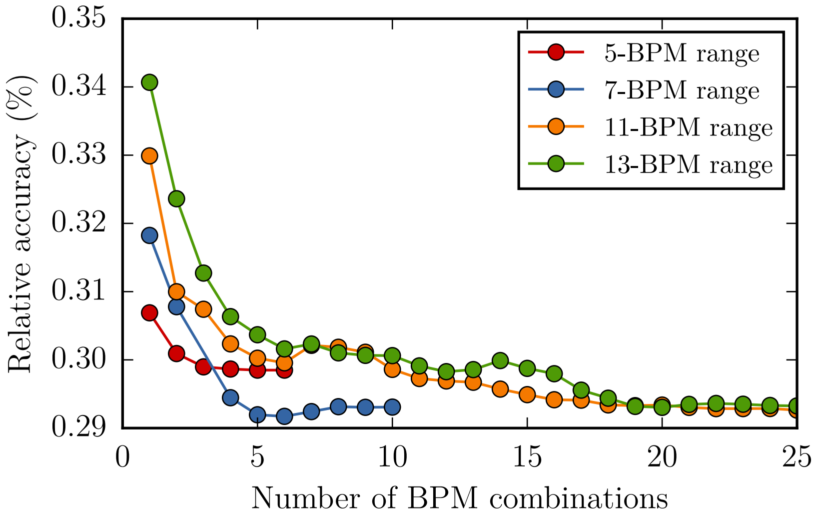

Figure 2.20.: Accuracy of the derived horizontal β-functions from simulations for different ranges of BPMs and different amount of BPM combinations.

Table 2.7.: Achievable precision and accuracy of the measured horizontal (H) and vertical (V) β-functions for using different BPM ranges.

BPM range	**Precision (%)**		**Accuracy (%)**	
	H	**V**	**H**	**V**
5	0.93	0.61	0.30	0.07
7	0.79	0.58	0.29	0.07
11	0.74	0.58	0.29	0.08
13	0.72	0.58	0.29	0.08

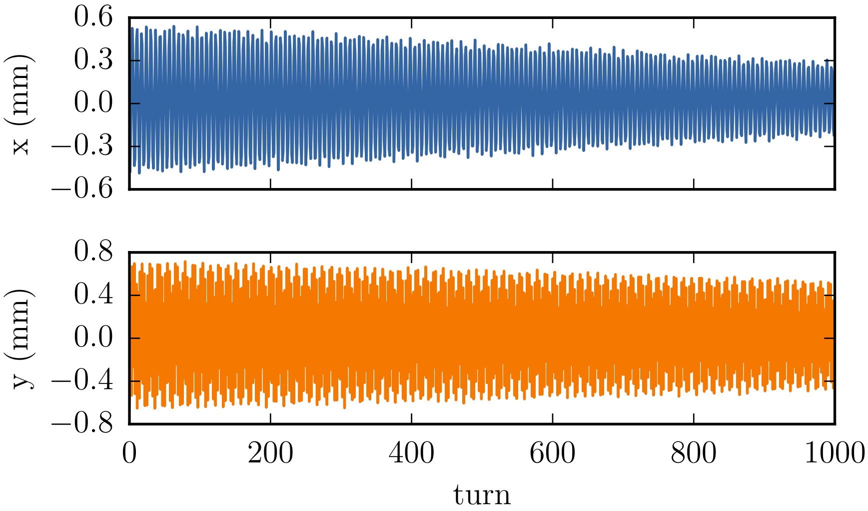

Figure 2.21.: Turn-by-turn oscillations at BPMs where $\beta = 12.7\,\mathrm{m}$.

40 measurements were performed, from which only 31 were used in the analysis, since some cases needed to be excluded due to BPM synchronization problems. The analysis was limited to 1024 turns, where the oscillation amplitude decreased by a factor of 2 in the horizontal plane, cf. Fig. 2.21. In contrast to using an ac dipole, like at the LHC, the pinger magnet performs a single beam excitation. This causes the TbT oscillation amplitude to damp over time due to the tune spread of the beam, and is referred to as decoherence [101]. The analysis was performed separately for using five different start turns, and averaging the results, to avoid distortions due to the decoherence. The rms deviation of the β-function among the five cases was 0.36 % in the horizontal and 0.19 % in the vertical plane. A correction formula, which can also be used to mitigate the decoherence effects is presented in [102]. A cleaning of the TbT data was performed using the SVD technique and keeping only the 12 strongest modes. Non-linear errors in the BPM calibration have been studied in [103], and are for oscillation amplitudes of 0.5 mm expected to be 2 µm. Non-linear effects due to sextupoles are assumed to be negligible as well for these oscillation amplitudes, as they were included in the tracking simulations where an accuracy of below 0.3 % of the measured β-function was achieved, as shown in Fig. 2.12. These assumptions are supported by analyzing the frequency spectrum in Fig. 2.22, where no cubic distortions are visible, as it was for example the case in [72].
Figure 2.23 shows the β-beating as computed from the phase of the betatron oscillation with the N-BPM method in comparison with the results obtained with LOCO. The error bars for the N-BPM method cover systematic and statistical uncertainties, whereas the error bars for LOCO account only for the reproducibility of the results.

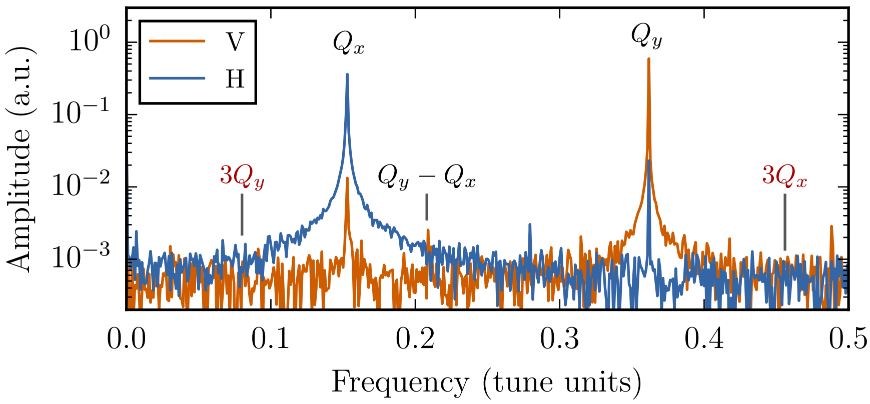

Figure 2.22.: Frequency spectrum of the horizontal (H) and vertical (V) turn-by-turn oscillations. The two peaks correspond to the tunes $Q_x = 18.15$ and $Q_y = 8.36$. No additional lines which correspond to cubic distortions at $3Q_x$ and $3Q_y$ are visible.

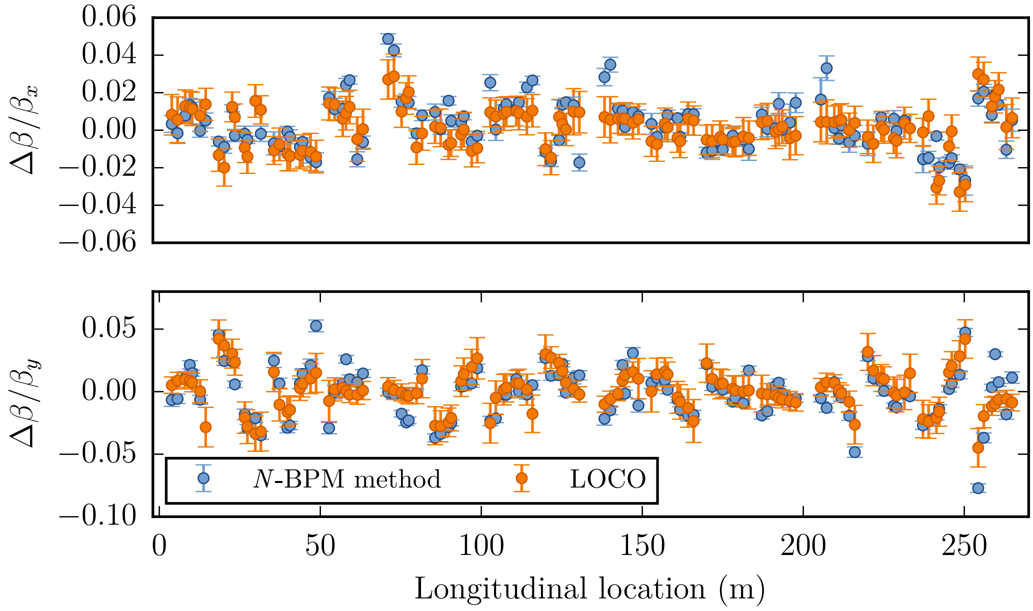

Figure 2.23.: Comparison of the β-beating as derived from BPM turn-by-turn data using the phase of the betatron oscillation (N-BPM method with an 11-BPM range) to the β-beating from LOCO.

There is a good agreement for many data points between both methods, however in general the deviations from LOCO to the nominal model are smaller, as shown in Table 2.8. Another method which can be used to obtain the β-function uses the amplitude information of the betatron oscillation, cf. Section 1.2.1. A prerequisite for this method is the knowledge of the kick action, as well as the gain of the BPMs. Instead of assessing these values, a normalized β-function was computed [73]. The β-beating from the amplitude method is compared to the N-BPM method in Fig. 2.24. The rms β-beating to the nominal model is for each method shown in Table 2.8.

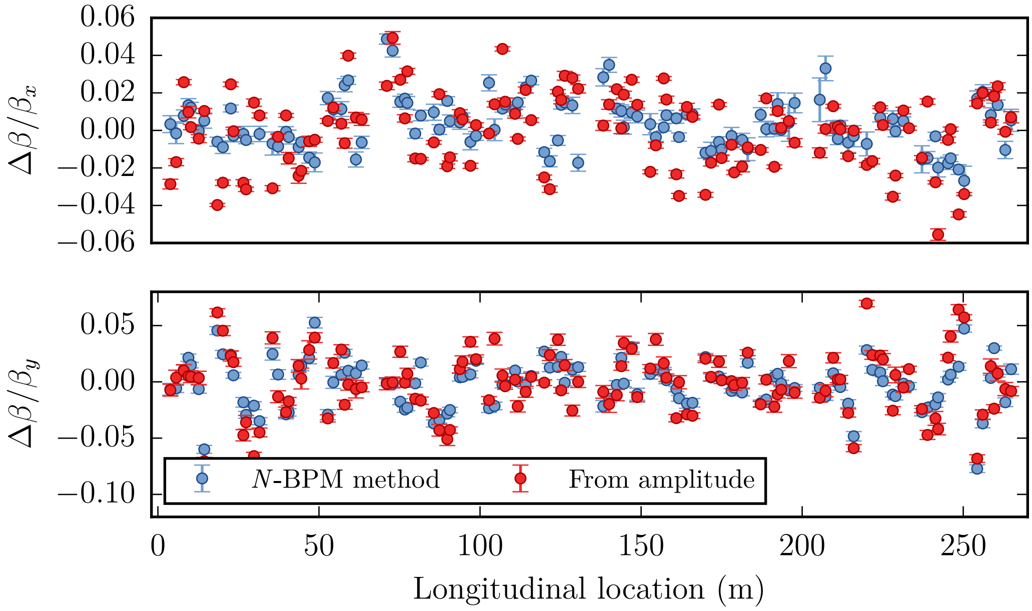

Figure 2.24.: Comparison of the β-beating as derived from BPM turn-by-turn data using either the amplitude information or phase of the betatron oscillation (N-BPM method).

Furthermore, in the second part of Table 2.8, the results which are obtained by the different methods are compared pairwise, by computing the rms deviation of the β-function between two methods.
The amplitude method shows the largest deviation from the nominal model. Using the normalized β-function on the one hand does not suffer from uncertainties of the computed kick action or BPM gains, but on the other hand introduces further systematic errors, as shown in Section 1.2.1.
Since the N-BPM method uses model transfer matrix elements, it was also tested to run the analysis not with the ideal model, but the model that has been fitted with LOCO. The idea is that if the LOCO model is closer to the real machine, then using

Table 2.8.: The first part shows the rms deviation of the β-function to the nominal model as computed from the different methods. The second and third part compares the deviation of the β-functions which are obtained by two different methods. In the third part for the N-BPM method the LOCO fitted model was used in the analysis instead of the ideal model.

	rms $\boldsymbol{\beta}$-beating (%)	
	horizontal	**vertical**
Method vs. nominal model		
N-BPM (phase)	1.4	2.0
From amplitude	2.0	2.7
LOCO	1.1	1.6
Method 1 vs. Method 2		
N-BPM (phase) vs. LOCO	1.0	1.3
N-BPM (phase) vs. amplitude	1.7	1.9
From amplitude vs. LOCO	1.4	1.7
$\boldsymbol{N}$-BPM using LOCO model		
N-BPM (phase) vs. LOCO	0.8	1.1

the LOCO model for the N-BPM method should also provide a result that is closer to the LOCO result. There is an improvement of the rms β-beating from the N-BPM method to LOCO of 20 % in both planes. These results are in excellent agreement considering the estimated uncertainties of the N-BPM method of in this case 1.01 % horizontally and 0.66 % vertically for a linear addition of the systematic and random uncertainties, in comparison with the LOCO uncertainties of 0.89 % in the horizontal and 1.06 % in the vertical plane [99].

3. LHC optics measurements

3.1. Re-analysis of run I measurements

Optics measurements from the first run of the LHC have been re-analyzed using the N-BPM method. In contrast to the analysis in 2012, the dipole b_2 errors are considered in the optics model, together with a new calibration of MQY magnets, which has been tested in a machine development (MD) session [104]. The SVD technique, cf. Section 1.2.1, was used to reduce the noise in the measured BPM TbT data [49, 100]. Only the 12 strongest singular modes were kept, since simulations showed only marginal improvements for smaller cuts. Figure 3.1 shows the resulting β-beating for the $\beta^* = 60\,\mathrm{cm}$ optics for beam 1, comparing the 2012 analysis with the results from the N-BPM method. The corresponding plot for beam 2 is shown in Fig. B.3 in Appendix B.2. The error bar for many BPM positions has significantly improved, in particular in the IRs. The IRs can be easily depicted in the 2012 analysis due to the large error bars in these regions, which is not the case in the N-BPM method. The root mean square (rms) and peak β-beating are shown in Table 3.1. Compared to the 2012 analysis the rms β-beating is similar [64], as well as the peak β-beating with a maximum value of $(9 \pm 1)\,\%$. From this measurement, the β^* values at the interaction points have been derived, cf. Table 3.2. In 2012 no β^* values have been published due to their large uncertainties.
Figure 3.2 shows the average uncertainty of the measured β-functions for different measurements from 2012 in comparison to a re-analysis with the N-BPM method. An improvement of at least a factor three of the average error bar is observed. The larger uncertainties in both methods for the ATS optics, which is a novel optics concept foreseen for the HL-LHC, is discussed in Section 4.1.

Table 3.1.: rms and peak β-beating after local and global corrections at $\beta^* = 60\,\mathrm{cm}$.

		Beam 1		**Beam 2**	
		x	**y**	**x**	**y**
$\frac{\Delta\beta}{\beta}$ (%)	peak	9 ± 1	9 ± 1	7.0 ± 0.6	6.7 ± 1.7
	rms	2.6	2.3	2.4	2.2

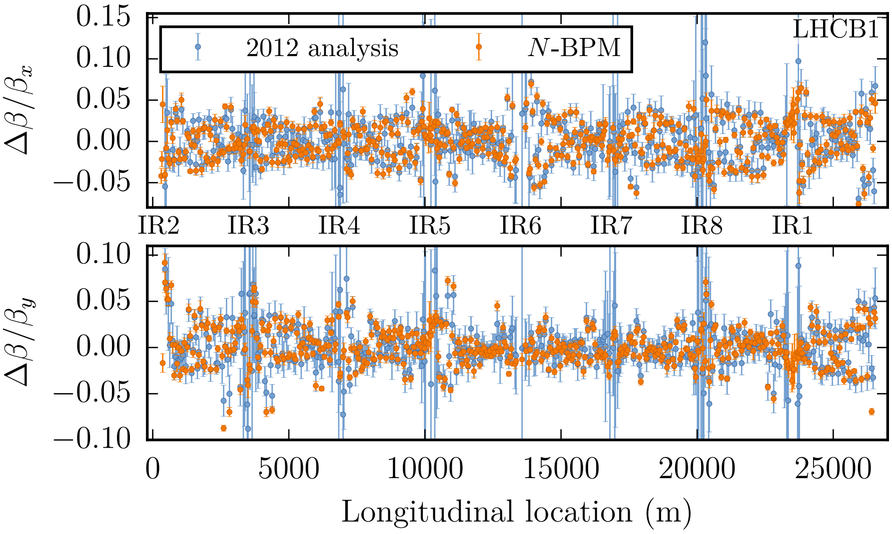

Figure 3.1.: β-beating for Beam 1 after local and global corrections at $\beta^* = 60\,\text{cm}$.

Table 3.2.: Measured β^* values for squeezed optics at $\beta^* = 60\,\text{cm}$ after local and global corrections.

Beam 1	β_x^* **(m)**	β_y^* **(m)**
IP1	0.589 ± 0.019	0.61 ± 0.03
IP2	2.85 ± 0.19	2.86 ± 0.06
IP5	0.595 ± 0.010	0.595 ± 0.011
IP8	3.03 ± 0.08	3.03 ± 0.11
Beam 2	β_x^* **(m)**	β_y^* **(m)**
IP1	0.592 ± 0.015	0.61 ± 0.02
IP2	3.0 ± 0.2	3.02 ± 0.08
IP5	0.59 ± 0.03	0.594 ± 0.013
IP8	3.06 ± 0.09	2.92 ± 0.15

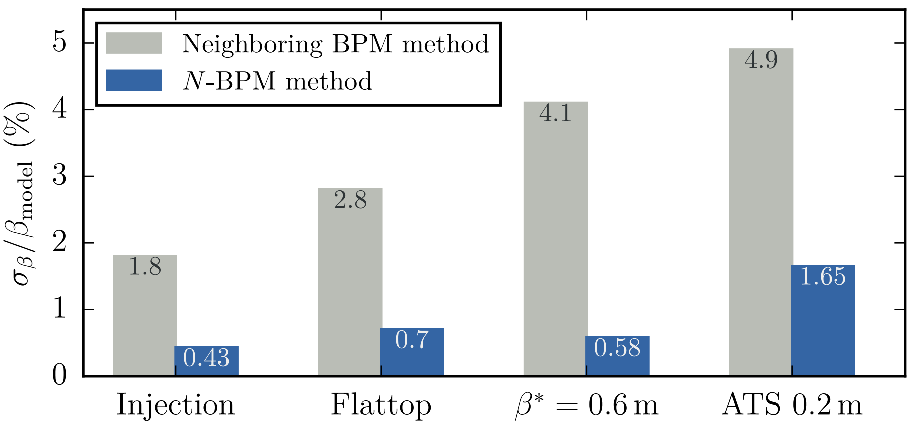

Figure 3.2.: Average uncertainty of the measured β-functions for different measurements from 2012.

3.2. Commissioning at 6.5 TeV

In this section the procedure and the results of the LHC optics commissioning for run II at an unprecedented energy of 6.5 TeV are presented. The higher energy poses challenges for the optics commissioning, as the larger damage potential of the machine limits the maximum oscillation amplitude and beam charge during optics measurements. The focus is on the application of the N-BPM method from chapter 2. This includes directly the measurement of the β-function, and based on this the calculation of optics corrections which benefits additionally from improvements to the SbS technique [84]. Furthermore, during the first long shutdown (LS1), hardware and software upgrades were performed which allow for a longer acquisition of turn-by-turn data with the ac dipole [105]. The benefit of this is discussed in section 3.4. During the optics commissioning and during MD sessions further measurements were performed to assess other aspects of the optics quality and to better understand the non-linear optics model [57, 60, 106–110]. This includes for example the measurement and correction of coupling between the horizontal and vertical plane, and the influence of non-linear errors which can be assessed for example in the measurement of detuning with amplitude or chromaticity.

The N-BPM method was used for the first time online for measurements in the control center during the LHC optics commissioning in 2015. Its results were furthermore directly used for the calculation and verification of optics corrections. The optics commissioning started with measurements of the injection optics at an energy of 450 GeV [111]. This is shown together with the correction of this optics in Section 3.2.1. A successful correction of the injection optics paves the way for accelerating the particles up to an energy of 6.5 TeV. In Section 3.2.2 the results of the optics commissioning at top energy are presented up to the squeezed optics with a β-function at the ATLAS and CMS interaction points (β^*) of 40 cm. For the first time, three different optics with a β^* of 40 cm, 60 cm and 80 cm were commissioned together. A common correction which is constant in the range of the three β^* has been derived. This is not only a more time efficient approach for the commissioning, but would also facilitate β^*-leveling [112, 113].

3.2.1. Injection optics

Injection energy measurements exposed the N-BPM method and all other tools which are involved in the optics measurement to unexpected hardware and software related issues. During the first measurements at injection energy more than half of the BPMs were malfunctioning, and no reasonable measurements could be performed. While at the 2nd attempt of injection optics measurements this problem was resolved, further issues became visible. The oscillation amplitude of the recorded TbT data showed abrupt changes for beam 1 vertically, which was later attributed to a bad electronic connection of the AC dipole [111]. Furthermore, many BPMs showed a spike in the recorded TbT data, i.e. a value which is larger than 20 mm while the usual oscillation amplitude is below 2 mm. These spikes occurred randomly at different BPMs and at different turn numbers. It was decided to reject the BPMs where a spike occurred for the online analysis, since no simple workaround would ensure not to deteriorate further analysis. In order to keep a larger number of BPMs the TbT data was limited to 1700 turns, so that fewer spikes would occur and less BPMs are rejected. This issue was soon identified to be caused due to an incompatibility of the TbT acquisition mode and the average orbit acquisition, which can be avoided by disabling the latter during optics measurements. Thus it was not interfering with subsequent measurements at top energy.

The β-beating before optics correction is shown in Fig. 3.3 for beam 1 in comparison to measurements from 2012. The amplitude and pattern of the β-beating is very similar, although a few differences can be seen. In the horizontal plane, the β-beating in 2015 is slightly lower from IR2 to IR7 and slightly higher elsewhere. In the vertical plane the β-beating is even more similar, only between IR4 and IR5 it is smaller in 2015, and larger in between IR7 and IR8. Qualitatively one can draw similar conclusions for beam 2. For all plots in this section, the corresponding ones for beam 2 are shown in Appendix B.1. Since no strong local optics errors could be identified, global corrections were directly calculated as explained in section 1.3.2. Figure 3.4 shows the resulting β-beating after global optics corrections for beam 1, cf. Appendix B.1 for beam 2.

The β-beating was significantly reduced from a peak value of more than 30 % to 14 %.

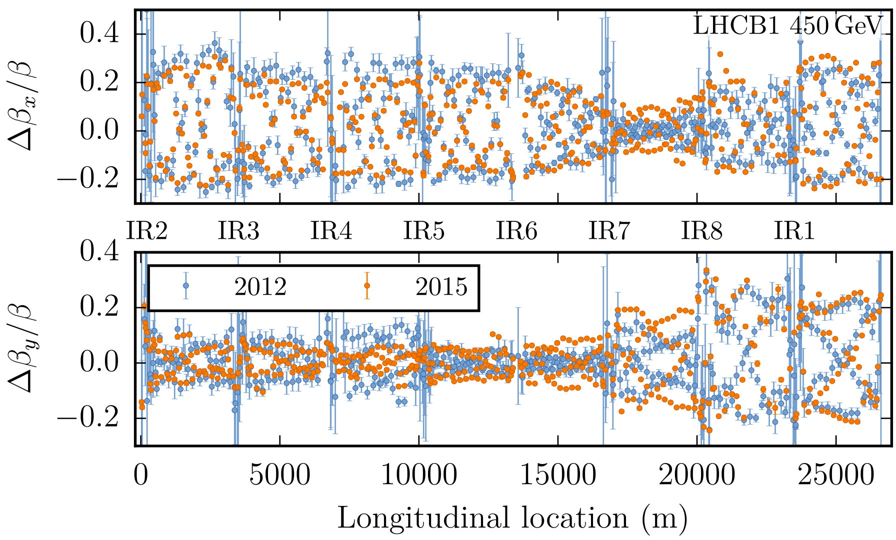

Figure 3.3.: β-beating at injection for beam 1. The measurement from 2015 was analyzed with the N-BPM method, while the one from 2012 used the previous neighboring BPM method.

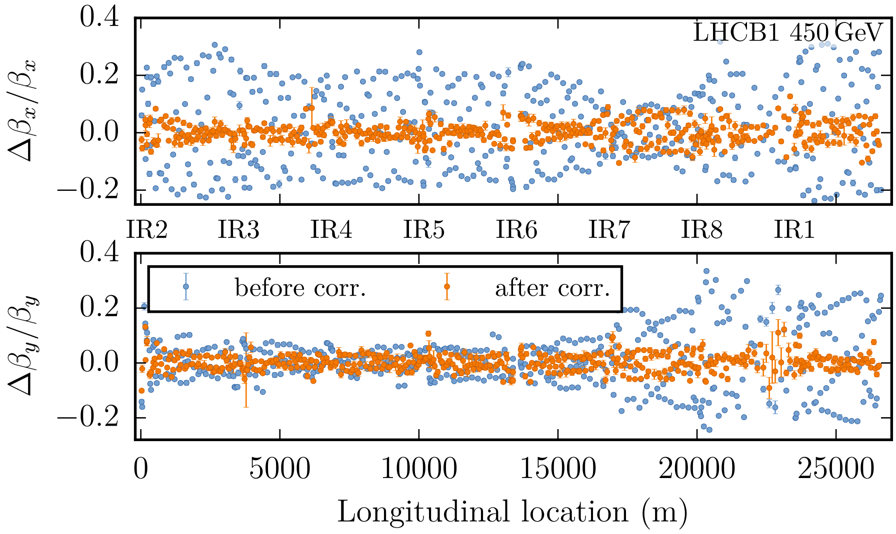

Figure 3.4.: β-beating at injection for beam 1 before and after optics correction. Both measurements were analyzed with the N-BPM method.

This is a good result, which is meeting the specified tolerable β-beating at injection, which is shown in Table 1.2, especially considering the unfavorable conditions of these measurements.

3.2.2. Squeeze of the interaction point β-functions

The optics commissioning for squeezed optics begins again with the measurement of the uncorrected machine, since many magnetic errors are energy dependent and the correction derived for injection energy will not be suitable at 6.5 TeV. During the squeeze, the β-function in the four interaction points is being reduced. The steps of the squeeze will in the following be characterized by the β-function in the ATLAS and CMS interaction point (β^*). Measurements were performed for several intermediate matched points of the optics along the squeeze from a β^* of 10 m to 40 cm. The minimum β^* of 40 cm in this commissioning is lower than in 2012, where it was 60 cm and even lower than the original design value for the LHC of 55 cm [14]. The results of the measured β-beating along the squeeze are shown in Fig. 3.5 in comparison to the measurements in 2012 at an energy of 4 TeV.
The rms β-beating for beam 1 vertically and beam 2 horizontally is very similar compared to 2012. The rms value is in general better suited for comparisons as it is more robust than a potentially very localized peak value. However, for machine protection considerations the peak value might be more important as certain deviations to larger β-functions could not be tolerated even if they occur only in a small region. The β-beating for beam 1 horizontally and beam 2 vertically are significantly smaller than in 2012, which is an indication that the optics errors significantly changed during LS1. This is discussed in more detail in Section 3.4. The maximum observed β-beating is larger than 110 % for a β^* of 40 cm, which is more than the 100 % that was observed in 2012 for a β^* of 60 cm.

Local corrections

Local corrections were computed using the SbS technique, cf. Section 1.3.1. The corrections for the final focusing magnets in the ATLAS and CMS interaction region are listed in Table 3.3, which also suggest a difference of the optics errors in 2015 compared to 2012. A complete list of all local corrections can be found in Appendix C. The resulting β-beating after local corrections is shown in Fig. 3.6 and compared to 2012. The maximum β-beating after local corrections is 15 % / 13 % (horizontally / vertically) which was 20 % / 25 % in 2012. The β-beating after local corrections in 2015 was already below the specified maximum tolerable β-beating for squeezed optics, cf. Table1.2, which was not the case in 2012 [43]. The significantly better local corrections in 2015 compared to 2012 indicate furthermore the good performance of the N-BPM method.

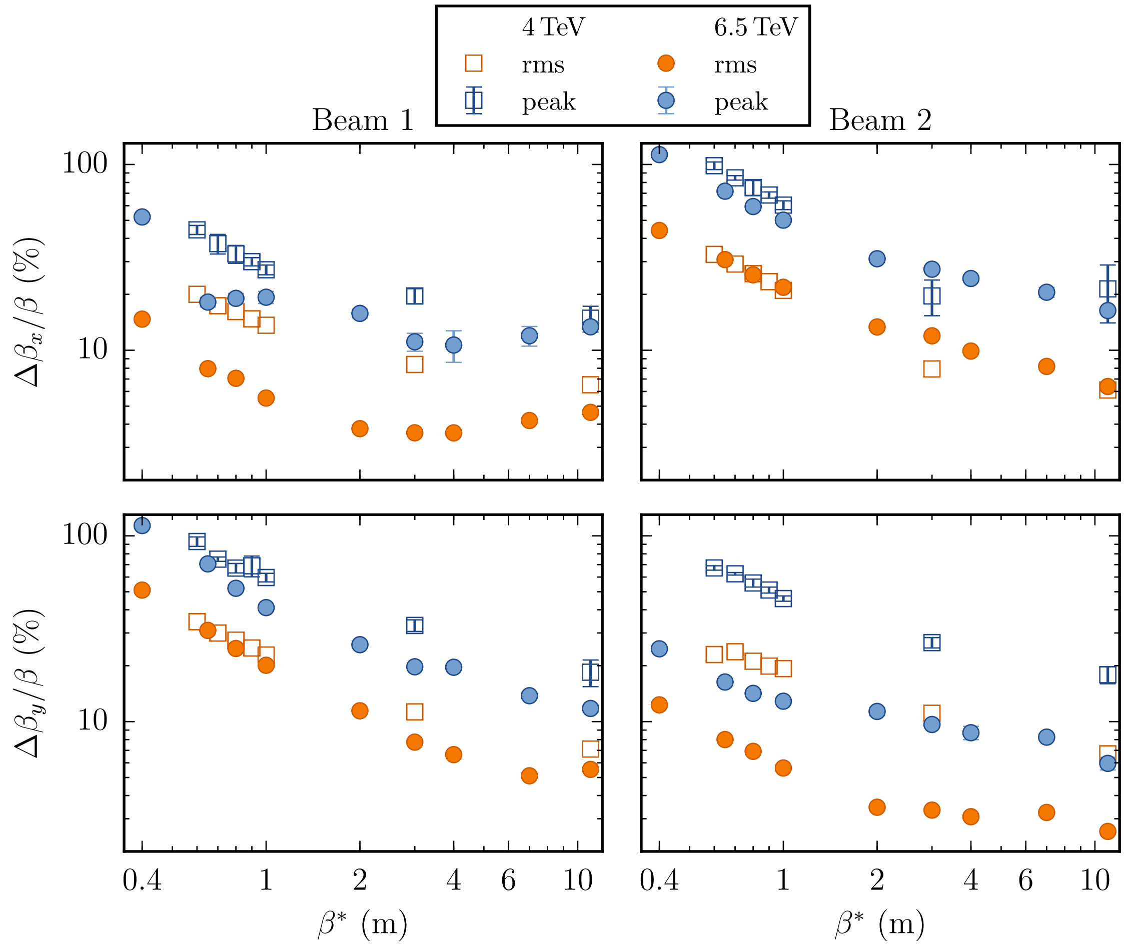

Figure 3.5.: Measured peak and rms β-beating before optics corrections. Values are given for different β^* along the squeeze. Measurements at 4 TeV were performed in 2012, and at 6.5 TeV in 2015.

Table 3.3.: Local correction strengths from run II compared to run I for final focusing quadrupoles in the ATLAS (IR1) and CMS (IR5) insertion region.

Location	**Circuit**	**Δk (10^{-5}m^{-2})**		**Relative (%)**
		2012	**2015**	**2015**
IR1	ktqx1.r1	1.0		
	ktqx2.l1	1.0	0.35	−0.04
	ktqx2.r1	−1.4	−0.7	+0.08
IR5	ktqx1.l5		2.0	−0.23
	ktqx1.r5		−2.0	−0.23
	ktqx2.r5	1.05	1.9	0.22
	ktqx2.l5	0.70	−0.09	0.01

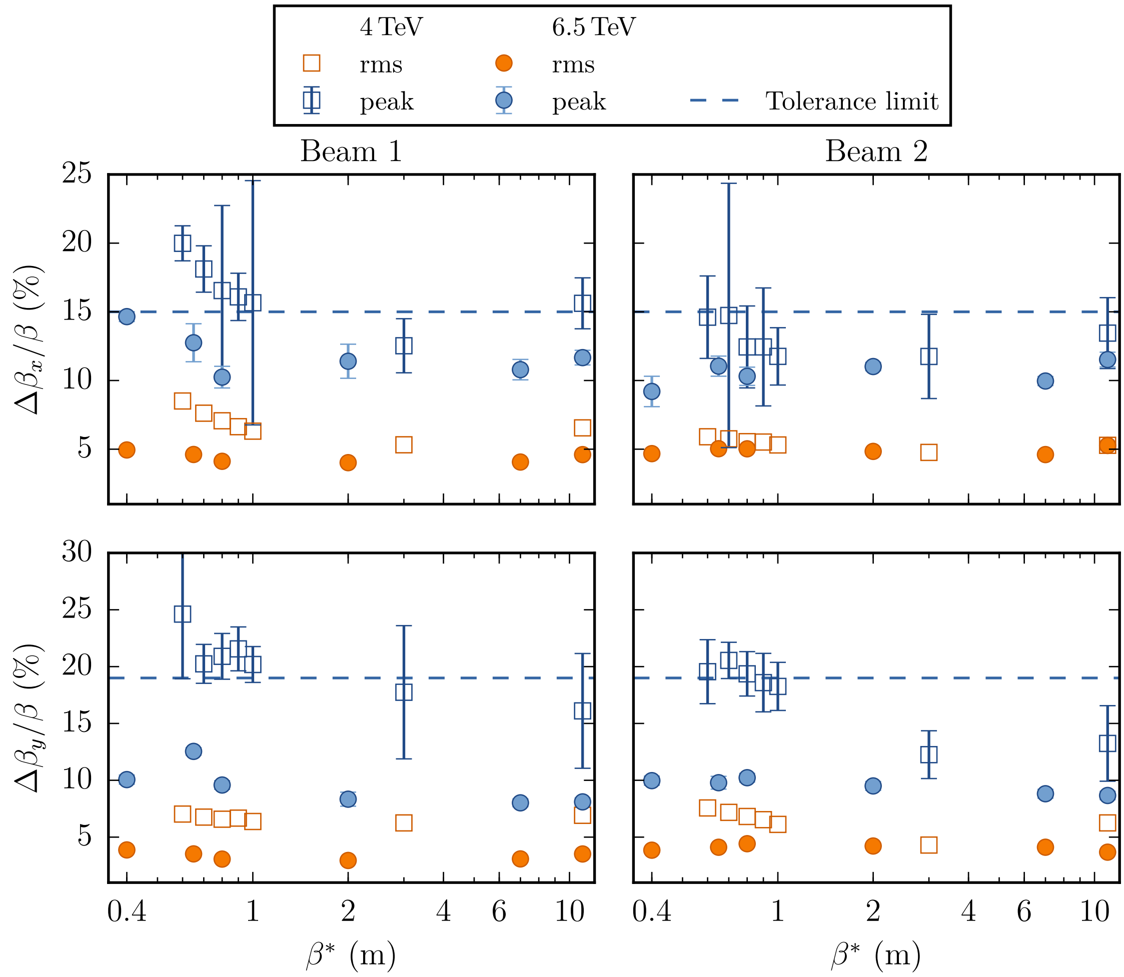

Figure 3.6.: Measured peak and rms β-beating along the β^* squeeze after local optics corrections have been incorporated. The maximum tolerable peak β-beating according to Table 1.2 is indicated as well.

Global corrections

As explained in Section 1.1.4, a smaller β^* is one way to increase the performance of a collider. The baseline for operation in 2015 foresaw an optics with a β^* of 80 cm [114]. Optics measurements and corrections were done up to a minimum β^* of 40 cm during the commissioning and MD sessions in 2015 [106], as the commissioning progress could reveal additional margins, e.g. in the aperture or from beam beam instabilities, that could be used up for an optics with a smaller β^*. Furthermore, it demonstrates that the optics are well under control for the smaller β^*, which might become operational in a future run. Measurements after local corrections were done for the low-β^* optics with a β^* of 80 cm, 65 cm and 40 cm. For the first time instead of deriving separate global corrections for each β^*, it was investigated whether a common correction would be possible for a range of β^*. This was already done for local corrections in 2012 [64]. It has the advantage of being more time efficient during the commissioning, as for the verification of the global corrections one does not have to remove the previous correction and apply a new correction when moving from one β^* to the next one. Furthermore, a constant correction for a range of β^* would facilitate β^*-leveling which might become important for future runs.
Global corrections were calculated for each β^* separately from the measured phase advances and dispersion as explained in Section 1.3.2. The expected β-beating after global corrections can be calculated by adding the β-beating that would arise from applying the corrections to the measured β-beating. This is shown in Fig. 3.7 for all possible combinations of applying the three calculated corrections to the three different β^*.
The expected β-beating shows, that the lowest β-beating is achieved if the correction is applied for the same optics from which it was derived. The β-beating becomes larger for larger differences between the β^* at which the correction is applied and the one from which it was computed. At this point during the commissioning it was clear that the β^* of 80 cm will be used for the physics run in 2015 [115]. Therefore, a preference was given to correct the 80 cm optics as good as possible. It was decided to use the 80 cm correction for all optics, since the maximum expected β-beating of in this case 12 % at a β^* of 40 cm is still acceptable according to the specified tolerable maximum β-beating in Table 1.2. The measured β-beating after applying the global corrections is shown in Fig. 3.7. The lowest β-beating is as expected achieved for the optics with a β^* of 80 cm. However, even the $\beta^* = 60$ cm optics is slightly better corrected than the optics with the same β^* in 2012 at an energy of 4.0 TeV, with a $(10-20)$ % lower rms β-beating, cf. Table 3.1. For a deviation of a factor two, between the β^* at which the correction is computed, and the β^* at which it is applied, the expected average rms β-beating increases by a factor two as well.

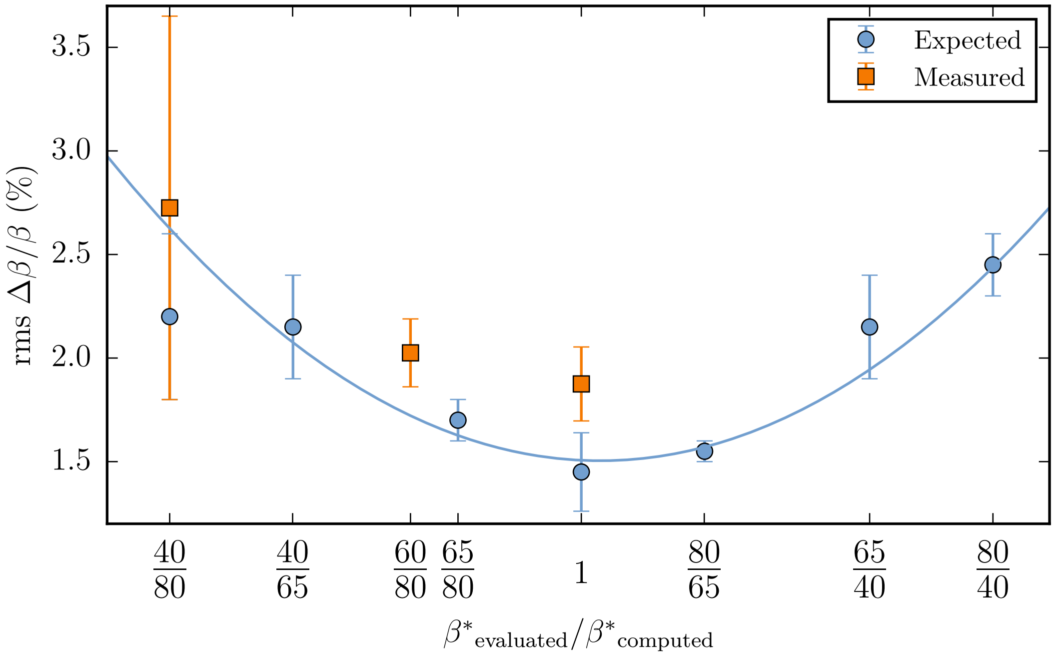

Figure 3.7.: The expected rms β-beating is shown for different β^* after evaluating different global corrections which have been computed from measurements at a β^* of either 80 cm, 65 cm or 40 cm. A fit with a parabola in a logarithmic horizontal axis is shown. The expected β-beating at $\beta^*_{\text{evaluated}}/\beta^*_{\text{computed}} = 1$ includes the three cases of evaluating the global correction for the same optics from which they were computed. The measured rms β-beating is shown for the three cases of applying the global corrections computed at $\beta^* = 80$ cm to the three optics with a β^* of 80 cm, 60 cm and 40 cm.

3.2.3. Overcoming the limiting factors of 2015

After the optics commissioning for the proton run in 2015, several issues were discovered which affected the optics measurements and limited ultimately the correction performance. These issues are discussed in the following paragraphs, together with ways to mitigate them. Finally, results from the optics commissioning in 2016 are shown.

Dispersion measurements

Quadrupole movements in IR8 [116], which resulted in drifts of the beam orbit, have disturbed many dispersion measurements. This limited global corrections, since the betatron phase and dispersion are corrected together, cf. Section 1.3.2. In Figure 3.8 the measured normalized dispersion is shown before and after global corrections. The very large error bars are a direct effect of the orbit drifts. Moreover, the values of the normalized dispersion before and after correction are very similar, which shows that the correction performance was limited. The quadrupole movements were found to be caused by a problem with a regulation valve of the cryogenic system [117]. After this issue has been fixed, reliable dispersion measurements and corrections were possible again in 2016.

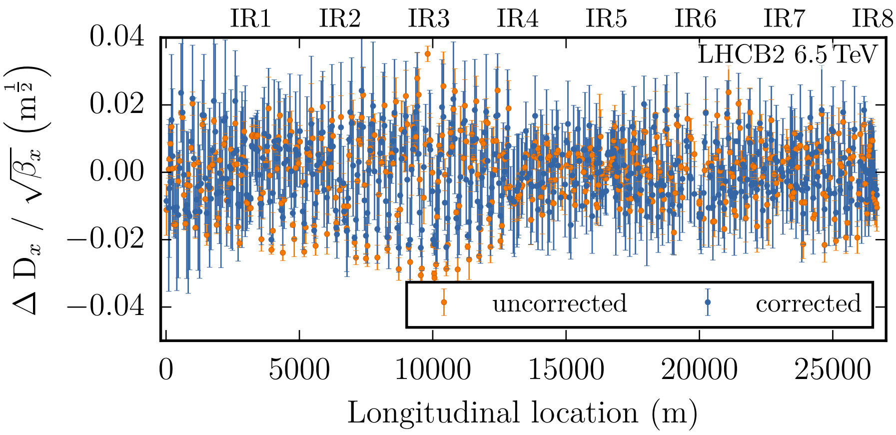

Figure 3.8.: Normalized dispersion before and after global corrections for beam 2 and $\beta^* = 80\,\mathrm{cm}$.

Interaction point β-functions

Despite the globally very well corrected optics, an average discrepancy of 6 % was observed in the interaction point β-function measured with k-modulation, cf. Table 3.4, which came along with an average absolute shift of the β-function waist of 19.1 cm, cf. Table 3.5.

First k-modulation results mistakenly suggested no significant deviation of the measured β^* to the model values in IR1 and IR5 [66]. An accurate analysis of the k-modulation measurements was only done at the end of the proton run, so that no correction of this effect was possible during the commissioning [119, 120]. Furthermore, the gradient errors of the triplet magnets that could cause the measured waist shift are 4 times larger than the assumed gradient uncertainties. The assumptions of the gradient uncertainties were based on WISE [89, 90], which provides smaller uncertainty values than [121]. Both references however do not fully explain the observed errors in the triplet magnets, which could possibly be related to larger misalignment

Table 3.4.: β^* for the 80 cm optics from k-modulation measurements [118].

		$\boldsymbol{\beta^*}$ **(cm)**	
		horizontal	**vertical**
Beam 1	IP1	87.8 ± 1.3	86.5 ± 0.7
	IP5	86.2 ± 1.1	86 ± 5
Beam 2	IP1	81.9 ± 1.3	82.7 ± 0.6
	IP5	86.7 ± 1.4	83 ± 2

Table 3.5.: Waist shift of the β^* for the 80 cm optics for the proton run from k-modulation measurements [118]. A positive value indicates a shift towards the focusing quadrupole in the corresponding plane.

		$\boldsymbol{\omega}$ **(cm)**	
		horizontal	**vertical**
Beam 1	IP1	24 ± 1	23 ± 1
	IP5	20 ± 1	15 ± 1
Beam 2	IP1	17 ± 2	21 ± 1
	IP5	22 ± 1	11 ± 1

uncertainties of these magnets. Therefore, neither was this deviation of the β-function waist expected, nor were turn-by-turn measurements sensitive enough to detect it.

Based on the k-modulation measurements, corrections for the β^* waist shift were calculated and successfully tested with protons during the optics commissioning for the ion run [118]. The relative quadrupole gradient changes of the corrections are for three of the triplet magnets as large as 0.23 %. The resulting waist shift after corrections is shown in Table 3.6, showing significantly smaller deviations, with an average absolute value of 3.9 cm.

An improved optics correction procedure was proposed which includes k-modulation measurement results already in the calculation of local and global optics corrections [122]. This required improved k-modulation tools which provide analysis results online for a direct use in the calculation of optics corrections [123].

Another approach to assure a good correction of the β^* values is based on TbT measurements. While the N-BPM method is less sensitive close to the IPs as the phase advance for consecutive BPMs is very small, the β-function from amplitude method, cf. Section 1.2.1, might provide more precise values. This requires however a good knowledge of the BPM calibration. Recent efforts try to calibrate the BPMs close to the IPs in beam based measurements of special optics where the final focusing magnets are switched off, the so called ballistic optics [124]. For this optics very precise results are expected from the N-BPM method which could be used to calibrate the BPMs close to the IPs.

Table 3.6.: Waist shift of the β^* for the 80 cm optics for the ion run from k-modulation measurements [118]. A positive value indicates a shift towards the focusing quadrupole in the corresponding plane.

		ω (cm)	
		horizontal	**vertical**
Beam 1	IP1	2 ± 4	5 ± 2
	IP5	-4 ± 5	1 ± 2
Beam 2	IP1	4 ± 3	-4 ± 2
	IP5	2 ± 4	-9 ± 3

Record low β-beating

For the LHC run in 2016 a smaller β^* was foreseen with $\beta^* = 40\,\mathrm{cm}$ as the ultimate goal [125]. Since no k-modulation measurements existed for the 40 cm optics, deviations of the β^* were unknown. The evolution of the β-function around its waist is described by

$$\beta(\Delta s) = \beta^* + \frac{(\Delta s)^2}{\beta^*}, \tag{3.1}$$

where β^* is the minimum β-function at the waist and Δs the longitudinal distance from the waist. Using this equation for the $\beta^* = 80\,\mathrm{cm}$ optics, the average waist shift of 19.1 cm from Table 3.5 would cause a 6 % deviation of the β^*, which is in accordance with the values observed in Table 3.4. Extrapolating this to the $\beta^* = 40\,\mathrm{cm}$ optics under the assumption of a similar waist shift results in a deviation of 25 % of the β^*. Since this would undermine the gains in luminosity of using the smaller β^* optics, a re-commissioning of the $\beta^* = 40\,\mathrm{cm}$ was done in 2016.

This commissioning showed the full potential of the improved optics measurement and correction techniques, as it was not limited from the aforementioned dispersion issue, and included k-modulation measurements in the correction procedure. The resulting β-beating after corrections is shown in Fig. 3.9 for beam 1 and in Fig. B.12 in Appendix B.2 for beam 2. The peak and rms β-beating values are compared in Table 3.7 to the results from previous years. Excellent low values for the rms β-beating of (1.4–1.6) % have been achieved. For the first time, a high-energy hadron collider is demonstrating an optics quality which is on par with low energy synchrotron light sources [126].

Table 3.7.: Achieved rms and peak β-beating after local and global corrections in the optics commissioning in 2012, 2015 and 2016.

	Beam 1		**Beam 2**		**Year**	**Energy**	β^*
	x	**y**	**x**	**y**		**(TeV)**	**(cm)**
peak $\frac{\Delta\beta}{\beta}$ (%)	9 ± 1	9 ± 1	7.0 ± 0.6	6.7 ± 1.7	2012	4.0	60
	9.6 ± 1.6	5.0 ± 1.0	11.2 ± 1.1	6.8 ± 1.2	2015	6.5	40
	7.8 ± 0.7	4.5 ± 0.7	5.0 ± 0.4	4.2 ± 0.3	2016	6.5	40
rms $\frac{\Delta\beta}{\beta}$ (%)	2.6	2.3	2.4	2.2	2012	4.0	60
	3.2	1.7	4.0	2.0	2015	6.5	40
	1.6	1.4	1.6	1.5	2016	6.5	40

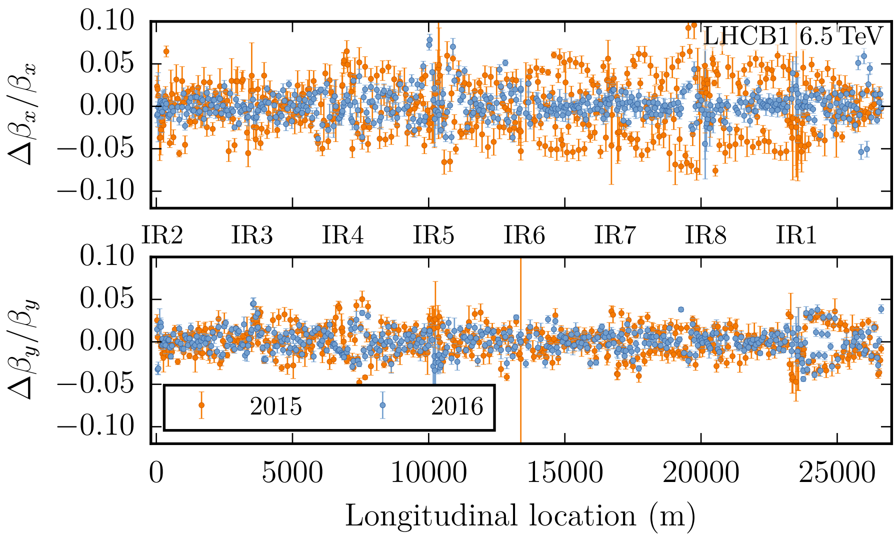

Figure 3.9.: β-beating for beam 1 at $\beta^* = 40\,\mathrm{cm}$ after corrections in 2015 and 2016.

3.3. β-functions during the energy ramp

In the commissioning of the LHC optics measurements and corrections are performed both at injection energy and at top energy. While the particles are accelerated to

higher energies, the gradient uncertainties for the magnets are changing. Furthermore, orbit errors during the energy ramp could introduce additional optics errors due to feed down effects. It is therefore of interest to assess the optics quality during the energy ramp as well. Besides, the optics behavior during the ramp is also of interest for other studies, e.g. for emittance measurement [82].
Performing optics measurements during the energy ramp is more challenging, since it is a continuous process which cannot be stopped at intermediate energies. K-modulation, which is generally used to measure the β-function with high precision at the location of certain quadrupoles, cannot be used during the energy ramp, since these measurements require stable optics over a period comparable to the length of the ramp. TbT measurements however are executed in less than one second, and are therefore ideally suited for these kind of measurements. A repetition of the measurement for several consecutive ramps is desired to estimate the uncertainty of the derived phase advances. This requires a precise coordination of the measurements, since the same points of the energy ramp need to be measured in every repetition.

3.3.1. Energy ramp to 4 TeV

A set of optics measurements in 2012 has been performed during the energy ramp from 450 GeV to 4 TeV. In 2012 during the energy ramp, an increase of the beam emittance was observed [127]. Furthermore, the emittance evolution showed an unexpected behavior by decreasing for a short time during the energy ramp. This triggered optics measurements during the energy ramp, to study how the β-function at the location of the wire scanners, which are used in the emittance measurements, evolves. The resulting β-functions at the wire scanners are shown in Fig. 3.10 together with the values from k-modulation measurements [128]. Beam 1 shows a deviation of the vertical β-function at 3 TeV, which might explain why an emittance shrinking is observed if only interpolated β values are used [129]. More measurements at different energies during the ramp are needed to further investigate this.

3.3.2. Combined ramp and squeeze to 6.5 TeV

In the current operation of the LHC the optics squeeze, i.e. the process of reducing the β-function in the IPs, is following the energy ramp. Studies have been done in the past for starting the squeeze already during the energy ramp, which would be a more time efficient approach [130, 131]. In 2015 the combined ramp and squeeze (CRS) was successfully tested for the first time with beam [132]. Optics measurements have been performed when the squeeze reached a β^* of 7 m, 4 m and 3 m in IP1 and IP5. Two ramps were performed and measured data of both ramps was analyzed together. The measured β-beating is shown in Fig. 3.11 for a β^* of 7 m and compared to a static

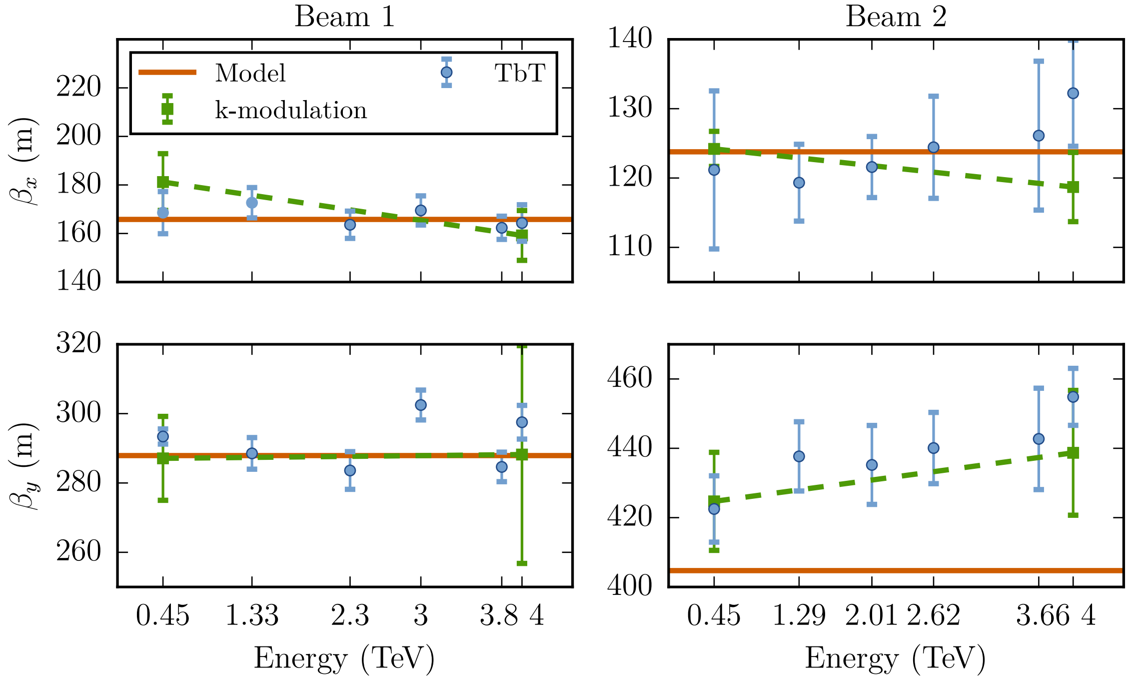

Figure 3.10.: Measured β-function at the wire scanners during the energy ramp. β values from a k-modulation measurement at 0.45 TeV and 4 TeV are shown as a comparison. The dashed line connects the two points from the k-modulation measurement at injection and top energy.

measurement of the standard squeeze. β-beating plots for the other β^* are listed in Appendix B.3. Measurement results are only available for beam 2, as beam 1 was lost at the beginning of both ramps. This issue was caused by a wrong setting and was not related to the CRS [132].

Although the precision of the measurement is lower compared to a static measurement, due to fewer acquired turns and fewer repetitions of the measurement, the agreement to measurements at 6.5 TeV is very good. The optics quality is no limit for a CRS to a β^* of 3 m and likely to even lower values.

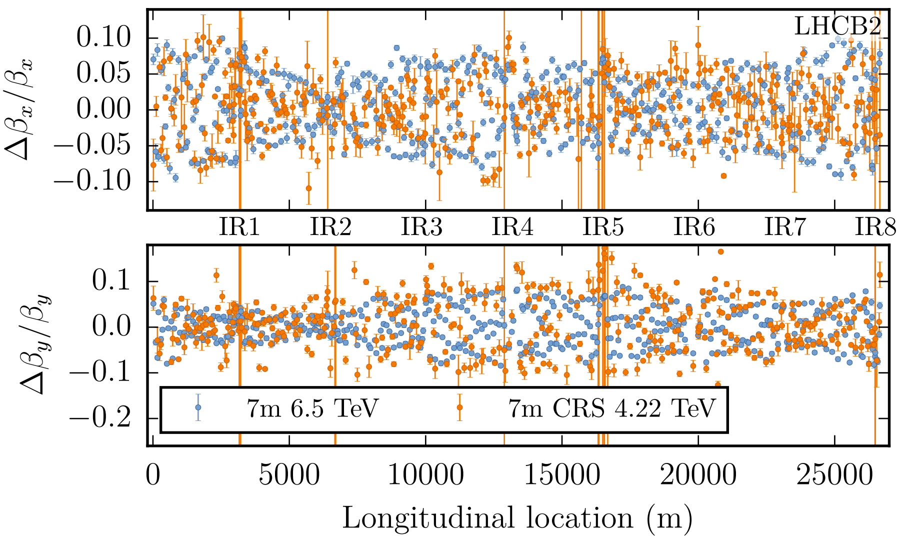

Figure 3.11.: β-beating for beam 2 during the CRS at an energy of 4.22 TeV and a β^* of 7 m in IP1 and IP5 in comparison to a static measurement at 6.5 TeV with the same β^*.

3.4. Optics stability

In this section the optics stability is studied for different time scales. During LS1 the BPM acquisition system and the ac dipole have been upgraded to allow for 6600 turns of beam excitation plateau and TbT acquisition for optics measurements. This corresponds to a duration of 587 ms with a sampling rate of one turn (89 µs). For measurements before LS1, the beam excitation and TbT acquisition were limited to 2200 turns (196 ms). The increased length of the TbT data allows for a closer look on the optics stability during beam excitations, which is discussed in Section 3.4.1.

For an optics measurement at a specific machine state, the TbT measurement is repeated several times. Single measurements are separated by at least one minute, to avoid overheating of the ac dipole [45]. For a usual measurement, five or more measurements are analyzed together to derive the optical functions, cf. Fig. 3.12.

Potential changes from one beam excitation to the next one are analyzed in Section 3.4.2. Furthermore, the benefit from the increased TbT acquisition time is discussed.

For larger time periods one can look at the stability of the optics for measurements which were performed on a different day, i.e. using a different beam, which is done in Section 3.4.3.

Finally, in Section 3.4.4 differences of the measured optics are investigated before and

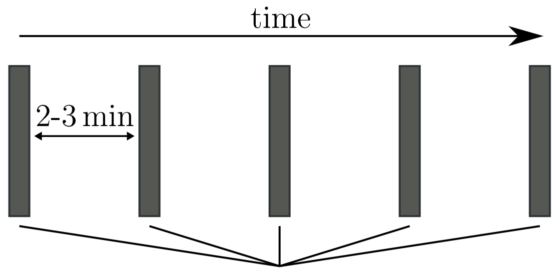

Figure 3.12.: Illustration of the time scale for a set of TbT measurements. Taking at least five measurements is recommended, based in the observations in Section 2.1.1. Additional measurement sets with different rf settings can be performed for probing off-momentum effects.

after LS1, which corresponds to a time period of 3 years.

3.4.1. Single beam excitations

The increased TbT data acquisition length allows for a more detailed look on the stability of the optics and the instrumentation used for the measurements on a time scale below one second. To study potential changes over time from the measurement files of 6600 turns only 2000 turns were used in the analysis, starting from different turn numbers in steps of 500 turns. The analyses of these files were performed according to Section 1.2.1. The noise reduction with an SVD was however performed on each file separately in order not to add additional correlations among the single files. One can now look at the evolution of observables like the driven (ac dipole) and natural tunes in both planes as well as the phase advances between BPMs. Figure 3.13 shows the evolution of the driven tune over time for beam 1 in both planes.
An increase of the driven tune in the order of 10^{-6} can be seen at turns 1000 to 2000. This behavior is neither seen in the vertical plane nor in any plane for beam 2. It is furthermore visible for different measurement days and different optics. No such behavior can be seen for the natural tunes of the machine. Therefore, an artifact of the ac dipole is suspected. The effect of this on the optics measurement precision is shown in Section 3.4.2.
The same evaluation can be done for the measured phase advances. In this case one has about 2000 observables (>500 BPMs per beam and per plane). The evolution of the phase advances for some BPMs show a tendency for a linear increase or decrease over time. To assess if this behavior is significant, for all BPMs a linear regression was performed for the evolution of the phase advance. This was done separately per plane and per BPM and for different optics. Figure 3.14 shows the distribution of the

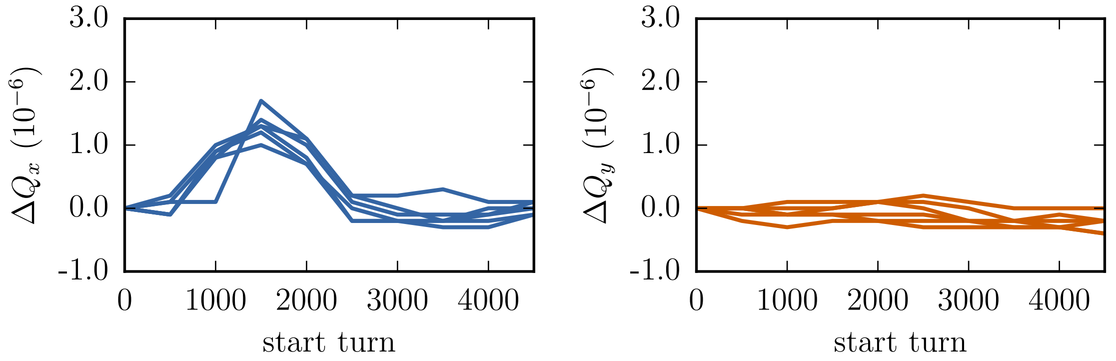

Figure 3.13.: Measured deviation of the ac dipole tune when 2000 turns out of 6600 were analyzed, starting from different turn numbers. The plots show six different measurements at a β^* of 80 cm.

two-sided p-values for a hypothesis test whose null hypothesis is that the slope of the linear regression is zero, cf. Appendix A.2, for beam 1 at a β^* of 80 cm. Under the hypothesis that there are significant drifts of the phase advances, one would assume a bias towards smaller p-values. Due to the uniform distribution this hypothesis is rejected. With the current measurement precision no drifts of the phase advances on time scales below one second are visible.

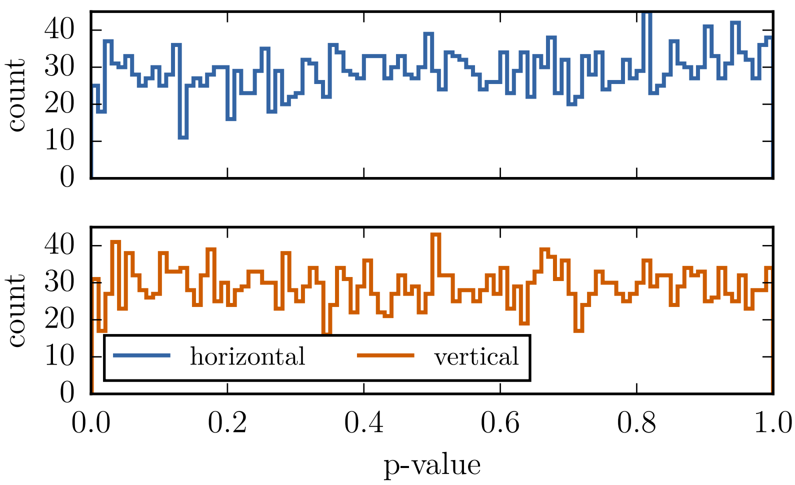

Figure 3.14.: Distribution of the p-values for a linear regression of the measured phase advances from six consecutive TbT analysis of 1100 turns each. The data was generated by splitting a measurement of 6600 turns into six pieces. The plot shows the case of a β^* of 80 cm for beam 1.

3.4.2. Repeated beam excitations

Repeated beam excitations allow to assess the uncertainty of the phase advance measurement, by computing its standard deviation for the different beam excitations at each BPM position. Depending on the number of measurements, a correction factor according to Section 2.1 is applied to the uncertainty. Figure 3.15 shows the distribution of the uncertainty of the phase advance measurement from within one beam excitation where the TbT data was split into six parts of 1100 turns, in comparison to using six different consecutive beam excitations. For the consecutive beam excitations also only 1100 turns were analyzed to obtain comparable results. The phase advance uncertainty remains the same independent of whether the standard deviation is computed from within one beam excitation or among separate ones. This indicates that with the current precision of the measurement no optics changes between consecutive beam excitations can be seen.

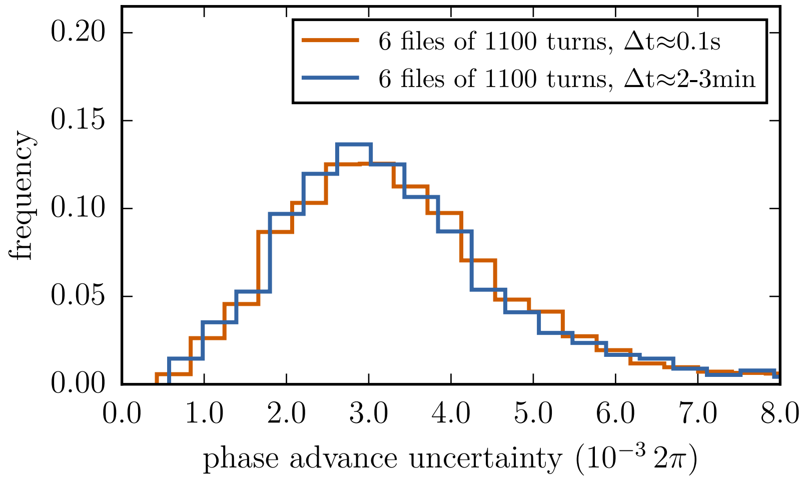

Figure 3.15.: Uncertainties of the measured betatron phase advances calculated from six measurement files of 1100 turns from one (Δt≈0.1 s) or multiple (Δt≈2-3 min) beam excitations for beam 1 at a β^* of 80 cm.

Figure 3.16 shows the distribution of the phase advance uncertainties for measurements from 2012 where up to 2200 turns of TbT data were recorded compared to 2015 (6600 turns of TbT data). One can clearly see, how the longer TbT data acquisition improves the precision of the measured phase advances. Moreover, a significant difference of the uncertainty is visible for the different planes. In both cases the horizontal phase advance has a larger uncertainty.
One reason for this can be attributed to the fact that the excitation amplitude in the horizontal plane was usually lower than in the vertical plane, which will decrease the

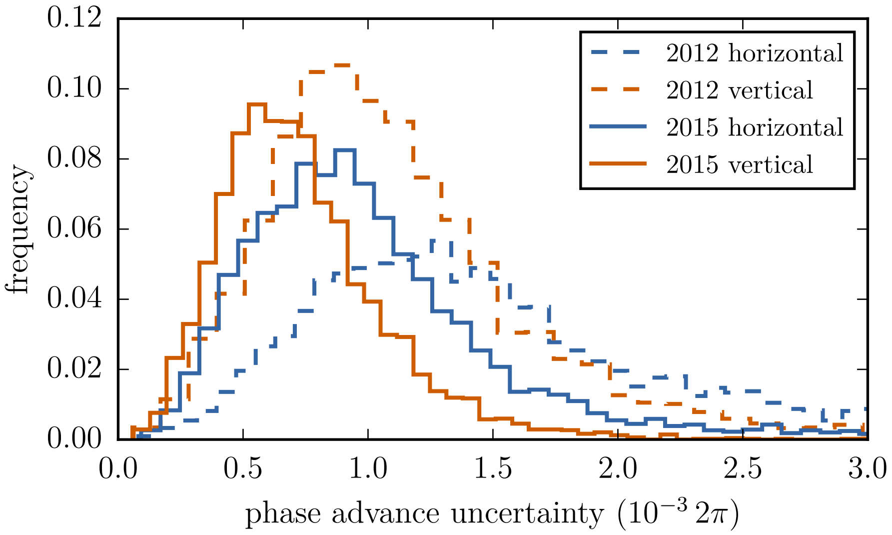

Figure 3.16.: Uncertainties of the measured betatron phase advances for both beams for optics with $\beta^* = 60\,\mathrm{cm}$ (2012) and $\beta^* = 80\,\mathrm{cm}$ (2015).

signal to noise ratio and therefore increase the measurement uncertainty, cf. Fig. 3.17. This happened because the strengths of the ac dipole kick need to be set manually and different values are required in both planes to achieve the same oscillation amplitude. This seemed to favor lower oscillation amplitudes for the horizontal plane. The graphical user interface (GUI) for these settings has been improved to display the peak-to-peak amplitudes of the betatron oscillations which should avoid this imbalance for future measurements [133].

Another contribution comes from the technical problem with the ac dipole which was already observed in Section 3.4.1. Figure 3.18 shows how the phase advance uncertainty depends on the number of turns analyzed. For beam 1 horizontally, where the measured ac dipole tune unexpectedly changes in between turn number 2000 to 3000, also the phase advance uncertainty increases with larger numbers of turns analyzed. The small deviation of the ac dipole frequency became only visible in a combined analysis of the TbT data from all BPMs, which made it difficult to find the source for this issue. In 2016, an amplifier of the beam 1 ac dipole for the horizontal plane stopped working and had to be replaced [134]. Measurements after the replacement confirmed, that the problem with the small frequency deviations disappeared. This highlights the resolution of the TbT analysis, which made discrepancies of the ac dipole visible before a complete defect occurred.

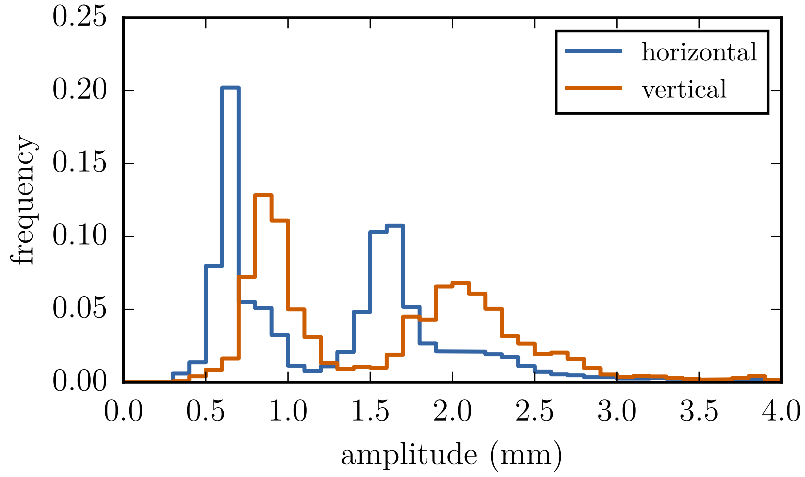

Figure 3.17.: Distribution of the beam oscillation amplitudes during TbT measurements at all BPMs for low-β^* optics in 2015. The two peaks in this distribution are due to the fact that most of the BPMs are located in the arcs where the β-function alternates between 30 m and 170 m at the BPM positions.

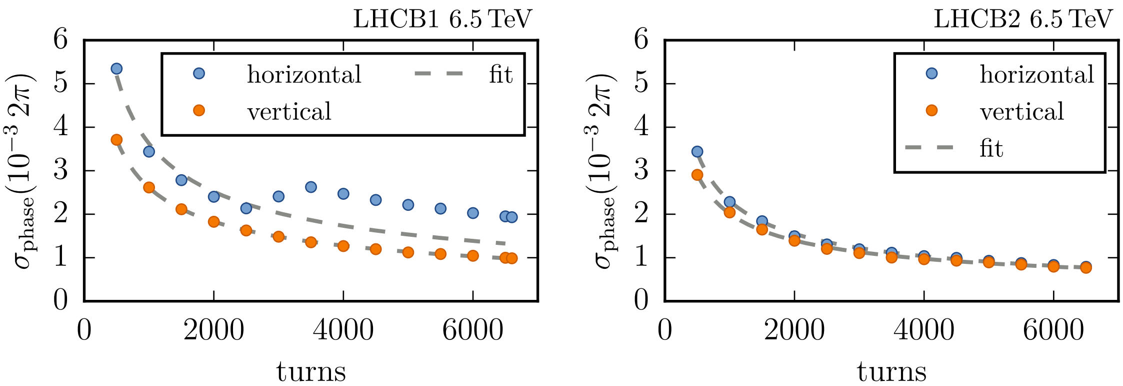

Figure 3.18.: Average precision of the measured phase advance for different number of turns used in the analysis for beam 1 (left) and beam 2 (right). The fit was done with a function proportional to $1/\sqrt{\text{turns}}$, and for beam 1 horizontally only the first five data points were used for the fit.

3.4.3. Repeated measurements with a different beam

In this section potential changes of the optics are investigated for time periods which are larger than one day. In contrast to the previous sections this implies that the measurements are taken with different particle beams. It is therefore affected by further uncertainties from the reproducibility of a certain machine state, since the machine will have undergone several operational cycles in between. For injection optics a repeated measurement after the commissioning was taken during a machine development session on the 28$^{\mathrm{th}}$ August 2015. Figure 3.19 shows the measured β-beating in comparison to the measurement during the commissioning. Both measurements are separated by 4 months. In general the β-beating is very similar in both cases. However, a few differences can be seen, for example the β-beating in the horizontal plane increased in the arc between IR5 and IR6 and similarly decreased in the arcs between IR8 and IR2. The changes of the β-beating are in the order of 2 % in these regions.
Repeated measurements exist also at an energy of 6.5 TeV with $\beta^* = 40\,\mathrm{cm}$ which are also separated by 4 months, cf. Fig. 3.20 and Fig. B.11 in Appendix B.2 for beam 2. Unfortunately, the second measurement was done with a smaller oscillation amplitude and fewer repetitions, which resulted in large error bars. Also for squeezed optics no larger deviations are observed, however not enough measurements of the same optics under the same conditions with reasonable error bars exist.

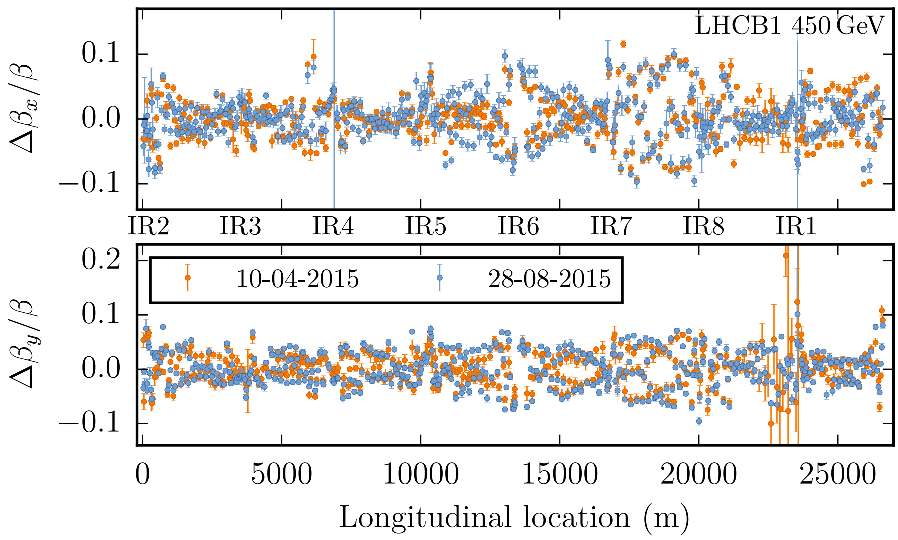

Figure 3.19.: Repeated measurement of the β-beating for beam 1 at injection after a time period of 4 months.

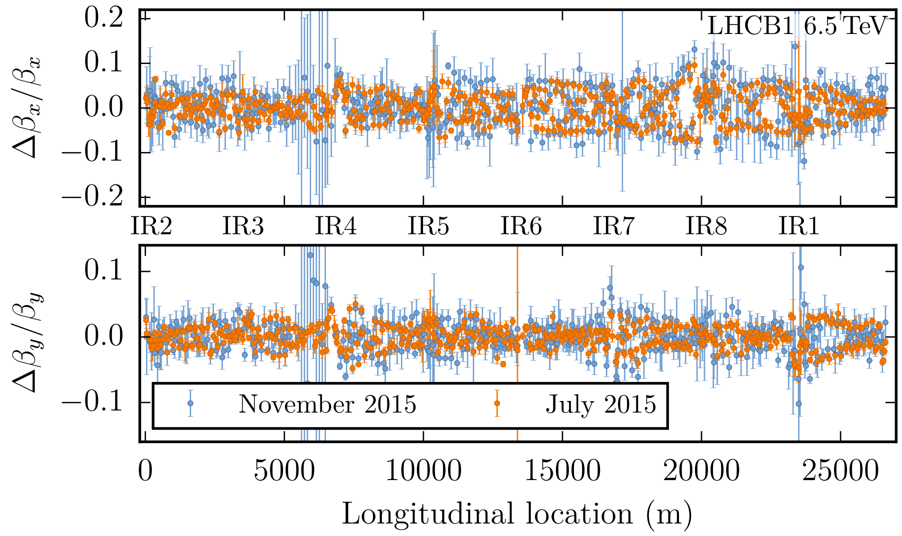

Figure 3.20.: Repeated measurement of the β-beating for beam 1 at a β^* of 40 cm after a time period of 4 months.

3.4.4. Differences after the long shutdown

Measurements before and after LS1 are separated by three years. Not only could changes over time be more expressed than in the previous section, but further errors could have been introduced due to the mechanical work during the shutdown. Figure 3.21 shows the β-beating before optics corrections for similar squeezed optics in 2012 and 2015, cf. Fig. B.10 in Appendix B.2 for beam 1. Significant differences can be seen in the β-beating especially in IR1 and IR5.

Also the local corrections which were derived in 2012 and 2015 deviate substantially, cf. Table 3.3. The effect on the betatron phase of the corrections from 2012 and 2015 is shown in Fig. 3.22 exemplary for beam 1 in IR1.

The deviations indicate that the 2012 corrections could not be reused after three years. Possible reasons for the discrepancy are (i) the different energy (4 TeV to 6.5 TeV), (ii) effects from the long technical stop, (iii) new misalignments and (iv) magnet ageing. A counterargument to the energy difference as the source of the discrepancy is the fact, that the optics errors that were observed in measurements at 2.51 TeV in 2015 were compatible with the ones at 6.5 TeV [135].

To further understand the behavior of optics perturbances over time, regular optics measurements once a year would be useful, especially since with the currently available data the optics stability for squeezed optics cannot be demonstrated for time scales of more than one year, and significant differences were observed after LS1.

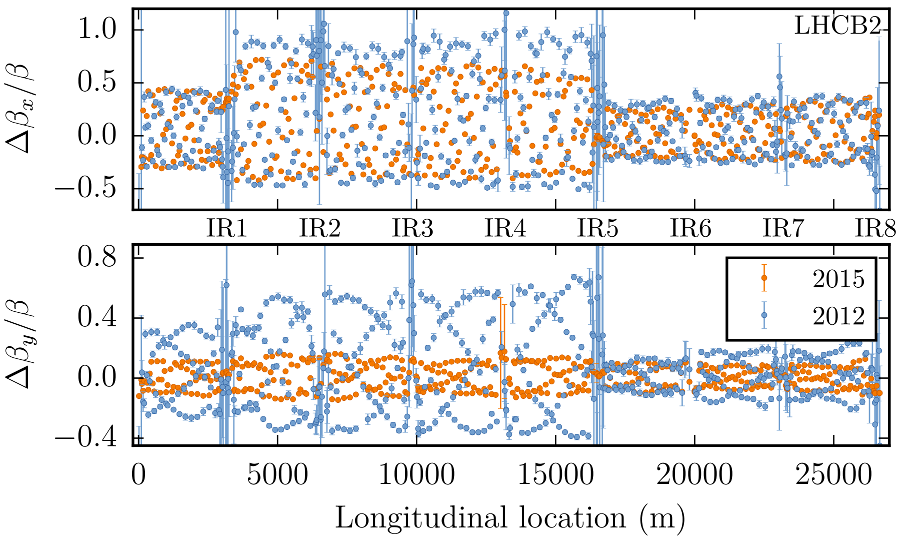

Figure 3.21.: β-beating before optics corrections for beam 2 at a β^* of 60 cm (2012 at 4 TeV) and 65 cm (2015 at 6.5 TeV).

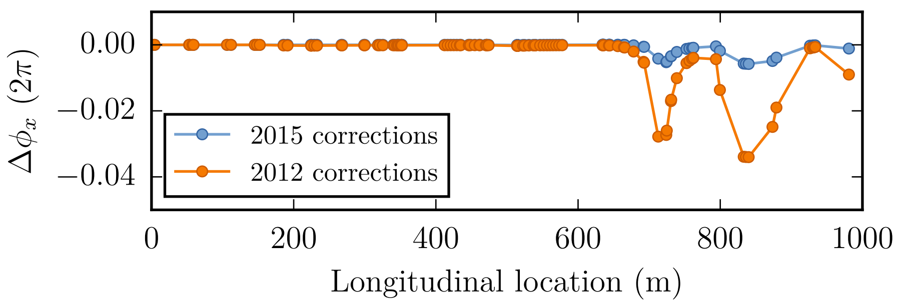

Figure 3.22.: Resulting deviations of the betatron phase for local corrections in IR1 of beam 1 which were used in 2012 and 2015.

4. High Luminosity LHC

The HL-LHC is a major upgrade of the LHC with significant performance improvements. The upgrades in the main IRs will be performed during the third long shutdown of the LHC in the 2020s. The goal on the integrated luminosity for HL-LHC of $3000\,\mathrm{fb}^{-1}$ is ten times more, than the expected value for the LHC up to the upgrade [136, 137]. This is achieved by enhancing key parameters which contribute to the luminosity, as shown in Table 4.1. A more precise equation for the luminosity than Eq. (1.1), includes a reduction factor $0 < R \leq 1$,

$$\mathcal{L} = \frac{1}{4\pi} \frac{N_1 N_2 f N_b}{\epsilon \beta^*} R, \tag{4.1}$$

which considers the hourglass effect due to the rapidly changing β-function around the IP, as well as the impact of the crossing angle of the two beams [20]. These effects are not negligible for the HL-LHC with its larger crossing angle, and would render the improvements for the luminosity ineffective. Therefore, an envisaged constituent of the HL-LHC is the compensation of the crossing angle effect by using crab cavities [138, 139] which are illustrated in Fig. 4.1. Moreover, the higher beam intensity increases the stored energy in the beam by about a factor of two, which increases the machine protection challenges [140]. For example, stronger dipole magnets, which achieve the same bending angle in a shorter distance, will make space available for additional collimators [141, 142]. Further improvements are new final focusing triplet magnets with a wider aperture, to allow for larger beam sizes. Together with a novel optics focusing concept, the achromatic telescopic squeezing (ATS) scheme, which is

Table 4.1.: Parameters for the HL-LHC in comparison to LHC, as shown in [136].

Parameter	**LHC**	**HL-LHC**
$N_{1,2}$	1.15×10^{11}	2.2×10^{11}
N_b	2808	2748
ϵ_N	3.75 µrad	2.5 µrad
Crossing angle	285 µrad	590 µrad
β^*	55 cm	15 cm
Virtual luminosity	$1.2 \times 10^{34}\mathrm{cm}^{-2}\mathrm{s}^{-1}$	$2 \times 10^{35}\mathrm{cm}^{-2}\mathrm{s}^{-1}$

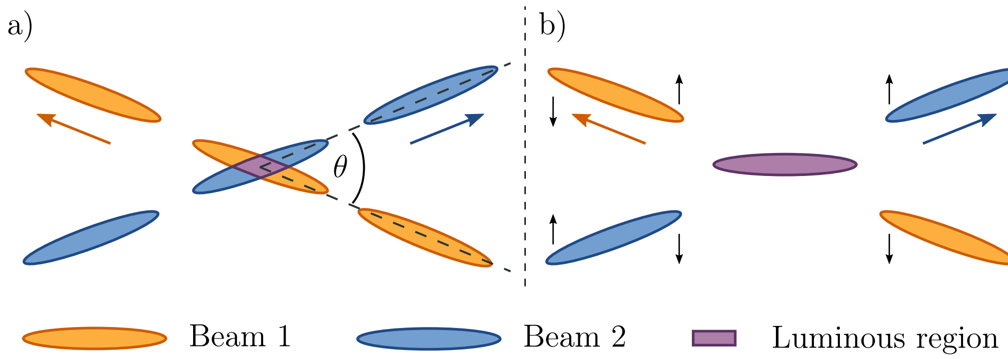

Figure 4.1.: Illustration of bunch crossings at an IP. In a) the effect of the crossing angle θ between the beams is shown, which reduces the luminous region where particle collisions occur. The luminous region becomes smaller for larger crossing angles. In b) the same setting is shown with additional crab cavities before and after the crossing. The transverse deflection of the bunches allows effectively for head-on collisions and compensates the luminosity reduction due to the crossing angle.

foreseen for the HL-LHC, this will allow for lower β^* [143].

4.1. ATS optics measurements

Tests of the ATS optics have been performed in the LHC during MD sessions in 2011 and 2012 [144–147]. In 2012, optics measurements were performed for a β^* of 40 cm, 20 cm and 10 cm. Local corrections were computed and tested at a β^* of 20 cm. Only beam 1 was available for measurements at $\beta^* = 10$ cm, as beam 2 was lost at $\beta^* = 14$ cm, due to a wrong setting [147]. These measurements have been re-analyzed with the N-BPM method. The β-beating before and after local corrections at $\beta^* = 20$ cm is shown in Fig. 4.2 for beam 1. β-beating plots for the other cases are listed in Appendix B.4. Unexpectedly, the local corrections did not improve the β-beating. During the re-analysis, it was found that the reason for this was an incompatibility between magnetic strength definitions in MAD-X for ATS optics and the software for finding optics corrections, which effectively overwrote the correction value for one quadrupole powering circuit. As a consequence the applied correction differed from the envisaged one. It was possible to re-construct the actual magnet settings as they were applied to the accelerator. The prediction from the actual correction is in excellent agreement with the measured phase deviation after local corrections, as shown in Fig. 4.3. It is therefore very likely that local correction could significantly improve the observed β-beating for ATS optics, however an experimental

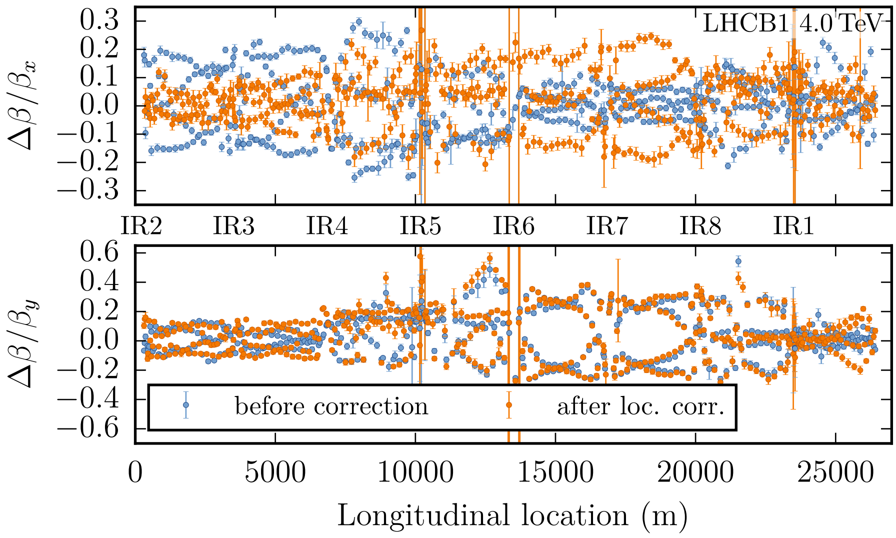

Figure 4.2.: Beta-beating for beam 1 for ATS optics with $\beta^* = 20\,\mathrm{cm}$, before and after local corrections.

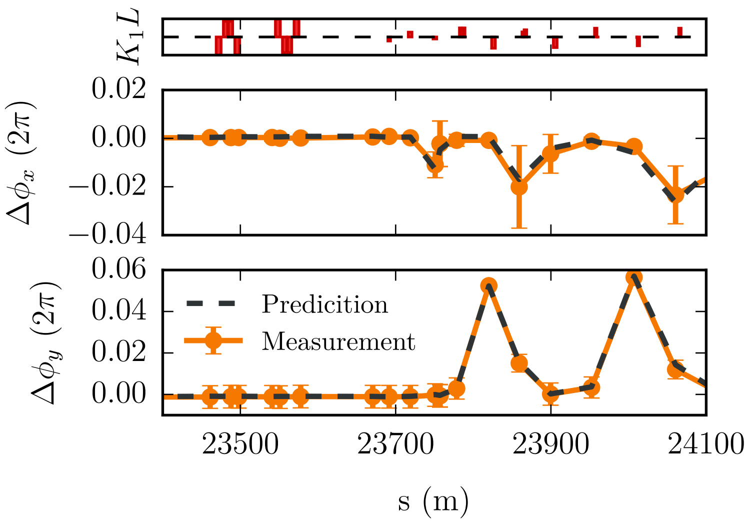

Figure 4.3.: Deviation of the propagated phase advance in SbS after local corrections for ATS optics for beam 1 at $\beta^* = 20\,\mathrm{cm}$. For successful corrections a flat line would be expected, cf. Section 1.3.1. Due to a wrong magnet setting in the corrections, the actual prediction of the phase deviation differs from this expectation. However, it is in excellent agreement with the measurement.

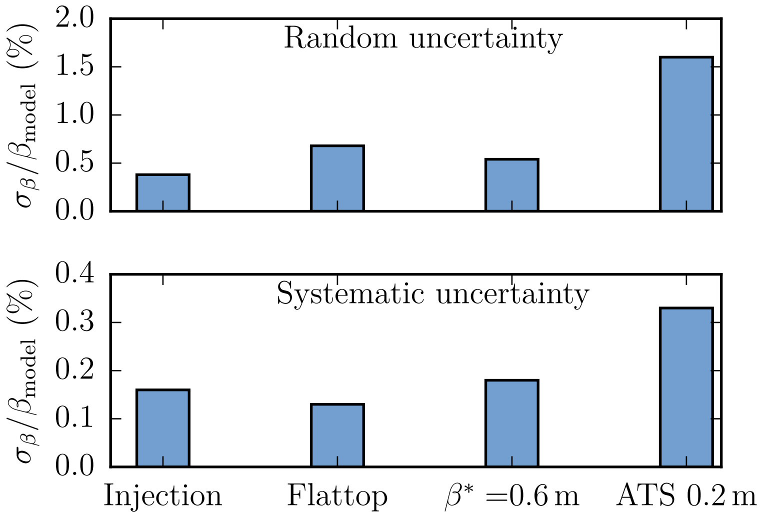

Figure 4.4.: Average relative uncertainty of the measured β-functions. Injection measurements are performed at 450 GeV, while all other measurements are at 4 TeV.

demonstration is still required.
The uncertainties of the measured β-functions are shown in Fig. 4.4 exemplary for a β^* of 20 cm. The uncertainties are compared to further measurements from 2012 with different optics configuration, namely at injection, after the energy ramp to 4 TeV (Flattop), and for a β^* of 60 cm. ATS optics measurements show about a factor two larger random and systematic uncertainties. One reason for the larger systematic uncertainties is the larger β-function in several arcs and in the experimental IRs [148]. Furthermore, random uncertainties of the measured phase are expected to increase as well, due to the larger average β-function, which results in a larger phase jitter [149].

4.2. Optics correction challenges

The impact of perturbations on the optics, and their correctability is simulated for the HL-LHC in comparison to the LHC. For the HL-LHC simulation, the lattice and optics version HLLHCV1.1 is used [150]. The same field errors from Table 2.2 and the b_2 uncertainty of the main dipoles, as described in Section 2.2, are used for both the LHC and the HL-LHC. Additional uncertainties are assumed for the new magnet types of the HL-LHC, as shown in Table 4.2. The following error tables are used for the b_2 uncertainty of IR dipole magnets, *D2_errortable_v5_spec*, *MBH_errortable_v1* and *D1_errortable_v1_spec* [151]. In this simulation, global corrections are tested.

It is assumed that previous local correction would have successfully corrected errors of the final focusing triplet magnets, cf. Table 4.2.

Table 4.2.: Gradient errors of different quadrupole magnet families. For MQYL the same uncertainty as for the LHC MQY magnet is assumed as they are of the same magnet type, cf. Table 2.2. For the final focusing triplet magnets (MQX) a residual uncertainty is assumed after successful local corrections.

Quadrupole family	**Error relative to the main field (10^{-4})**
MQYL	8
MQYY	10
MQX	2

10^3 lattices are simulated by randomly applying the uncertainties, following a Gaussian distribution, truncated at three standard deviations. The distribution of the resulting peak β-beating is shown in Fig. 4.5. The peak β-beating distribution for the LHC is consistent with measurements after local corrections, cf. Appendix C and [64]. The resulting β-beating due to the optics perturbations is about a factor two to three worse for the HL-LHC.
A response matrix, based on the ideal model, is calculated according to Section 1.3.2. For each case a global optics correction is calculated according to Eq. (1.54), assuming no uncertainty of the phase advances. The peak β-beating distribution after the correction is shown in Fig. 4.6.
Even after one iteration of global optics corrections, the peak β is still a factor two worse in comparison to the LHC. This emphasizes the challenges that lie ahead for optics corrections at the HL-LHC.
As shown in Section 3.2.3, the β-function from phase advance computation, reaches its limits around the IP for very low β^*, as the phase advance in between BPMs is in the order of the measurement uncertainty. Using only the phase information in SbS for local optics corrections is insufficient for the HL-LHC [152]. Several improvements are under development to cope with this, by including the results from different measurement methods in SbS. K-modulation measurements were successfully used in the calculation of local and global optics corrections in the 2016 optics commissioning [123]. Furthermore, improvements of the BPM calibration with beam based measurements are developed, which will allow to derive precise β-functions from the amplitude information of TbT measurements [124], cf. Section 1.2.1. This method can give precise results at positions where the β-functions are very large, which is exactly the region where the N-BPM method is limited.

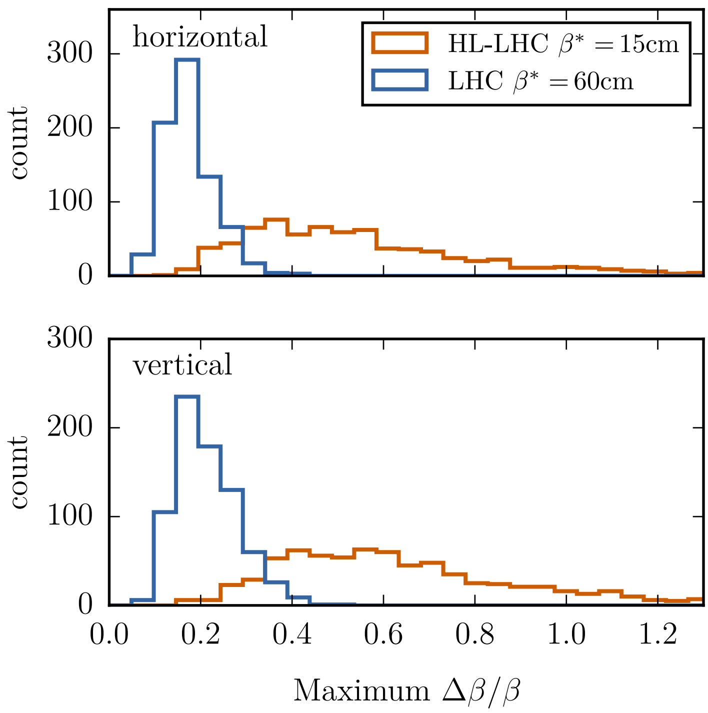

Figure 4.5.: Peak β-beating distribution before optics correction.

The use of ballistic optics, where the triplet magnets are not powered, can furthermore be used to disentangle optics corrections of the triplets from other IR magnets, which has been tested in an MD [153].
Combining the results from these different available measurement techniques, each with different weaknesses and strengths, is a promising approach to cope with more demanding optics correction scenarios.

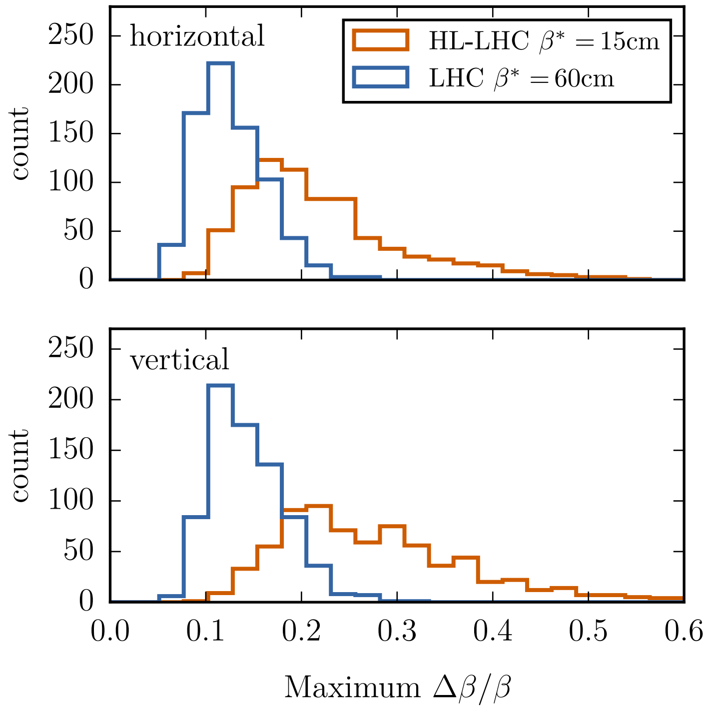

Figure 4.6.: Peak β-beating distribution after one iteration of global optics correction.

Conclusion

In this thesis, advancements in the measurement and control of the beam focusing properties of the Large Hadron Collider were presented. Measurement and control of the beam optics, specifically the β-functions, are essential for the performance reach of a particle collider. Furthermore, the LHC has tight tolerances on the allowed maximum deviation from its design parameters.

The β-function can be computed from the phase advance of the betatron oscillation between at least three beam position monitors (BPMs), which is derived from turn-by-turn (TbT) orbit measurements at these BPMs while an oscillation of the beam is excited. The measurement of the β-functions at one BPM position deteriorates, if too many BPMs are used with equal weights, as contributions from model errors increase. The N-BPM method, which is developed here, overcomes this limitation by performing a detailed analysis of statistical and systematic error sources and their correlations. This allows to use the measurement information from more BPMs to improve the precision and accuracy of the derived β-function. This method has been tested in simulations, as well as in comparison with k-modulation measurements at the LHC, and with the linear optics from closed orbit method (LOCO) at the ALBA accelerator. A re-analysis of the LHC measurement data from 2012 with the N-BPM method showed an improvement in the average error bar of the derived β-functions of at least a factor three, compared to the analysis from 2012.

The N-BPM method has been used online in the LHC control room during the optics commissioning at an unprecedented energy of 6.5 TeV. Its results were used to derive optics corrections which are used in operation. An improved optics quality has been demonstrated for optics with a stronger focusing, and hence smaller beam sizes at the collision points, than its design values. A new record low β-beating is achieved, and for the first time a high energy hadron collider is demonstrating an optics quality which is on par with synchrotron light sources.

Measurements during the energy ramp confirmed the good control of the optics during acceleration. This is a prerequisite for the combined ramp and squeeze scheme, which can reduce the turnaround time from one particle fill to the next one, and hence increase the integrated luminosity.

Studies of the optics stability were presented for different time scales. This benefited from recent upgrades of the ac dipole and TbT acquisition system, which allowed to increase the length of the beam excitation time for optics measurements. In this analysis a subtle change of the ac dipole excitation frequency was observed, which became only visible in the combined analysis of TbT data from more than 500 BPMs. No other available measurement technique had the required resolution to observe this deviation, which effectively increased the uncertainty of the measured betatron phase for beam 1 in the horizontal plane. The issue was resolved after an amplifier of the ac dipole was replaced.

Optics measurements which are separated by several months show that deviations of the measured β-function of up to 2 % may occur at injection. However, only few measurements under the same conditions were available. Measurements before and after the first long shutdown of the LHC (LS1), which are separated by three years, deviate significantly, so that optics corrections from 2012 could not be used again in 2015. The energy increase from 4 TeV to 6.5 TeV was ruled out as the source for this discrepancy, as measurements in 2015 at 2.5 TeV showed errors compatible with those observed at 6.5 TeV. To further understand this behavior, regular optics measurements once a year should be performed.

Large efforts for optics measurements from TbT orbit data at ALBA resulted in a great step forward in the calculation of β-functions from the phase of the betatron oscillation at synchrotron light sources. Deriving systematic errors and correlations in the N-BPM method successfully increased the optics measurement precision. The agreement with LOCO is now at a level of 1 %. For the first time TbT measurements and LOCO show the same level of precision in the measurement of β-functions at a synchrotron light source. This also sparked the interest at other machines, and the N-BPM method was tested at ESRF with great success [154].

Measurements with a new optics scheme which is foreseen for HL-LHC had been performed in 2012, where the computed local corrections were unsuccessful in improving the β-beating. A re-analysis of these measurements was presented, revealing that due to a software incompatibility different correction settings were applied to the machine than the envisaged one. Taking this into account, the measurement after correction was in good agreement with the expectation, which indicates that there was in principle no obstacle for optics corrections for this optics.

Optics corrections for the HL-LHC were studied in simulations. It was shown how the stronger focusing will significantly increase the β-beating before corrections. It will moreover challenge optics measurements with the N-BPM method around the collision points, due to even smaller phase advances between BPMs. Furthermore, optics measurements will become more difficult, as the increased average β-function amplifies the phase jittering, which results in larger random errors. Simulations show that systematic errors are expected to increase as well. Several approaches were described, which are under development, to cope with the more challenging scenarios for optics measurements and corrections. This includes combining the data from different measurement techniques, which will complement the N-BPM method in regions where it becomes less efficient.

In summary, the present work highlights the benefit of a careful analysis of systematic and statistical errors and their correlations, to increase the accuracy and precision of the derived parameters. The N-BPM method sets new standards for optics measurements at high energy particle colliders and synchrotron light sources. The improvements condensed into a significantly enhanced quality of the beam optics at the LHC. This provides additional margins for the aperture requirements of the beam, which could be used to increase the machine performance by operating with stronger beam focusing. As a result, the LHC is since 2016 operating with a smaller β^* at the collision points, than its design specifications. The N-BPM method will continue to play a crucial role for further advancements of the machine performance and future upgrades.

Acknowledgments

The work presented in this thesis would not have been possible without the support of many people. First, I want to express my sincere gratitude to my CERN supervisor Rogelio Tomás. His advices were invaluable and I am glad for the opportunity to learn from such a dedicated expert. I appreciate his patience and the very quick replies whenever I was looking for feedback. It has been a pleasure to work with him. Furthermore, I would like to thank my university supervisors Eckhard Elsen and Jörg Roßbach for their guidance during this time. I am very thankful for the constructive discussions about my work progress.

I am grateful to the members of the BE-ABP group for the positive work atmosphere and especially to Gianluigi Arduini, Oliver Brüning and Massimo Giovannozzi. Thank you also to Delphine Rivoiron for her support in administrative tasks. I would like to thank also Bernhard Holzer for his assistance and advice.

I am thankful to Per Hagen and Ezio Todesco for giving me insight into the field gradient uncertainties of the LHC magnets.

I would like to thank the LHC operation group and especially Jörg Wenninger for their assistance during optics measurements. Thanks also to Nicolas Magnin for his support related to the ac dipole.

I am furthermore very grateful to the night owls of the optics measurement and correction team. It has been a pleasure working with you, also during the exhausting LHC commissioning period. Special thanks to Ewen Maclean and Tobias Persson who explained me many things about the analysis tools, and who helped me to setup simulation scripts when I started at CERN. Thanks also to Jaime Coello de Portugal and Viktor Maier for programming related discussions and for improving the measurement analysis code.

I am grateful to Maria Kuhn for providing the k-modulation measurement results. Thanks also to Andrea Franchi for the discussion about optics measurement analysis. Special thanks also to Gabriele Benedetti, Michele Carlà, Ubaldo Iriso and Zeus Martí for allowing me to participate in optics measurements at the ALBA light source and for providing me with further measurement data.

I am grateful for the financial support from the Wolfgang Gentner Scholarships of the Federal Ministry of Education and Research and would like to thank also Michael Hauschild, the coordinator of this program.

On a personal note I would like to express my gratitude to my friends for the enjoyable times we spent together. A big thank you goes to Oliver Stein, Pascal Hermes and René Meusel, who made life in the Geneva region much more attractive. Thanks also to my office mates Foteini Asvesta and Panagiotis Zisopoulos for the many discussions, especially the non-physics ones.
Finally, I would like to thank my family Erwin, Christine, Kim, Lissi, Erika, Traute, Uschi, Holger, Monika and Christina for their continuous support and in particular Annika for always being there for me.

Thank you all!

Acronyms

ac	alternating current
ALICE	A Large Ion Collider Experiment
ATLAS	A Toroidal LHC ApparatuS
ATS	achromatic telescopic squeezing
BPM	beam position monitor
dof	degrees of freedom
DS	dispersion suppression section
CERN	European Organization for Nuclear Research
CMS	Compact Muon Solenoid
CRS	combined ramp and squeeze
DA	dynamic aperture
FODO	focusing and defocusing quadrupoles in alternating order
GUI	graphical user interface
HL-LHC	High Luminosity Large Hadron Collider
IP	interaction point
IR	insertion region
IR1	ATLAS interaction region
IR2	Alice interaction region
IR3	Momentum cleaning insertion
IR4	Insertion for beam acceleration

IR5	CMS interaction region
IR6	Beam extraction insertion
IR7	Betatron cleaning insertion
IR8	LHCb interaction region
LEP	Large Electron-Positron Collider
LHC	Large Hadron Collider
LHCb	Large Hadron Collider beauty
LINAC2	50 MeV linear proton accelerator
LOCO	linear optics from closed orbit
LS1	the first long shutdown
LS3	the third long shutdown
MAD-X	Methodical Accelerator Design
MB	main dipole
MD	machine development
MQT	tune trim quadrupole
MQY	wide aperture quadrupole in the insertion
MQX	final focusing triplet magnets
MS	matching section
ORM	orbit response matrix
pp	proton-proton
PS	Proton Synchrotron
PSB	Proton Synchrotron Booster
QPS	quench protection system
rf	radio frequency

RHIC	Relativistic Heavy Ion Collider
sc	superconducting
SPS	Super Proton Synchrotron
rms	root mean square
SbS	segment-by-segment
SVD	singular value decomposition
TbT	turn-by-turn

Bibliography

[1] R. Widerøe, "Über ein neues Prinzip zur Herstellung hoher Spannungen", TH Aachen (1927). Arch. f. Elektrotechnik **21** (1928) DOI: 10.1007/BF01656341, https://link.springer.com/10.1007/BF01656341.

[2] G. Ising, "Prinzip Einer Methode Zur Herstellung Von Kanalstrahlen Hoher Voltzahl", Ark. f. Mat. Astr. och Fys. **18** (1925), https://cds.cern.ch/record/433984.

[3] M. S. Livingston, "Early History of Particle Accelerators", in *Adv. Electron. Electron Phys.* Vol. 50 (1980), DOI: 10.1016/S0065-2539(08)61061-6, https://linkinghub.elsevier.com/retrieve/pii/S0065253908610616.

[4] K. Wille, *The physics of particle accelerators* (Oxford Univ. Press, 2000), https://cds.cern.ch/record/560708.

[5] S. Y. Lee, *Accelerator Physics*, 3rd edition (World Scientific Publishing, 2011), https://cds.cern.ch/record/1425444.

[6] S. Machi, "Trends for Electron Beam Accelerator Applications in Industry", Rev. Accel. Sci. Technol. **04**, 1 (2011) DOI: 10.1142/S1793626811000562, http://www.worldscientific.com/doi/abs/10.1142/S1793626811000562.

[7] A. Todd, "Prospects for Accelerator Technology", Rev. Accel. Sci. Technol. **04**, 235 (2011) DOI: 10.1142/S1793626811000604, http://www.worldscientific.com/doi/abs/10.1142/S1793626811000604.

[8] O. Jäkel, "State of the Art in Hadron Therapy", in AIP Conf. Proc. Vol. 958, 70 (2007), DOI: 10.1063/1.2825836, https://scitation.aip.org/content/aip/proceeding/aipcp/10.1063/1.2825836.

[9] R. Whitney, D. Douglas, and G. Neil, "Airborne megawatt class free-electron laser for defense and security", in Proc. SPIE, edited by G. L. Wood, Vol. 5792 (2005), DOI: 10.1117/12.603906, http://proceedings.spiedigitallibrary.org/proceeding.aspx?articleid=863849.

[10] R. Alemany Fernandez, R. Averbeck, P. Bechtle, M. Boonekamp, T. Carli, et al., *The Large Hadron Collider - Harvest of Run 1*, edited by T. Schörner-Sadenius (Springer International Publishing, 2015), DOI: 10.1007/978-3-319-15001-7, https://link.springer.com/10.1007/978-3-319-15001-7.

[11] P. Giubellino, "Heavy Ion Physics at the LHC", Hadron Collider Physics Symposium (2008),
http://arxiv.org/abs/0809.1062.

[12] K. Schindl, "Space Charge", in CAS - CERN Accelerator School: Intermediate Course on Accelerator Physics (2003),
https://cds.cern.ch/record/941316.

[13] J. Haffner, *The CERN accelerator complex*, 2013,
https://cds.cern.ch/record/1260465.

[14] O. S. Brüning, P. Collier, P Lebrun, S. Myers, R. Ostojic, et al., *LHC Design Report*, Vol. 1 (Geneva, 2004), DOI: 10.5170/CERN-2004-003-V-2,
http://cdsweb.cern.ch/record/782076.

[15] B. Salvachua, R. W. Assmann, R. Bruce, D. Deboy, A. Marsili, et al., "Cleaning Performance of the LHC Collimation System up to 4 TeV", in Proceedings of IPAC2013 (2013),
https://cds.cern.ch/record/1574583.

[16] E. Holzer, B. Dehning, E. Effinger, J. Emery, G. Ferioli, et al., "Beam Loss Monitoring System for the LHC", in IEEE Nucl. Sci. Symp. Conf. Rec. 2005 (2005), DOI: 10.1109/NSSMIC.2005.1596433,
https://ieeexplore.ieee.org/lpdocs/epic03/wrapper.htm?arnumber=1596433.

[17] L. Coull, D. Hagedorn, V. Remondino, and F. Rodriguez-Mateos, "LHC Magnet Quench Protection System", in 13th International Conference on Magnet Technology (MT13) (1993),
https://cds.cern.ch/record/259538.

[18] "Interim Summary Report on the Analysis of the 19 September 2008 Incident at the LHC", Cern. Doc. EDMS 973073 (2008),
https://edms.cern.ch/document/973073/1.

[19] J. Baglio, A. Djouadi, and J. Quevillon, "Prospects for Higgs physics at energies up to 100 TeV", arXiv Prepr. (2015),
http://arxiv.org/abs/1511.07853.

[20] W. Herr and B. Muratori, "Concept of luminosity", in CAS - CERN Accelerator School: Intermediate Course on Accelerator Physics (2003), DOI: 10.5170/CERN-2006-002.361,
https://cds.cern.ch/record/941318.

[21] D. A. Edwards and M. J. Syphers, *An Introduction to the Physics of High Energy Accelerators* (Wiley-VCH Verlag GmbH, Weinheim, Germany, 1993), DOI: 10.1002/9783527617272,
https://doi.wiley.com/10.1002/9783527617272.

[22] D. W. Kerst and R. Serber, "Electronic orbits in the induction accelerator", Phys. Rev. **60**, 53 (1941) DOI: 10.1103/PhysRev.60.53, http://dx.doi.org/10.1103/PhysRev.60.53.

[23] N. Christofilos, "Focussing System for Ions and Electrons", US Patent 2,736,799 (1956), https://www.google.com/patents/US2736799.

[24] E. Courant and H. Snyder, "Theory of the Alternating-Gradient Synchrotron", Ann. Phys. (N. Y). **281**, 360 (2000) DOI: 10.1006/aphy.2000.6012, http://linkinghub.elsevier.com/retrieve/pii/S0003491600960123.

[25] J. Rossbach and P. Schmüser, *Basic course on accelerator optics*, 1994.

[26] J. O. Smith, *Introduction to Digital Filters with Audio Applications* (W3K Publishing, 2007), https://ccrma.stanford.edu/$\sim$jos/filters/.

[27] G. Ripken and F. Willeke, "On the Impact of Linear Coupling on Nonlinear Dynamics", in 14th International Conference on High-Energy Accelerators (1989), https://cds.cern.ch/record/204506.

[28] P. J. Bryant, "A Simple Theory for Weak Betatron Coupling", in CAS - CERN Accelerator School : 5th General Accelerator Physics Course (1992), https://cds.cern.ch/record/261066.

[29] M. G. Minty and F. Zimmermann, *Measurement and Control of Charged Particle Beams*, Particle Acceleration and Detection (Springer Berlin Heidelberg, Berlin, Heidelberg, 2003), DOI: 10.1007/978-3-662-08581-3, https://link.springer.com/10.1007/978-3-662-08581-3.

[30] A. Piwinski, "Observation of Beam-Beam Effects in PETRA", in Proc. PAC79 (1979), https://inspirehep.net/record/147893.

[31] W. Herr, "Tune Shifts and Spreads Due to Short and Long Range Beam-Beam Interactions in the LHC", CERN-LHC-Note-119 (1990), http://cds.cern.ch/record/207280.

[32] R. Tomás, "From Farey sequences to resonance diagrams", Phys. Rev. ST Accel. Beams **17** (2014) DOI: 10.1103/PhysRevSTAB.17.014001, http://link.aps.org/doi/10.1103/PhysRevSTAB.17.014001.

[33] S. Guiducci, "Chromaticity", in CAS - CERN Accelerator School : 4th General Accelerator Physics Course (INFN, Frascati, Italy, 1990), https://cds.cern.ch/record/223348.

[34] F. Zimmermann, "Measurement and correction of accelerator optics", in Joint US-CERN-Japan-Russia Particle Accelerator School on Beam Measurement (1998),
https://cds.cern.ch/record/363825.

[35] B. Holzer, "Lattice design in high-energy particle accelerators", in CAS - CERN Accelerator School: Intermediate Course on Accelerator Physics (2003),
https://arxiv.org/pdf/1404.0923.

[36] J.-P. Koutchouk, W. Scandale, A. Verdier, and M. Bassetti, "Optimization of the LHC Lattice and Chromaticity", in Proceedings of PAC87 (1987),
https://inspirehep.net/record/245489.

[37] D. Kaltchev, M. Craddock, R. Servranckx, and T. Risselada, "Momentum Cleaning in the CERN LHC", in Proceedings of EPAC98 (1998),
https://inspirehep.net/record/473159.

[38] R. Aßmann, J. B. Jeanneret, and D. Kaltchev, "Efficiency for the Imperfect LHC Collimation System", in Proceedings of EPAC02 (2002),
https://cern.ch/lhc-collimation/files/epac02/mople030.pdf.

[39] R. Aßmann, O Aberle, M Brugger, L Bruno, H Burkhardt, et al., "Designing and Building a Collimation System for the High-Intensity LHC Beam", in Proceedings of PAC03 (2003), DOI: 10.1109/PAC.2003.1288836,
https://ieeexplore.ieee.org/lpdocs/epic03/wrapper.htm?arnumber=1288836.

[40] A. Verdier, "The LHC IR6 optics", LHC Proj. Note 146 (1998),
http://cds.cern.ch/record/691998.

[41] L. Jin and F. Schmidt, "Dynamic Aperture Tune Scan for LHC Version 5 at Injection Energy", LHC Proj. Note 182 (1998),
https://cds.cern.ch/record/692049.

[42] R. Calaga, D. Jacquet, E. Metral, R. Miyamoto, N. Mounet, et al., "Collision tunes at injection and ramp", CERN-ATS-Note-2011-034 MD (2011),
https://cds.cern.ch/record/1504706.

[43] O. Brüning and S. Fartoukh, "Field quality specification for the LHC main dipole magnets", LHC Proj. Rep. 501 (2001),
http://cds.cern.ch/record/522049/files/lhc-project-report-501.pdf.

[44] R. Tomás, M. Aiba, A. Franchi, and U Iriso, "Review of Linear Optics Measurements and Corrections in Accelerators", in Proceedings of IPAC2016 (2016),
https://accelconf.web.cern.ch/AccelConf/ipac2016/papers/moyca01.pdf.

[45] J. Serrano and M. Cattin, "The LHC AC Dipole system: an introduction", CERN-BE-Note-2010-014 (CO) (2010),
http://cdsweb.cern.ch/record/1263248.

[46] R. Tomás, "Adiabaticity of the ramping process of an ac dipole", Phys. Rev. ST Accel. Beams **8** (2005) DOI: 10.1103/PhysRevSTAB.8.024401,
http://link.aps.org/doi/10.1103/PhysRevSTAB.8.024401.

[47] P. Forck, P. Kowina, and D. Liakin, "Beam position monitors", CAS - CERN Accelerator School,
https://cds.cern.ch/record/1213277.

[48] O. R. Jones, "LHC beam instrumentation", in Proceedings of PAC07 (2007), DOI: 10.1109/PAC.2007.4440723,
https://ieeexplore.ieee.org/lpdocs/epic03/wrapper.htm?arnumber=4440723.

[49] J. Irwin, C. X. Wang, Y. T. Yan, K. L. F. Bane, Y. Cai, et al., "Model-Independent Beam Dynamics Analysis", Phys. Rev. Lett. **82** (1999) DOI: 10.1103/PhysRevLett.82.1684,
http://link.aps.org/doi/10.1103/PhysRevLett.82.1684.

[50] P. Castro, J. Borer, A. Burns, G. Morpurgo, and R Schmidt, "Betatron function measurement at LEP using the BOM 1000 turns facility", in Proceedings of PAC93 (1993), DOI: 10.1109/PAC.1993.309235,
https://ieeexplore.ieee.org/lpdocs/epic03/wrapper.htm?arnumber=309235.

[51] P. Castro, "Luminosity and beta function measurement at the electron-positron collider ring LEP", PhD thesis (1996),
http://cds.cern.ch/record/316609.

[52] R. Tomás, "Normal form of particle motion under the influence of an ac dipole", Phys. Rev. ST Accel. Beams **5** (2002) DOI: 10.1103/PhysRevSTAB.5.054001,
http://link.aps.org/doi/10.1103/PhysRevSTAB.5.054001.

[53] R. Tomás, M. Bai, R. Calaga, W. Fischer, A. Franchi, et al., "Measurement of global and local resonance terms", Phys. Rev. ST Accel. Beams **8** (2005) DOI: 10.1103/PhysRevSTAB.8.024001,
https://link.aps.org/pdf/10.1103/PhysRevSTAB.8.024001.

[54] R. Miyamoto, S. E. Kopp, A. Jansson, and M. J. Syphers, "Parametrization of the driven betatron oscillation", Phys. Rev. ST Accel. Beams **11** (2008) DOI: 10.1103/PhysRevSTAB.11.084002,
https://link.aps.org/doi/10.1103/PhysRevSTAB.11.084002.

[55] R. Calaga, R. Tomás, and F. Zimmermann, "BPM calibration independent LHC optics correction", in Proceedings of PAC07 (2007),
https://cds.cern.ch/record/1058520.

[56] R. Miyamoto, M. Aiba, R. Tomás, and G. Vanbavinckhove, "Measurement of coupling resonance driving terms in the LHC with AC Dipoles", in Proceedings of IPAC2011 (2011),
https://cds.cern.ch/record/1382073.

[57] T. Persson, M. Gasior, A. Langner, T. Lefevre, E. H. Maclean, et al., "Experience with DOROS BPMs for Coupling Measurement and Correction", in Proceedings of IPAC2016 (2016),
https://inspirehep.net/record/1469590/.

[58] A. Franchi, L. Farvacque, F. Ewald, G. Le Bec, and K. B. Scheidt, "First simultaneous measurement of sextupolar and octupolar resonance driving terms in a circular accelerator from turn-by-turn beam position monitor data", Phys. Rev. ST Accel. Beams **17** (2014) DOI: 10.1103/PhysRevSTAB.17.074001,
http://link.aps.org/doi/10.1103/PhysRevSTAB.17.074001.

[59] S. White, E. Maclean, and R. Tomás, "Direct amplitude detuning measurement with ac dipole", Phys. Rev. ST Accel. Beams **16** (2013) DOI: 10.1103/PhysRevSTAB.16.071002,
http://link.aps.org/doi/10.1103/PhysRevSTAB.16.071002.

[60] E. H. Maclean, R. Tomás, M. Giovannozzi, T. H. B. Persson, P. K. Skowronski, et al., "Non-Linear Errors in the Experimental Insertions of the LHC", in Proceedings of IPAC2016 (2016),
https://accelconf.web.cern.ch/AccelConf/ipac2016/papers/thpmr038.pdf.

[61] T. H. B. Persson, Y. I. Levinsen, R. Tomás, and E. H. Maclean, "Chromatic coupling correction in the Large Hadron Collider", Phys. Rev. ST Accel. Beams **16** (2013) DOI: 10.1103/PhysRevSTAB.16.081003,
http://link.aps.org/doi/10.1103/PhysRevSTAB.16.081003.

[62] Y. Ohnishi, K. Ohmi, H. Koiso, M. Masuzawa, A. Morita, et al., "Measurement of chromatic X-Y coupling", Phys. Rev. ST Accel. Beams **12** (2009) DOI: 10.1103/PhysRevSTAB.12.091002,
http://link.aps.org/doi/10.1103/PhysRevSTAB.12.091002.

[63] B. Montague, "Linear Optics for Improved Chromaticity Correction", CERN-LEP-NOTE-165 (1979),
https://cds.cern.ch/record/443342.

[64] R. Tomás, T. Bach, R. Calaga, A. Langner, Y. I. Levinsen, et al., "Record low β-beating in the LHC", Phys. Rev. ST Accel. Beams **15** (2012) DOI: 10.1103/PhysRevSTAB.15.091001,
http://link.aps.org/doi/10.1103/PhysRevSTAB.15.091001.

[65] R. Calaga, R. Tomás, R. Miyamoto, and G. Vanbavinckhove, "Beta* Measurement in the LHC Based on K-modulation*", in Proceedings of IPAC2011 (2011),
http://cds.cern.ch/record/1382057.

[66] M. Kuhn, V. Kain, A. Langner, and R. Tomas, "First K-Modulation Measurements in the LHC during RUN 2", in Proceedings of IBIC2015 (2015),
https://ibic.synchrotron.org.au/papers/mopb046.pdf.

[67] J. Safranek, "Experimental determination of storage ring optics using orbit response measurements", Nucl. Instr. Meth. Phys. Res. A **388**, 27 (1997) DOI: 10.1016/S0168-9002(97)00309-4,
http://linkinghub.elsevier.com/retrieve/pii/S0168900297003094.

[68] C. Y. Tan, K. Seiya, A. K. Triplett, and L. R. Prost, "Optics Corrections with LOCO in the FERMILAB Booster", in Proceedings of IPAC2016 (2016),
https://lss.fnal.gov/archive/2016/conf/fermilab-conf-16-130-ad.pdf.

[69] G. Benedetti, D. Einfeld, Z. Martí, and M. Munoz, "LOCO in the ALBA Storage Ring", in Proceedings of IPAC2011 (2011),
https://accelconf.web.cern.ch/AccelConf/IPAC2011/papers/wepc024.pdf.

[70] M. Aiba, M. Böge, J. Chrin, N. Milas, T. Schilcher, et al., "Comparison of linear optics measurement and correction methods at the Swiss Light Source", Phys. Rev. ST Accel. Beams **16** (2013) DOI: 10.1103/PhysRevSTAB.16.012802,
http://link.aps.org/doi/10.1103/PhysRevSTAB.16.012802.

[71] V. Smaluk, X. Yang, W. Guo, Y. Hidaka, G. Wang, et al., "Experimental Crosscheck of Algorithms for Magnet Lattice Corrections", in Proceedings of IPAC2016 (2016),
https://inspirehep.net/record/1470505.

[72] G. Vanbavinckhove, M. Aiba, A. Nadji, L. Nadolski, R. Tomás, et al., "Linear and Non-Linear Optics Measurements at SOLEIL", in Proceedings of PAC09 (2009),
https://accelconf.web.cern.ch/AccelConf/PAC2009/papers/th6pfp075.pdf.

[73] M. Carlà, Z. Martí, G. Benedetti, and L. Nadolsky, "Optimization of Turn by Turn Measurements at Soleil and Alba Light Sources", in Proceedings of IPAC2015 (2015),
https://accelconf.web.cern.ch/AccelConf/IPAC2015/papers/tupje035.pdf.

[74] K. Fuchsberger, "Novel Concepts for Optimization of the CERN Large Hadron Collider Injection Lines", PhD thesis (TU Wien, 2011),
https://cds.cern.ch/record/1377386.

[75] K. Fuchsberger, “LOCO for LHC”, in Optics Measurements, Corrections and Modeling for High-Performance Storage Rings Workshop (2011), https://indico.cern.ch/event/132526.

[76] M. Aiba, S. Fartoukh, A. Franchi, M. Giovannozzi, V. Kain, et al., “First β-beating measurement and optics analysis for the CERN Large Hadron Collider”, Phys. Rev. ST Accel. Beams **12** (2009) DOI: 10.1103/PhysRevSTAB.12.081002, http://link.aps.org/doi/10.1103/PhysRevSTAB.12.081002.

[77] *MAD-X*, https://cern.ch/mad.

[78] R. Tomás, O. Brüning, M. Giovannozzi, P. Hagen, M. Lamont, et al., “CERN Large Hadron Collider optics model, measurements, and corrections”, Phys. Rev. ST Accel. Beams **13** (2010) DOI: 10.1103/PhysRevSTAB.13.121004, http://link.aps.org/doi/10.1103/PhysRevSTAB.13.121004.

[79] M. Bai, J. Aronson, M. Blaskiewicz, Y. Luo, S. White, et al., “Optics Measurements and Corrections at RHIC”, in Proceedings of IPAC2012 (2012), https://www.bnl.gov/isd/documents/78622.pdf.

[80] P. Skowroński, “Measurements at 40cm and Computer Aided Segment By Segment corrections”, in Optics Measurement and Correction Review (2013), http://indico.cern.ch/event/246159/overview.

[81] J. Coello de Portugal, F. Carlier, A. Langner, T. Persson, P. Skowroński, et al., “OMC Software Improvements in 2014”, in Proceedings of IPAC2015 (2015), https://inspirehep.net/record/1417296.

[82] M. Kuhn, A. Langner, G. Arduini, V. Kain, M. Schaumann, et al., “Origins of Transverse Emittance Blow-Up During the LHC Energy Ramp”, in Proceedings of IPAC14 (2014), https://inspirehep.net/record/1314178.

[83] G. Valentino, A. Langner, S. Redaelli, and R. Tomás, “Comparison of Beam Sizes at the Collimator Locations from Measured Optics and Beam-based Collimator Alignment in the LHC”, in Proceedings of IPAC2015 (2015), https://cds.cern.ch/record/2141841.

[84] A. Langner, J. Coello de Portugal, P. Skowroński, and R. Tomás, “Developments of the Segment-by-Segment Technique for Optics Corrections in the LHC”, in Proceedings of IPAC2015 (2015), https://inspirehep.net/record/1417295.

[85] R. Tomás, O. Brüning, R. Calaga, S. Fartoukh, A. Franchi, et al., "Procedures and Accuracy Estimates for Beta-Beat Correction in the LHC", in Proceedings of EPAC06 (2006),
https://inspirehep.net/record/727774.

[86] V. Blobel and E. Lohrmann, *Statistische und numerische Methoden der Datenanalyse* (1998),
https://link.springer.com/book/10.1007%2F978-3-663-05690-4.

[87] O. Behnke, K. Kröninger, G. Schott, and T. Schörner-Sadenius, *Data Analysis in High Energy Physics: A Practical Guide to Statistical Methods* (Wiley-VCH Verlag GmbH, 2013),
https://cds.cern.ch/record/1517556.

[88] A. Franchi, "Error analysis of linear optics measurements via turn-by-turn beam position data in circular accelerators", arXiv Prepr. (2016),
https://arxiv.org/abs/1603.00281.

[89] P. Hagen, M. Giovannozzi, J.-P. Kouttchouk, T. Risselada, S. Sanfilippo, et al., "WISE: An adaptive simulation of the LHC optics", in Proceedings of EPAC06 (2006),
https://accelconf.web.cern.ch/accelconf/e06/PAPERS/WEPCH139.PDF.

[90] P. Hagen, M. Giovannozzi, J.-P. Kouttchouk, T. Risselada, F. Schmidt, et al., "WISE: A simulation of the LHC optics including magnet geometrical data", in Proceedings of EPAC08 (2008),
https://accelconf.web.cern.ch/AccelConf/e08/papers/tupp091.pdf.

[91] D. Einfeld on behalf of the CELLS - Commissioning Team, "ALBA Synchrotron Light Source Commissioning", in Proceedings of IPAC2011 (2011),
https://accelconf.web.cern.ch/AccelConf/IPAC2011/papers/moxaa01.pdf.

[92] F. Perez on behalf of the Accelerator Division, "1st Year Operation of the ALBA Synchrotron Light Source", in Proceedings of IPAC2013 (2013),
https://accelconf.web.cern.ch/AccelConf/IPAC2013/papers/mopea055.pdf.

[93] M. Kuhn, "LHC K-Modulation - First Results", in OMC Meeting (2015),
https://indico.cern.ch/event/406408/.

[94] A. Langner, "Update on comparison AC dipole vs. k-modulation", in OMC Meeting (2015),
https://indico.cern.ch/event/406408/.

[95] M. Kuhn, *Private communication*, 2015.

[96] X. Huang, J. Sebek, and D. Martin, "Lattice modeling and calibration with turn-by-turn orbit data", Phys. Rev. ST Accel. Beams **13** (2010) DOI: 10.1103/PhysRevSTAB.13.114002,
http://link.aps.org/doi/10.1103/PhysRevSTAB.13.114002.

[97] X. Yang and X. Huang, "Simultaneous linear optics and coupling correction for storage rings with turn-by-turn beam position monitor data", arXiv Prepr. (2015),
https://arxiv.org/abs/1511.02450.

[98] Z. Martí, G. Benedetti, M. Carlà, and A. Olmos, "First Turn-by-Turn Measurements for Beam Dynamics Studies at ALBA", in Proceedings of IPAC14 (2014),
https://accelconf.web.cern.ch/AccelConf/IPAC2014/papers/tupro060.pdf.

[99] Z. Marti, *LOCO accuracy simulations with ALBA lattice*, tech. rep. (ALBA Project Document No ACDIV-2013-17, 2013),
https://intranet.cells.es/Divisions/Accelerators/publications/ACDIV-2013-17.pdf.

[100] R. Calaga and R. Tomás, "Statistical analysis of RHIC beam position monitors performance", Phys. Rev. ST Accel. Beams **7** (2004) DOI: 10.1103/PhysRevSTAB.7.042801,
http://link.aps.org/doi/10.1103/PhysRevSTAB.7.042801.

[101] R. E. Meller, A. W. Chao, J. M. Peterson, S. G. Peggs, and M. Furman, "Decoherence of Kicked Beams", SSC-N-360 (1987),
http://mafurman.lbl.gov/SSC-N-360.pdf.

[102] W. Guo, S. Kramer, F. Willeke, X. Yang, and L. Yu, "A Lattice Correction Approach Through Betatron Phase", in Proceedings of IPAC2016 (2016),
https://inspirehep.net/record/1469517/.

[103] A. A. Nosych, U. Iriso, A. Olmos, and M. Wendt, "Overview of the Geometrical Non-Linear Effects of Button BPMs and Methodology for their Efficient Suppression", in Proceedings of IBIC2014 (2014),
https://accelconf.web.cern.ch/AccelConf/IBIC2014/papers/tupf03.pdf.

[104] T. Bach, P. Hagen, A. Langner, Y. Levinsen, M. McAteer, et al., "1 % Calibration Errors in MQY Magnets", CERN-ATS-Note-2013-029 MD (LHC) (2013),
http://cds.cern.ch/record/1545888.

[105] N. Magnin, "AC-Dipole Upgrades", in LHC Optics Measurement and Correction review (2013),
http://indico.cern.ch/event/246159/.

[106] A. Langner, F. Carlier, J. Coello de Portugal, A. Valdivieso, E. H. Maclean, et al., “LHC Optics Commissioning at $\beta^* = 40$ cm and 60 cm”, CERN-ACC-NOTE-2015-0035 (2015),
https://cds.cern.ch/record/2063433/.

[107] T. H. B. Persson, A. Gorzawski, A. Langner, L. Malina, E. H. Maclean, et al., “Coupling Measurements and Corrections for the Combined Ramp and Squeeze”, CERN-ACC-NOTE-2016-0030 (2016),
https://cds.cern.ch/record/2135869.

[108] T. Persson and R. Tomás, “Optimizing Chromatic Coupling Measurement in the LHC”, in Proceedings of IPAC2016 (2016),
https://inspirehep.net/record/1469945.

[109] S. Mönig, E. H. Maclean, T. H. B. Persson, J. Coello de Portugal, A. Langner, et al., “Short Term Dynamic Aperture with AC Dipoles”, in Proceedings of IPAC2016 (2016),
https://inspirehep.net/record/1470532.

[110] F. Carlier, J. Coello de Portugal, E. H. Maclean, T. Persson, and R. Tomás, “Observation of Resonance Driving Terms in the LHC During Runs I and II”, in Proceedings of IPAC2016 (2016),
https://cds.cern.ch/record/2207444.

[111] A. Valdivieso, F. Carlier, C. A. Bonilla, A. Langner, E. H. Maclean, et al., “LHC injection optics measurements at commissioning (2015)”, CERN-ATS-Note-2016-0033 (2016),
http://cds.cern.ch/record/2143878.

[112] J. Wenninger and A. A. Gorzawski, “Implementation of Luminosity Leveling by Betatron Function Adjustment at the LHC Interaction Points”, in Proceedings of IPAC14 (2014),
https://inspirehep.net/record/1314189.

[113] X. Buffat, W. Herr, M. Lamont, T. Pieloni, S. Redaelli, et al., “Colliding During the Squeeze and β^* Levelling in the LHC”, in Proceedings of IPAC2013 (2013),
https://inspirehep.net/record/1337096.

[114] “188th LHC Machine Committee (LMC) Meeting”, (2014),
https://espace.cern.ch/lhc-machine-committee/Minutes/1/lmc_188.pdf.

[115] “218th LHC Machine Committee (LMC) Meeting”, (2015),
https://espace.cern.ch/lhc-machine-committee/Minutes/1/lmc_218.pdf.

[116] H. Mainaud Durand, “Update on IR8 triplet”, in LHC Machine Committee (LMC) (2015),
https://indico.cern.ch/event/451810/.

[117] J. Wenninger, “Update on IT movement in IR8”, in LBOC Meet. No 57 (2016), https://indico.cern.ch/event/506059/.

[118] T. Persson, for the OMC team, “Beta* corrections strategies”, in LBOC Meet. No 52 (2015),
https://indico.cern.ch/event/461647/.

[119] R. Tomás, F. Antoniou, F. Carlier, J. Coello de Portugal, A. Valdivieso, et al., “On possible sources of luminosity imbalance”, in LBOC Meet. No 50 (2015), https://indico.cern.ch/event/451059/.

[120] M. Kuhn, “Updated results from triplet k-modulation”, in LBOC Meet. No 52 (2015),
https://indico.cern.ch/event/461647/.

[121] S. Sanfilippo, P. Hagen, J.-P. Koutchouk, M. Giovannozzi, and T. Risselada, “Transfer Function of the Quadrupoles and Beta-Beating”, LHC Project Workshop - ’Chamonix XV’ (2006),
https://cds.cern.ch/record/974531.

[122] A. Langner, F. Carlier, A. Valdivieso, E. H. Maclean, L. Malina, et al., “Optics Model”, in Proceedings of the 2015 Evian Workshop on LHC Beam Operation (2015),
https://cds.cern.ch/record/2156966.

[123] T. Persson, for the OMC team, “2016 Optics Measurements and Corrections”, in LBOC Meet. No 58 (2016),
https://indico.cern.ch/event/512714/.

[124] A. Valdivieso, F. Carlier, J. Coello de Portugal, A. Langner, E. H. Maclean, et al., “Optics-Measurement-Based BPM Calibration”, in Proceedings of IPAC16 (2016),
https://accelconf.web.cern.ch/AccelConf/ipac2016/papers/thpmb041.pdf.

[125] R. Bruce and S. Redaelli, “2016 LHC Configuration: Can we get to $\beta^* = 40$ cm?”, in Proceedings of the 2015 Evian Workshop on LHC Beam Operation (2015),
https://cds.cern.ch/record/2156966.

[126] R. Tomás, M. Aiba, A. Franchi, and U. Iriso, “Review of Linear Optics Measurements and Corrections in Accelerators”, to be submitted to Phys. Rev. Acc. Beams (2016).

[127] M. Kuhn, G. Arduini, P. Baudrenghien, J. Emery, A. Guerrero, et al., “Investigations of the LHC Emittance Blow-Up during the 2012 Proton Run”, in Proceedings of IPAC2013 (2013),
https://cds.cern.ch/record/1567254.

[128] A. Langner and R. Tomás, "Optics measurement algorithms and error analysis for the proton energy frontier", Phys. Rev. ST Accel. Beams **18** (2015) DOI: 10.1103/PhysRevSTAB.18.031002, http://link.aps.org/doi/10.1103/PhysRevSTAB.18.031002.

[129] M. Kuhn, G. Arduini, V. Kain, A. Langner, Y. Papaphilippou, et al., "Emittance Growth During the LHC Ramp", in LS1 LBOC Meet. No 11 (2014), https://indico.cern.ch/event/295915/.

[130] N. Ryckx, "Combined energy ramp and β^* squeeze at the Large Hadron Collider", PhD thesis (2012), https://cds.cern.ch/record/1421259.

[131] S. Redaelli, M. Lamont, G. Mueller, N. Ryckx, R. Tomás, et al., "Combined Ramp and Squeeze at the Large Hadron Collider", in Proceedings of IPAC2012 (2012), https://inspirehep.net/record/1125451/.

[132] A. Langner, J. Coello de Portugal, A. A. Gorzawski, S. Redaelli, M. Schaumann, et al., "First beam test of a combined ramp and squeeze at LHC", CERN-ACC-NOTE-2015-0023 (2015), https://cds.cern.ch/record/2049886.

[133] J. Coello de Portugal, *Private communication*, 2016.

[134] N. Magnin, *Private communication*, 2016.

[135] L. Malina, "Optics errors at 2.51 TeV", in OMC Meeting (2015), https://indico.cern.ch/event/459612.

[136] O. Brüning, "The High Luminosity LHC Project", in Proceedings of IPAC2015 (2015), https://jacowfs.jlab.org/conf/proceedings/IPAC2015/papers/frxc2.pdf.

[137] A. Apollonio, M. Jonker, R. Schmidt, B. Todd, D. Wollmann, et al., "Update on Predictions for Yearly Integrated Luminosity for HL-LHC Based on Expected Machine Availability", in Proceedings of IPAC14 (2014), https://cds.cern.ch/record/2003167.

[138] D. R. Brett, R. B. Appleby, R. De Maria, J. Garcia, R. Tomás, et al., "Accurate crab cavity modeling for the high luminosity Large Hadron Collider", Phys. Rev. ST Accel. Beams **17** (2014) DOI: 10.1103/PhysRevSTAB.17.104001, https://link.aps.org/doi/10.1103/PhysRevSTAB.17.104001.

[139] S. U. De Silva, H. Park, J. R. Delayen, Z. Li, and T. H. Nicol, "Design and Prototyping of a 400 MHz RF-Dipole Crabbing Cavity for the LHC High-Luminosity Upgrade", in Proceedings of IPAC2015 (2015), https://cds.cern.ch/record/2114083.

[140] R. Schmidt, T. Bär, J. Wenninger, D. Wollmann, and M. Zerlauth, "Machine Protection challenges for HL-LHC", in Proceedings of IPAC14 (2014), https://cds.cern.ch/record/1968625.

[141] H. Garcia Morales, R. Bruce, and S. Redaelli, "Beam Cleaning in Experimental IRs in HL-LHC for the Incoming Beam", in Proceedings of IPAC2015 (2015), https://cds.cern.ch/record/2114111.

[142] R. Bruce, F. Cerutti, L. S. Esposito, J. M. Jowett, A. Lechner, et al., "Collimator Layouts for HL-LHC in the Experimental Insertions", in Proceedings of IPAC2015 (2015), https://jacowfs.jlab.org/conf/proceedings/IPAC2015/papers/tupty028.pdf.

[143] S. Fartoukh, "Achromatic telescopic squeezing scheme and application to the LHC and its luminosity upgrade", Phys. Rev. ST Accel. Beams **16** (2013) DOI: 10.1103/PhysRevSTAB.16.111002, http://link.aps.org/doi/10.1103/PhysRevSTAB.16.111002.

[144] S. Fartoukh, G. Vanbavinckhove, M. C. Alabau Pons, R. Alemany Fernandez, R. Assmann, et al., "The Achromatic Telescopic Squeezing (ATS) MD part I", CERN-ATS-Note-2011-033 MD (2011), https://cds.cern.ch/record/1353518.

[145] S. Fartoukh, M. Lamont, R. de Maria, R. Miyamoto, G. Mueller, et al., "The Achromatic Telescopic Squeezing (ATS) MD part II", CERN-ATS-Note-2011-060 MD (2011), https://cds.cern.ch/record/1369240.

[146] S. Fartoukh, R. Tomás, B. Goddard, W. Hofle, D. Jacquet, et al., "The Achromatic Telescopic Squeezing (ATS) MD part III", CERN-ATS-Note-2011-132 MD (2011), https://cds.cern.ch/record/1407532.

[147] S. Fartoukh, V. Kain, Y. Levinsen, E. Maclean, R. de Maria, et al., "The 10 cm beta* ATS MD", CERN-ATS-Note-2013-004 MD (2013), http://cds.cern.ch/record/1507216.

[148] B. J. Holzer, R. De Maria, S. Fartoukh, A. Chancé, B. Dalena, et al., "Optics Design and Lattice Optimisation for the HL-LHC", in Proceedings of IPAC2013 (2013), https://cds.cern.ch/record/1581707.

[149] J. Coello de Portugal, "Analysis of tune and beta-beating jitter from IT power converters", in 63rd HiLumi WP2 Meet. (2016), https://indico.cern.ch/event/463028/.

[150] R. de Maria, S. Fartoukh, and M. Fitterer, “HLLHCV1.1: Optics Version for the HL-LHC Upgrade”, in Proceedings of IPAC2015 (2015), https://cds.cern.ch/record/2112237.

[151] Y. Nosochkov, Y. Cai, M.-H. Wang, S. Fartoukh, M. Giovannozzi, et al., “Specification of Field Quality in the Interaction Region Magnets of the High Luminosity LHC Based on Dynamic Aperture”, in Proceedings of IPAC14 (2014), https://cds.cern.ch/record/1746712.

[152] J. Coello de Portugal, F. Carlier, A. Valdivieso, A. Langner, E. H. Maclean, et al., “Local Optics Corrections in the HL-LHC IR”, in Proceedings of IPAC2016 (2016), https://cds.cern.ch/record/2207447.

[153] A. Valdivieso, “MD result: alignment optics”, in 60th HiLumi WP2 Task Leader Meeting (2015), https://indico.cern.ch/event/402183/.

[154] L. Malina, J. Coello de Portugal, A. Langner, T. Persson, P. K. Skowro, et al., “Comparison of Optics Measurement Methods in ESRF”, in Proceedings of IPAC2016 (2016), https://cds.cern.ch/record/2207439.

[155] H. Fischer, *A history of the central limit theorem: from classical to modern probability theory* (2010), DOI: 10.1007/978-0-387-87857-7, https://cds.cern.ch/record/1412718.

Appendices

A. Hypothesis testing

Statistical auxiliary means, which have been used in this thesis for the test of hypotheses, are briefly introduced in the following sections.

A.1. χ^2-test

Assuming independent random variables x_i, which follow a Gaussian distribution with the probability density

$$f(x_i, \mu, \sigma) = \frac{1}{\sqrt{2\sigma^2\pi}} \exp\left[-\frac{(x_i - \mu)^2}{2\sigma^2}\right]. \tag{A.1}$$

For $\mu = 0$ and $\sigma = 1$, the sum of the squares

$$\chi^2 = \sum_{i=1}^{n} x_i^2, \tag{A.2}$$

follows a χ^2 distribution with n degrees of freedom (ν), whose probability density function is given by [86]

$$p(\chi^2, \nu) = \frac{(\chi^2)^{(\nu-2)/2} e^{-\chi^2/2}}{2^{\nu/2}\Gamma(\nu/2)}. \tag{A.3}$$

The χ^2 test can be used to evaluate the agreement of a measurement result with a theoretical model, if one has measurement variables y_i, which are independent and follow a normal distribution with μ_i and σ_i. This assumption is approximately valid in many cases due to the central limit theorem [155]. If the measurement results y_i are compatible with the theoretical expectation $y_{t,i}$, which is the hypothesis H_0, then the assumptions of Eq. (A.2) are fulfilled if the χ^2 is calculated as

$$\chi^2 = \sum_{i=1}^{n} \frac{y_i - y_{t,i}}{\sigma_i}. \tag{A.4}$$

The expected value of the χ^2 distribution is equal to the degrees of freedom, $E[\chi^2] = \nu$. Therefore, χ^2/ν, also referred to as the reduced χ^2, is expected to be close to one. A

value which differs, could mean that the measurement uncertainty is overestimated, if $\chi^2/\nu < 1$, or underestimated, if $\chi^2/\nu > 1$. However, it could also mean that H_0 is wrong.
More precisely one can evaluate the level of agreement by computing

$$P(\chi^2, \nu) = \int_{\chi^2}^{\infty} p(z, \nu)\,\mathrm{d}z, \tag{A.5}$$

which gives the probability to achieve a certain χ^2 or a larger one. This means $P(\chi^2, \nu)$ is the probability, assuming H_0 is correct, to achieve the observed level of agreement or a poorer one. If the probability is too low, this is an indication that there might be problem with the theoretical model, or with the assumed uncertainties.

A.2. p-value

The p-value is the probability to achieve the observed result or a more extreme one, assuming the hypothesis H_0 is true. A more extreme result could mean for example,

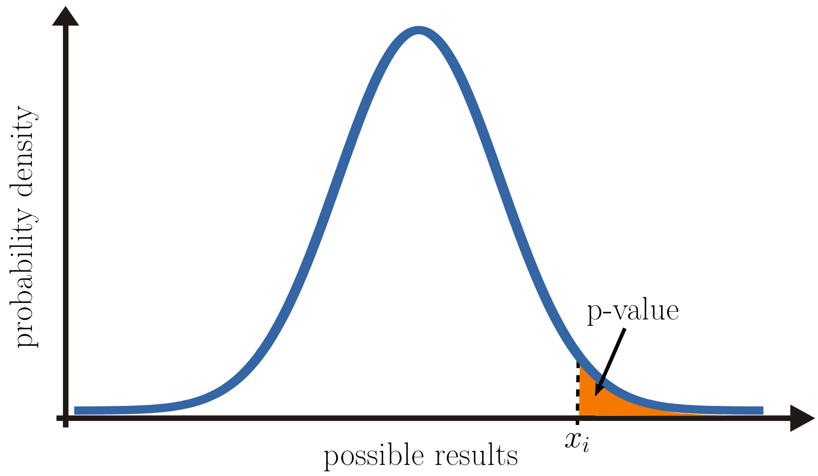

Figure A.1.: Illustration of the p-value for the observed result x_i, where a more extreme results would be larger than x_i.

a result which is larger than the observed one, as shown in Fig. A.1, which gives a one-sided p-value. A two-sided p-value covers both tails of the probability density function and is computed as two times the minimum of the two one-sided p-value for the left and right side.
For the χ^2-test in the previous section, the p-value would be equal to $P(\chi^2, \nu)$, if H_0 is true. By their definition, the p-values, if H_0 is true, follow a uniform distribution.

B. Measured β-beating

B.1. Injection energy

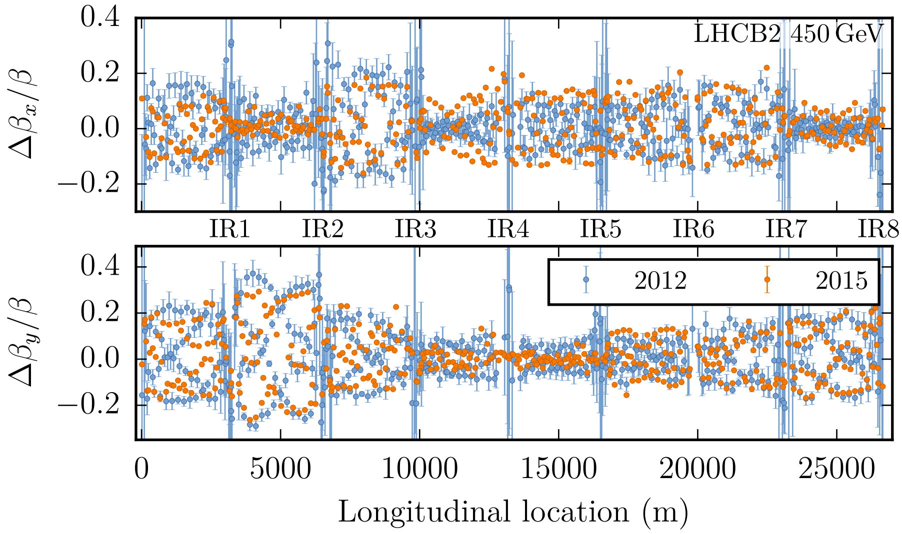

Figure B.1.: β-beating at injection for beam 2 in 2015 in comparison to 2012.

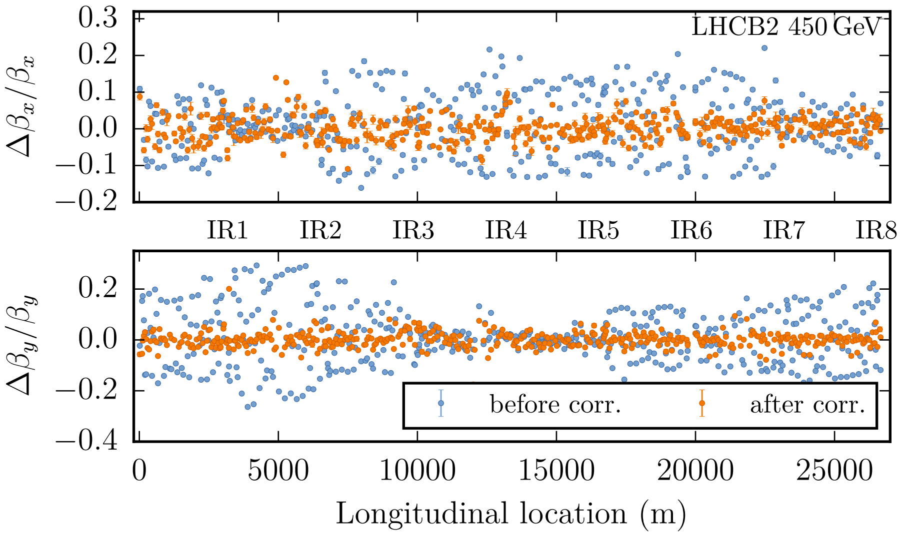

Figure B.2.: β-beating at injection for beam 2 before and after optics correction.

B.2. Squeezed optics

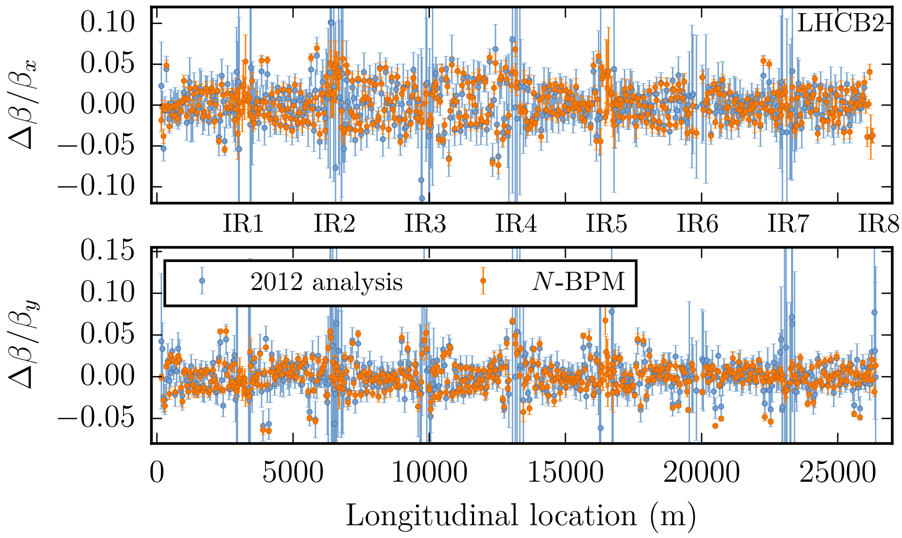

Figure B.3.: β-beating for Beam 2 after local and global corrections at $\beta^* = 60\,\mathrm{cm}$.

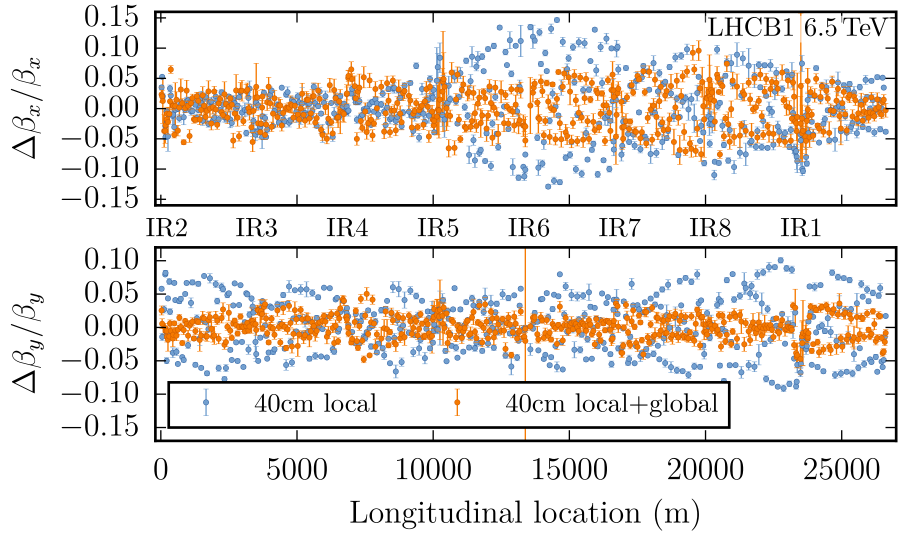

Figure B.4.: β-beating after local and global optics corrections along the machine for beam 1 at a β^* of 40 cm.

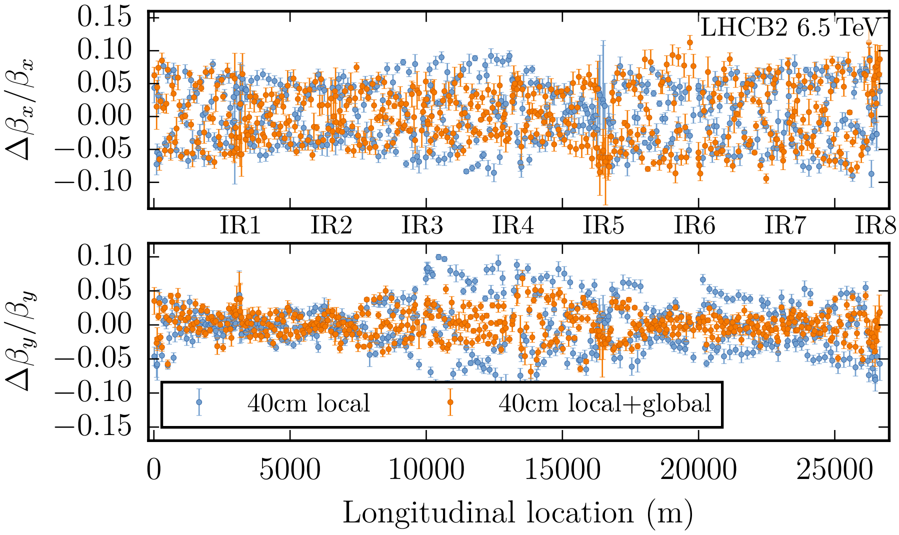

Figure B.5.: β-beating after local and global optics corrections along the machine for beam 2 at a β^* of 40 cm.

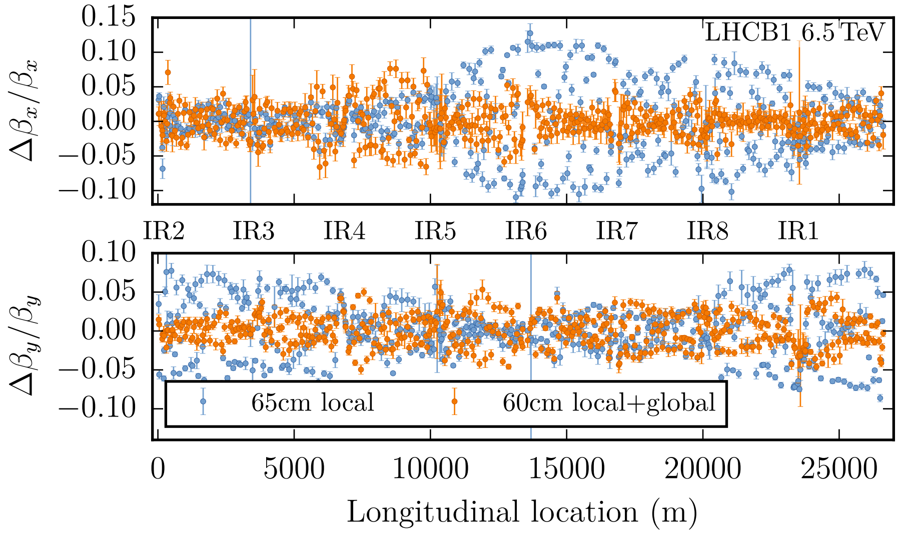

Figure B.6.: β-beating after local and global optics corrections along the machine for beam 1 at a β^* of 60 cm.

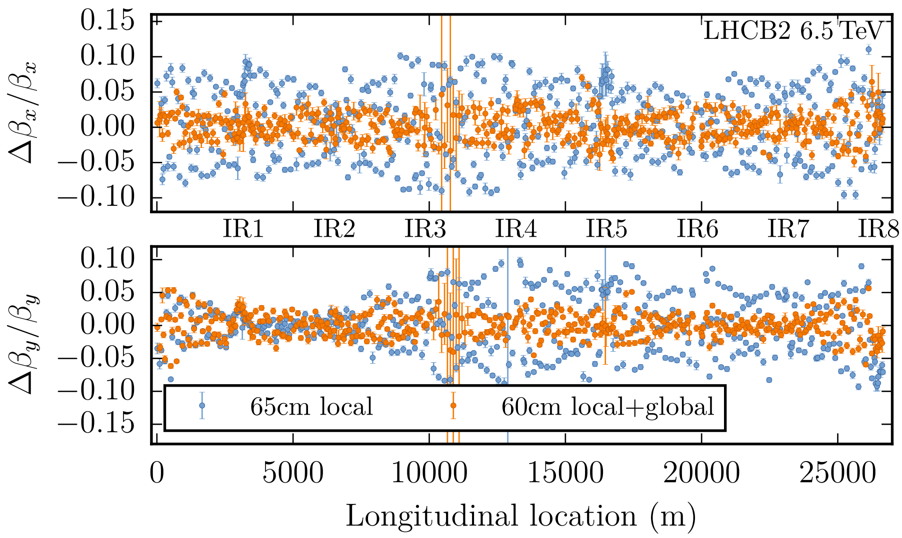

Figure B.7.: β-beating after local and global optics corrections along the machine for beam 2 at a β^* of 60 cm.

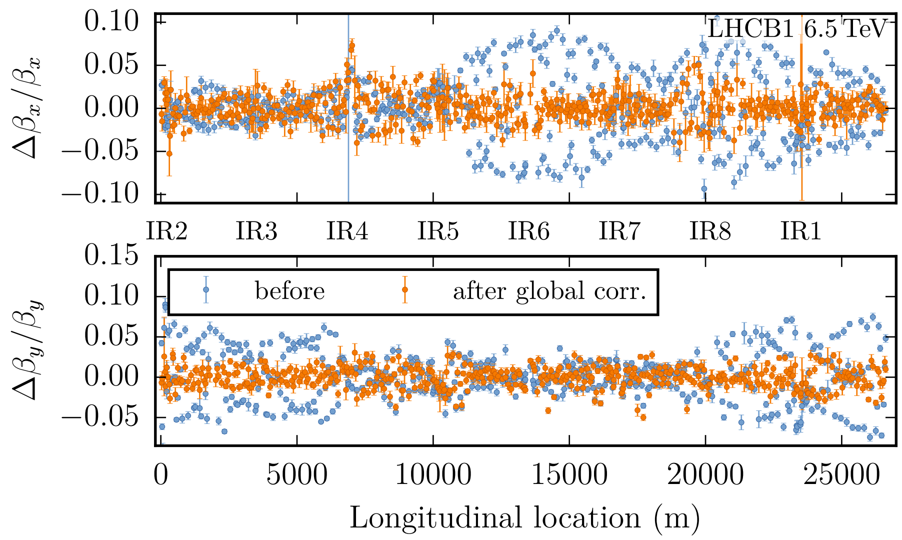

Figure B.8.: β-beating after local and global optics corrections along the machine for beam 1 at a β^* of 80 cm.

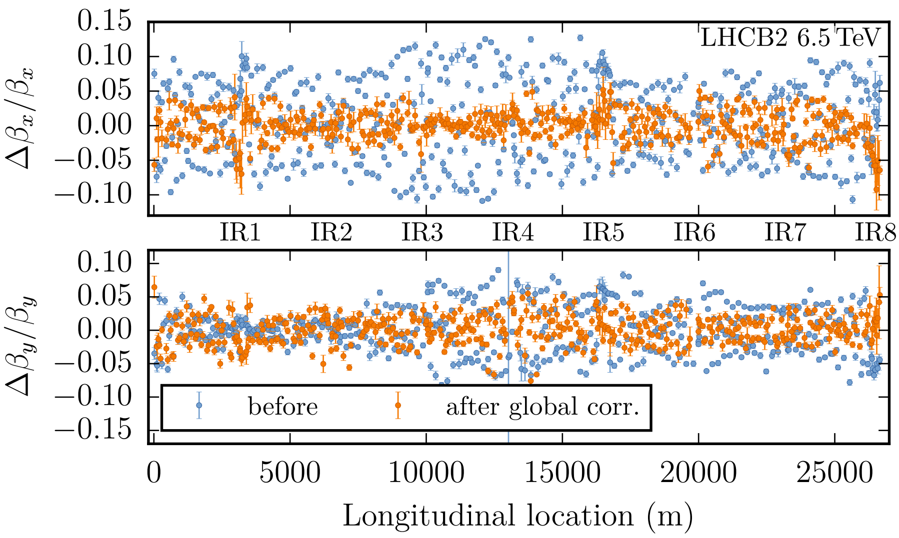

Figure B.9.: β-beating after local and global optics corrections along the machine for beam 2 at a β^* of 80 cm.

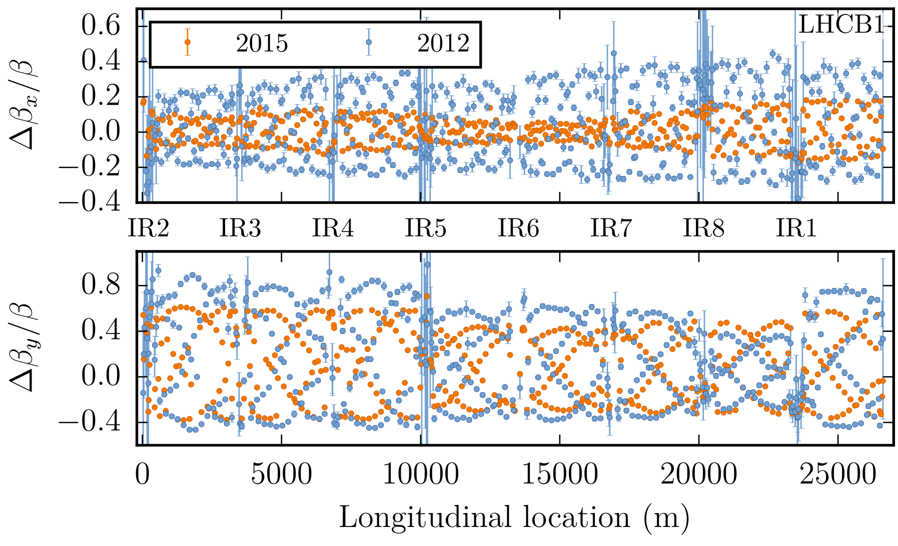

Figure B.10.: β-beating before optics corrections for beam 1 at a β^* of 60 cm (2012) and 65 cm (2015).

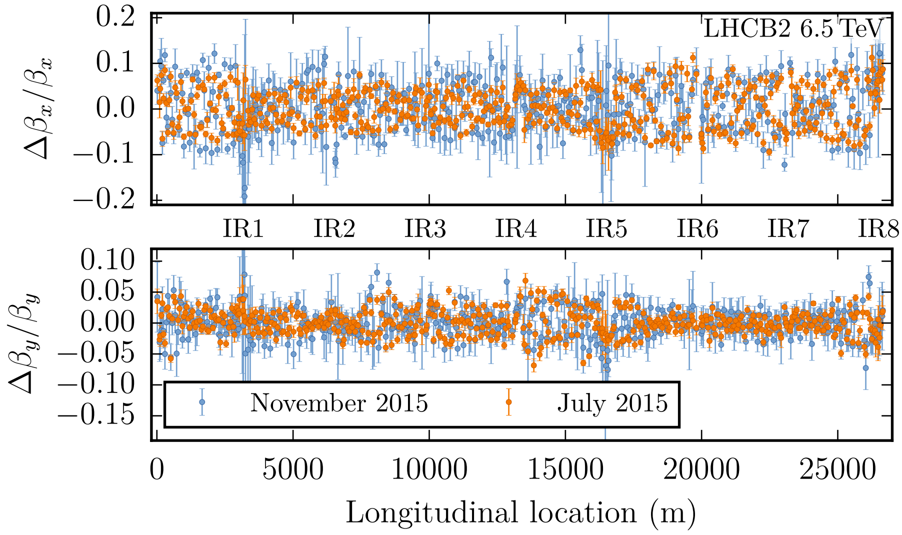

Figure B.11.: Repeated measurement of the β-beating for beam 2 at a β^* of 40 cm after a time period of 4 months.

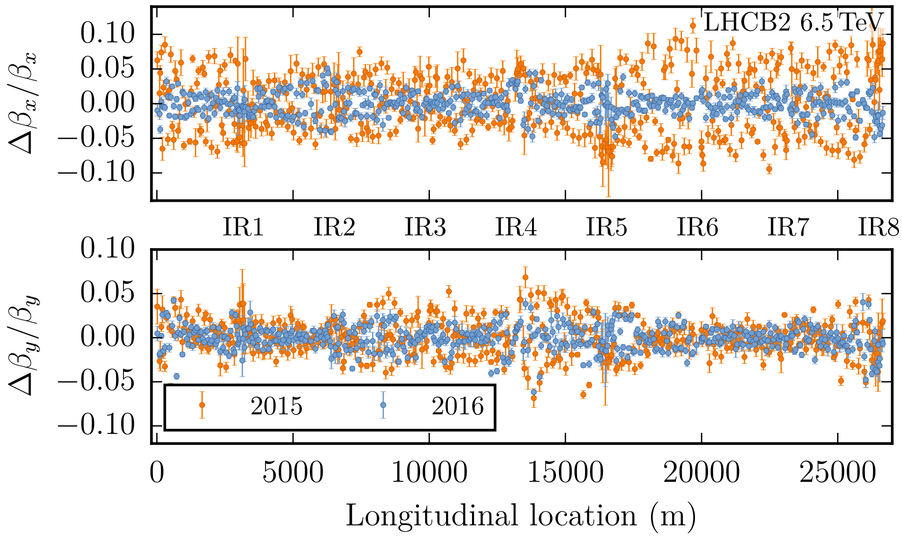

Figure B.12.: β-beating for beam 2 at $\beta^* = 40$ cm after corrections in 2015 and 2016.

B.3. Energy ramp

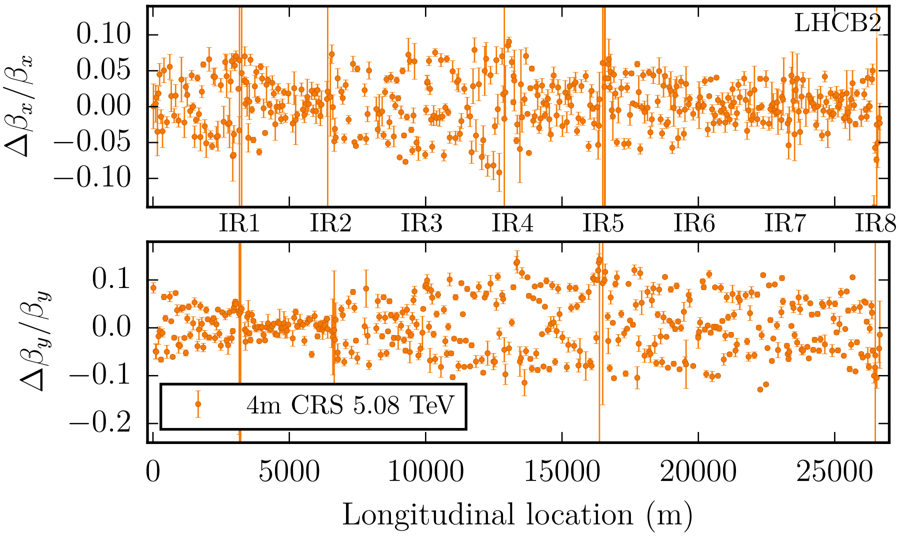

Figure B.13.: Beta-beating for beam 2 during the CRS at an energy of 5.08 TeV and a β^* of 4 m in IP1 and IP5.

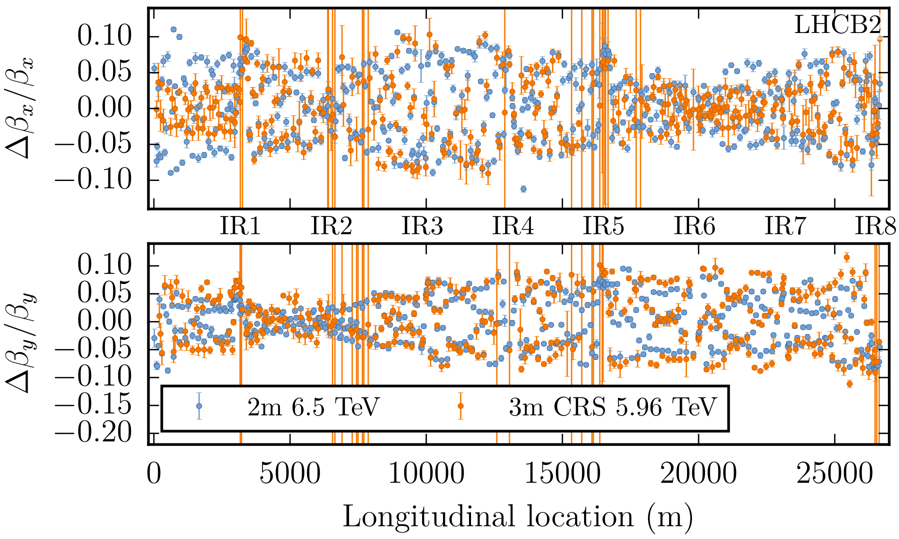

Figure B.14.: Beta-beating for beam 2 during the CRS at an energy of 5.96 TeV and a β^* of 3 m in IP1 and IP5 in comparison to a static measurement at 6.5 TeV with a β^* of 2 m.

B.4. ATS optics

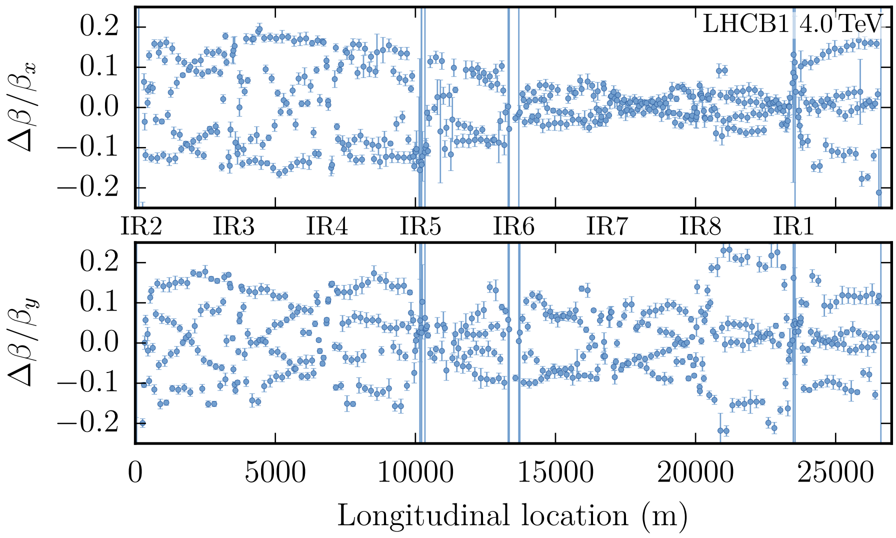

Figure B.15.: Beta-beating for beam 1 for ATS optics with $\beta^* = 40\,\mathrm{cm}$.

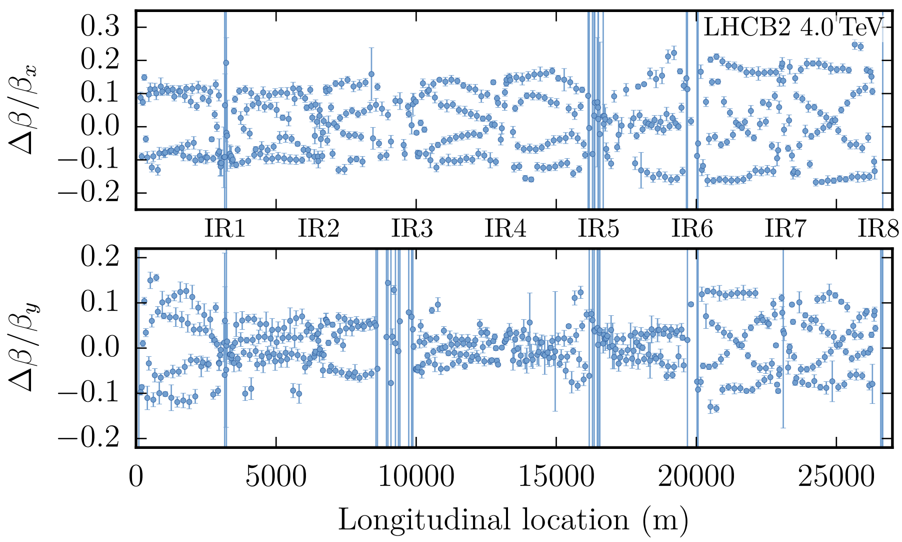

Figure B.16.: Beta-beating for beam 2 for ATS optics with $\beta^* = 40\,\mathrm{cm}$.

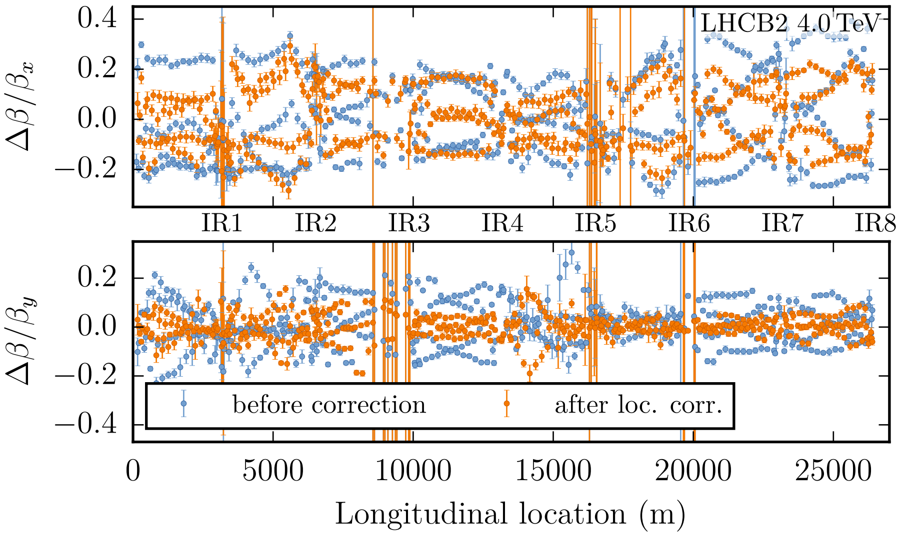

Figure B.17.: Beta-beating for beam 2 for ATS optics with $\beta^* = 20\,\text{cm}$, before and after local corrections.

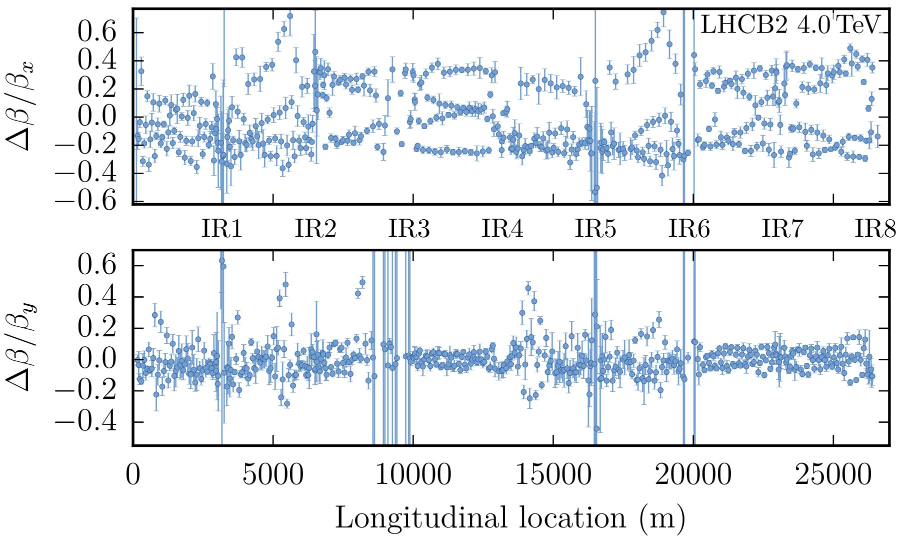

Figure B.18.: Beta-beating for beam 2 for ATS optics with $\beta^* = 10\,\text{cm}$.

C. Local optics corrections for run II

Table C.1.: Local correction strengths from run II compared to run I for interaction region (IR) quadrupoles. The circuits of the final focusing quadrupoles are highlighted with a bold font.

Location	**Circuit**	**Δk (10^{-5}m^{-2})**		**Relative (%)**
		2012	**2015**	**2015**
IR1	**ktqx1.r1**	**1.0**		
	ktqx2.l1	**1.0**	**0.35**	**−0.04**
	ktqx2.r1	**−1.4**	**−0.7**	**+0.08**
	kq4.l1b2	−0.5		
	kq9.l1b1	1.5		
IR2	**ktqx2.l2**		**−2.0**	**−0.21**
	ktqx2.r2		**2.0**	**−0.21**
IR5	**ktqx1.l5**		**2.0**	**−0.23**
	ktqx1.r5		**−2.0**	**−0.23**
	ktqx2.r5	**1.05**	**1.9**	**0.22**
	ktqx2.l5	**0.70**	**−0.09**	**0.01**
	kq4.l5b2	3.80		
IR6	kq5.l6b1	−3.9		
	kq5.r6b1	0.9		
	kq5.l6b2	4.8		
	kq5.r6b2	1.0		
IR8	**ktqx2.l8**		**−1.0**	**−0.11**
	kq4.l8b1	4.0		
	kq4.r8b2	−10.0		
	kq5.r8b1	8.0		
	kq5.r8b2	−3.0		
	kq6.l8b1	2.0	−2.0	0.46
	kq6.l8b2	−3.0	2.0	0.35